NEUTRON FLUX CHARACTERIZATION AND DESIGN OF UFTR RADIATION BEAM PORT USING MONTE CARLO METHODS

By

ROMEL SIQUEIRA FRANÇA

A THESIS PRESENTED TO THE GRADUATE SCHOOL
OF THE UNIVERSITY OF FLORIDA IN PARTIAL FULFILLMENT
OF THE REQUIREMENTS FOR THE DEGREE OF
MASTER OF SCIENCE

UNIVERSITY OF FLORIDA

2012

© 2012 Romel Siqueira França

I dedicate my thesis to my mother.

ACKNOWLEDGMENTS

I have deeply appreciation and respect for Dr. Schubring for his willingness to help and to guide me on my research. Dr. Schubring is a wealth of knowledge and dedication always trying to get the best out of their students. To meet such a human being like Dr. Schubring it was a unique opportunity that I had in my life.

TABLE OF CONTENTS

page

ACKNOWLEDGMENTS 4

LIST OF TABLES 7

LIST OF FIGURES 9

ABSTRACT 14

CHAPTER

1 INTRODUCTION 15

1.1 UFTR Reactor Background 15
1.2 UFTR Reactor Horizontal Beam Ports 16
1.3 UFTR Beam Port Challenges 17
1.4 Research Goals and Objective 18

2 REACTOR MODEL DEVELOPMENT 27

2.1 UFTR Reactor Model 27
2.2 UFTR Reactor Core Design 27
2.2.1 UFTR Fuel Box 28
2.2.2 UFTR Fuel Plate 28
2.3 Reactor Radiation Beam Ports Modeling 29

3 MCNP5 BACKGROUND AND CALCULATIONS 34

3.1 General Features of MCNP5 34
3.2 UF Cluster PC Computers 34
3.3 MCNP5 Deck 34
3.3.1 Criticality Determination 35
3.3.2 Fixed Source Methods Applied 35
3.3.2.1 Fixed source method with surface source read (SSR) . . 36
3.3.2.2 Fixed source method with SDEF 37

4 MCNP5 MATHEMATICAL AND THEORETICAL DISCUSSION 53

4.1 General Features of MCNP5 53
4.2 F4 Tally 53
4.3 FM Card - Tally Multiplier 54
4.4 FMESH4 Tally 55
4.5 Relative Error 56
4.6 Variance Reduction Methods 58
4.6.1 Nonanalog Methods 58
4.6.1.1 Geometry splitting (G.S.) 58
4.6.1.2 Russian roulette (R.R.) 58

4.6.1.3 Survival biasing (S.B.) . . . 59
4.6.2 Efficiency of the Nonanalog Method . . . 59
4.6.2.1 PHYS card . . . 60
4.6.2.2 IMP card . . . 60

5 MCNP5 SIMULATION RESULTS . . . 61

5.1 Introduction . . . 61
5.2 UFTR Beam Port . . . 62
5.2.1 UFTR Reactor South Beam Port Analyzes . . . 62
5.2.2 Energy Groups Analyzed . . . 62
5.2.3 South Beam Port 3-D Multi-Group Neutron Flux Distribution . . . 63
5.2.4 Impact of Different Moderators in the UFTR . . . 63

6 NEUTRON IRRADIATION CHARACTERIZATION OF GOLD FOIL . . . 113

6.1 Reaction-Rate Equation . . . 113
6.2 Activity Equations . . . 115
6.2.1 Irradiation Activity . . . 116
6.2.2 Activity After A_0 . . . 118
6.3 Reaction Rate Calculation using MCNP5 . . . 119

7 CONCLUSION . . . 124

APPENDIX

A URANIUM SILICIDE . . . 125

B ALUMINUM . . . 126

C THE EFFECT OF THE IMPURITY IN THE FUEL ON THE UFTR K_{eff} . . . 127

D FISSION CROSS-SECTIONS . . . 131

E 47 ENERGY GROUPS . . . 133

F BARYTES (BARITE) CONCRETE . . . 135

REFERENCES . . . 136

BIOGRAPHICAL SKETCH . . . 137

LIST OF TABLES

Table		page
1-1	Collimator Composition	19
1-2	PuBe and SbBe neutron sources features	19
1-3	Reactor power requirements for PuBe neutron source	19
2-1	Shielding nominal specifications	27
3-1	KCODE values - Criticality Source Card	35
3-2	Surface source write (SSW) and surface source read (SSR) cards	36
3-3	Possible MCNP5 constants for the Watt Fission Spectrum	40
5-1	MCNP5 - Total Transport Time (ctm) - 1CPU	61
5-2	MCNP5 - Relative Error% for tally type F4	62
5-3	Figure of Merit (FOM)	62
5-4	Energy range for UFTR measurements	62
5-5	General analyses for 47 energy groups for 16CPU's using (G.S. - R.R.)	63
5-6	General analyses for 47 energy groups for 16CPU's using (G.S. - R.R. - S.B.)	63
5-7	Cases of study for 47 energy groups	63
5-8	Physical properties of heavy water (D_2O) and light water (H_2O)	64
5-9	Slowing Down Parameters of Typical Moderators	64
6-1	Absorptive Reactions	113
6-2	Recommended γ-ray calibration energies and intensities	120
6-3	^{197}Au gold foil reaction rate	121
A-1	Uranium Silicide - (U_3Si_2)	125
A-2	Uranium Silicide Impurities	125
B-1	Aluminum - (Al)	126
B-2	Aluminum Impurities	126
C-1	$\sim$ no ^{10}B in the Aluminum Cladding	127
C-2	K_{eff} and Standard Deviation	127

C-3 ^{10}B in the Aluminum Cladding/ Variation of Cd concentration while Li is constant 128

C-4 K_{eff} and Standard Deviation 128

C-5 ^{10}B in the Aluminum Cladding/ Variation of Li concentration while Cd is constant 129

C-6 K_{eff} and Standard Deviation 129

E-1 47 Energy Groups 133

E-2 47 Energy Groups cont. 134

F-1 Elemental composition of barytes concretes in grams of element per cm^3 of concrete 135

F-2 Constants for thermal neutrons for barytes concretes 135

LIST OF FIGURES

Figure page

1-1 Axial projection of the UFTR, including all access ports. 20

1-2 Axial projection of the UFTR with its RABBIT system. 21

1-3 Horizontal beam ports drawing. 22

1-4 Collimator filtering a stream of rays in a general problem. Top without a collimator. Bottom with a collimator. 23

1-5 A Collimator 3D drawing. 24

1-6 Collimator 2D projection. 25

1-7 MCNP5 collimator x-y projection. 26

2-1 Radial projection of the UFTR core illustrating the fuel and the fuel box arrangement as surrounded by graphite stringers. 30

2-2 Horizontal section of the UFTR at beam tube level. 31

2-3 South beam port measurements. 32

2-4 MCNP model with materials, generated with MCNP Visual Editor (VisEd). . . . 33

3-1 Neutron fission density distribution $\sharp/\text{cm}^3$-sec for top view of the UFTR core. . 42

3-2 Neutron fission density distribution $\sharp/\text{cm}^3$-sec for bottom view of the UFTR core. 43

3-3 Neutron fission density distribution $\sharp/\text{cm}^3$-sec within six UFTR fuel boxes numbered from one to six showing the south view. 44

3-4 Neutron fission density distribution $\sharp/\text{cm}^3$-sec within six UFTR fuel boxes numbered from one to six showing the north view. 45

3-5 Flow chart calculation. 46

3-6 Average Fission Neutrons per group for Thermal Neutrons Fission in ^{235}U. . . . 47

3-7 Average Fission Neutrons per group for Thermal Neutrons Fission in ^{235}U (Log Scale). 48

3-8 Average Fission Neutrons per group for Thermal Neutrons Fission in ^{235}U. . . . 49

3-9 Average Fission Neutrons per group for Thermal Neutrons Fission in ^{235}U (Log Scale). 50

3-10 The Watt Fission Spectra when Thermal Neutrons Induce Fission in ^{235}U for $\chi(E)$ and f(a,b,E) (where a $= 0.988$ b $= 2.249$). 51

3-11 Schematic Neutron Fission Cross Section for U_{92}^{235} and U_{92}^{238} (Log Scale). . . . 52

5-1 Neutron fission density distribution $\sharp/cm^3$-sec throughout the fuel box 2 facing the reactor core. . . . 67

5-2 Neutron fission density distribution $\sharp/cm^3$-sec throughout the fuel box 2 facing south beam port. . . . 68

5-3 xy cross-section at z=-1 mid-section of the fuel box 2 . . . 69

5-4 2-D Neutron Flux Distribution for 47 energy groups along Y-axis (cm) before Collimator region. . . . 70

5-5 2-D Neutron Flux Distribution Relative Error for 47 energy groups along the Y-axis(cm) before Collimator region. . . . 71

5-6 2-D Neutron Flux Distribution for 47 energy groups along Y-axis (cm) before Collimator region. . . . 72

5-7 2-D Neutron Flux Distribution Relative Error for 47 energy groups along the Y-axis(cm) before Collimator region. . . . 73

5-8 2-D Neutron Flux Distribution for 47 energy groups along Y-axis (cm) in the Collimator region. . . . 74

5-9 2-D Neutron Flux Distribution Relative Error for 47 energy groups along the Y-axis(cm) in the Collimator region. . . . 75

5-10 2-D Neutron Flux Distribution for 47 energy groups along Y-axis (cm) in the Collimator region. . . . 76

5-11 2-D Neutron Flux Distribution Relative Error for 47 energy groups along the Y-axis(cm) in the Collimator region. . . . 77

5-12 2-D Neutron Flux Distribution Without Collimator for 47 energy groups along the Y-axis(cm) Before Collimator region. . . . 78

5-13 2-D Neutron Flux Distribution Relative Error for 47 energy groups Without Collimator along the Y-axis(cm) Before Collimator region. . . . 79

5-14 2-D Neutron Flux Distribution Without Collimator for 47 energy groups along the Y-axis(cm) Before Collimator region. . . . 80

5-15 2-D Neutron Flux Distribution Relative Error for 47 energy groups Without Collimator along the Y-axis(cm) Before Collimator region. . . . 81

5-16 2-D Neutron Flux Distribution Without Collimator for 47 energy groups along the Y-axis(cm) in the Collimator region. . . . 82

5-17 2-D Neutron Flux Distribution Relative Error for 47 energy groups Without Collimator along the Y-axis(cm) in the Collimator region. 83

5-18 2-D Neutron Flux Distribution Without Collimator for 47 energy groups along the Y-axis(cm) in the Collimator region. 84

5-19 2-D Neutron Flux Distribution Relative Error for 47 energy groups Without Collimator along the Y-axis(cm) in the Collimator region. 85

5-20 2-D Neutron Flux Distribution With and Without Collimator for 47 energy groups along the Y-axis(cm) Before Collimator region. 86

5-21 2-D Neutron Flux Distribution With and Without Collimator for 47 energy groups along the Y-axis(cm) Before Collimator region. 87

5-22 2-D Neutron Flux Distribution With and Without Collimator for 47 energy groups along the Y-axis(cm) Before Collimator region. 88

5-23 2-D Neutron Flux Distribution With and Without Collimator for 47 energy groups along the Y-axis(cm) in the Collimator region. 89

5-24 2-D Neutron Flux Distribution With and Without Collimator for 47 energy groups along the Y-axis(cm) in the Collimator region. 90

5-25 2-D Neutron Flux Distribution With and Without Collimator for 47 energy groups along the Y-axis(cm) in the Collimator region. 91

5-26 3-D thermal neutron flux distribution along the Y-axis(cm) south beam port before collimator region. 92

5-27 3-D thermal neutron flux relative error along the Y-axis(cm) south beam port before collimator region. 93

5-28 Contour 3-D thermal neutron flux distribution along the Y-axis(cm) south beam port before collimator region. 94

5-29 xy south beam port cross section 95

5-30 3-D epithermal neutron flux distribution along the Y-axis(cm) south beam port before collimator region. 96

5-31 3-D epithermal neutron flux distribution relative error along the Y-axis(cm) south beam port before collimator region. 97

5-32 3-D fast neutron flux distribution along the Y-axis(cm) south beam port before collimator region. 98

5-33 3-D fast neutron flux distribution relative error along the Y-axis(cm) south beam port before collimator region. 99

5-34 3-D thermal neutron flux distribution along the Y-axis(cm) south beam port collimator region. . . . 100

5-35 3-D thermal flux distribution relative error along the Y-axis(cm) south beam port collimator region. . . . 101

5-36 3-D fast neutron flux distribution along the Y-axis(cm) south beam port collimator region. . . . 102

5-37 3-D fast flux distribution relative error along the Y-axis(cm) south beam port collimator region. . . . 103

5-38 Neutron energy flux for different moderators region for 62 energy groups. . . . 104

5-39 Thermal neutron energy flux for three different moderators within 62 energy groups. . . . 105

5-40 Improvement of thermal neutron energy flux for the three different moderators within 62 energy groups. . . . 106

5-41 Fast neutron energy flux for three different moderators within 62 energy groups. 107

5-42 Improvement of fast neutron energy flux for the three different moderators within 62 energy groups. . . . 108

5-43 Neutron scattering cross sections for hydrogen, deuterium and C in H_2O, D_2O, and Graphite respectively. . . . 109

5-44 Neutron absorption cross sections for hydrogen and deuterium in H_2O and D_2O respectively. . . . 110

5-45 Neutron cross sections for hydrogen (H^1) . . . 111

5-46 Neutron cross sections for deuterium (H^2) . . . 112

6-1 MCNP5 calculations for ^{197}Au foils at 3 different locations. . . . 122

6-2 ^{197}Au (n,γ) ^{198}Au cross-section as a function of neutron energy . . . 123

C-1 Keff1. . . . 127

C-2 Keff2. . . . 128

C-3 Keff3. . . . 129

C-4 Keff$_{final}$. . . . 130

D-1 ^{232}Th fission cross-section versus neutron energy (MeV). . . . 131

D-2 ^{238}U fission cross-section versus neutron energy (MeV). . . . 131

D-3 ^{240}Pu fission cross-section versus neutron energy (MeV). . . . 132

D-4 ^{242}Pu fission cross-section versus neutron energy (MeV). 132

Abstract of Thesis Presented to the Graduate School
of the University of Florida in Partial Fulfillment of the
Requirements for the Degree of Master of Science

NEUTRON FLUX CHARACTERIZATION AND DESIGN OF UFTR RADIATION BEAM PORT USING MONTE CARLO METHODS

By

Romel Siqueira França

August 2012

Chair: DuWayne Schubring
Major: Nuclear Engineering Sciences

This research presents the characterization, modeling, and design of the UFTR (University of Florida Training Reactor) radiation beam ports for reactor analysis applications. Extensive validation of beam port is required. Using MCNP5 results were produced for the multigroup neutron flux distributions, neutron spectrum and neutron reaction rates.

Due to the strength of the neutron source in the reactor core, the neutron flux distribution and reaction rate can be monitored along the radiation beam port. The goal of the design in this research is to determine the neutron flux distribution, neutron energy flux and neutron reaction rate throughout the beam port.

The calculation of the neutron flux distribution, neutron spectrum and neutron reaction rates along the beam port were tallied. To compute the multigroup neutron flux distributions, and neutron energy flux FMESH4 and *F4 tallies were used, respectively. Sets of 47 and 62 energy groups were analyzed for these tallies. To calculate neutron reaction rates, the tally F4 along with the tally multiplier FM4 was used.

CHAPTER 1
INTRODUCTION

1.1 UFTR Reactor Background

The University of Florida Training Reactor (UFTR), was one of the first reactors built in a university in the United States of America. The UFTR was built in 1959 for education, research, and to train students to operate reactors. The UFTR operates at a maximum thermal power of 100 kW.

Details of fuel enrichment, mass, and geometry are excluded from this thesis for safeguards-related reasons. Detailed information on the UFTR fuel is available to all UFTR staff and those performing UFTR-related work. Accurate fuel parameters were employed in the present work

The UFTR presently uses a low-enriched Aluminum-Uranium Silicide (U_3Si_2 - Al) alloy meat with Aluminum cladding (composition in Appendix A and B). The main impurities in the UFTR nuclear fuel and graphite are ^{10}B and Cd which can impact neutron multiplication if their concentrations are changed [Appendix C], due to high neutron thermal absorption cross.

UFTR also uses two different neutron sources which are positioned in the vertical ports, near the center of the reactor. The first is a removable Plutonium Beryllium source (^{239}PuBe). The second is a regenerable Antimony Beryllium source (^{124}SbBe).

Tables 1-2 and 1-3 show the features of ^{239}PuBe and ^{124}SbBe neutron sources.

The UFTR also contains primary and secondary cooling systems .The primary system operates at all times that the reactor is critical. If the power is greater than 1 kW the secondary cooling system is required to cool the primary system. UFTR has four control blades. Three are safety control blades while the forth one is a regulating blade. The regulating blade is usually used for power adjustment.

The UFTR has three vertical ports going through the reactor core. They are used to place the neutron sources and sample irradiation. The vertical ports include, the

west vertical port (W.V.P.), the central vertical port (C.V.P.), and the east vertical port (E.V.P.). These three vertical holes are approximately 1.5 inches in diameter and are centrally positioned between six fuel compartments. Ports run through a large round removable plug that accesses a boral plate on top of the reactor graphite. See Figure 1-1 for vertical access plugs.

The graphite stringers are drilled out to the center of the core; these holes have removable graphite plugs. All nuclear fuel has graphite stringers around it.

Besides that, there is an east-west through port which barely touches the three vertical ports and this port is part of the RABBIT.

See Figure 1-2 for the RABBIT tube access.

UFTR also has radiation beam ports on the reactor center plane where the study of multi-group neutron flux distribution and neutron reaction rate will be performed. See Figures 1-3 for horizontal section of the UFTR at beam tube level.

1.2 UFTR Reactor Horizontal Beam Ports

The UFTR is composed of six horizontal radiation beam ports and one thermal column. The radiation beam ports were modeled with the Monte Carlo code MCNP5. Radiation beam ports are also used to perform sample irradiation and conduct special experiments . The reactor core is composed of six fuel boxes surrounded by graphite reflector used as a moderator.

The beam ports are surrounded by barytes concrete shielding as shown in Figure 1-3 which is used to reflect and absorb neutrons throughout the beam port. The beam ports are located in the north , northeast, northwest, south, southeast, and southwest sides of the reactor. The thermal column is located to the east side of the reactor. The beam ports are approximately 2.50 m deep with a cylindrical collimator resting at the end of the port.

1.3 UFTR Beam Port Challenges

The main complexity of this work was to achieve good statistics of the multi-group neutron flux distribution throughout the radiation beam port at different energies. This difficulty was addressed through of variance reduction, which is a very powerful tool used in Monte Carlo calculations.

Geometry Splitting and Geometry Splitting with Russian roulette worked very well. Cell importance was one of the variance reduction techniques applied, due to geometric characteristics of the problem. The neutron importance was increased by factor of two throughout these cells to keep the neutron population roughly constant. Neutron importance was chosen by looking at the neutron population. The source biasing or implicit capture was also applied to the problem.

Collimator

A collimator is a device that alters a stream of rays so that only those rays traveling parallel to a specified direction are allowed through. It has a long narrow tube with strongly absorbing material and reflecting walls (Figure 1-4). Diverging neutrons get repeatedly reflected or scattered and absorbed by the forming walls of the collimator.

The UFTR cylindrical collimator is mounted inside of the barytes concrete shielding [Appendix F] of the reactor, and can be removed as desired. The collimator is a long steel tube surrounded by barytic concrete with steel alloy on the outside (Figure 1-5). Barytic concrete is a low-cost shielding material that is effective even without the usual admixture of the neutron absorber boron.[16] This combination of scattering and absorbing material optimizes the shielding efficiency of a neutron diaphragm with respect to volume and weight.[6]

The concrete usually is made of 3% to 5% of ordinary water (H_2O) with low Z elements. Because ordinary water contains hydrogen (H^1) which absorbs neutrons, barytes concrete is commonly used for neutron shielding due to its low price. However, a large amount is required to shield a reactor.

The entrance and the exit of the collimator has a circular aperture of 2.54 cm with a approximately length of 1.4 m. The chemical composition of a collimator is shown in Table 1-1.

The collimator has a gap that is filled with air to allow the neutron beam to travel through it. It is possible to calculate the dose rate at the outside of the south beam port, which provides a neutron beam with a dose rate of 100 R/hr immediately following shutdown from power run.[13]

Figure 1-5 shows the 3D drawing of the cylindrical collimator, and Figure 1-7 shows its corresponding x-y projection of the MCNP5 model.

1.4 Research Goals and Objective

The primary goal of this research is to develop models for the determination of multi-group neutron flux distribution and neutron reaction rates throughout the radiation beam port. In addition analysis on the critical core configuration to investigate the combined effects of the impurities in the fuel and reactor structure was performed [Appendix C].

The specific objectives of this research were the following:

- Calculation of k_{eff} using MCNP5, and determination of neutron fission intensity distribution in each fuel box and in the whole reactor core using Watt fission Spectrum.
- Development of MCNP5 models for radiation beam port.
- Determination of multi-group neutron flux distributions for 47 energy-group structures throughout the radiation beam port using the FMESH4 tally option.
- Determination of neutron reaction rate for gold foil target using MCNP5.

Table 1-1. Collimator Composition

	Density (g/cm^3)	Temperature Limit (^{0}C)	Z
Steel Alloy	7.82	1400 ^{0}C -Very High	low
Barytes Concrete	3.1	$<$ 100 ^{0}C	low
Air	0.0011858	-	-

Table 1-2. PuBe and SbBe neutron sources features

PuBe	SbBe
Non-regenerable	Regenerable
1 Ci	10 Ci
Removable source	Removable source
Installed as needed/desired in C.V.P. or E.V.P.	Permanently installed in W.V.P.
Source alarm at 100 watts	High radiation tolerance

C.V.P. = Central Vertical Port, E.V.P. = East Vertical Port, W.V.P. = West Vertical Port

Table 1-3. Reactor power requirements for PuBe neutron source

PuBe
Prefer at 1 watt
Should be removed before 10 watts
Source alarm at 100 watts
Shall be removed before exceeding 1 kW

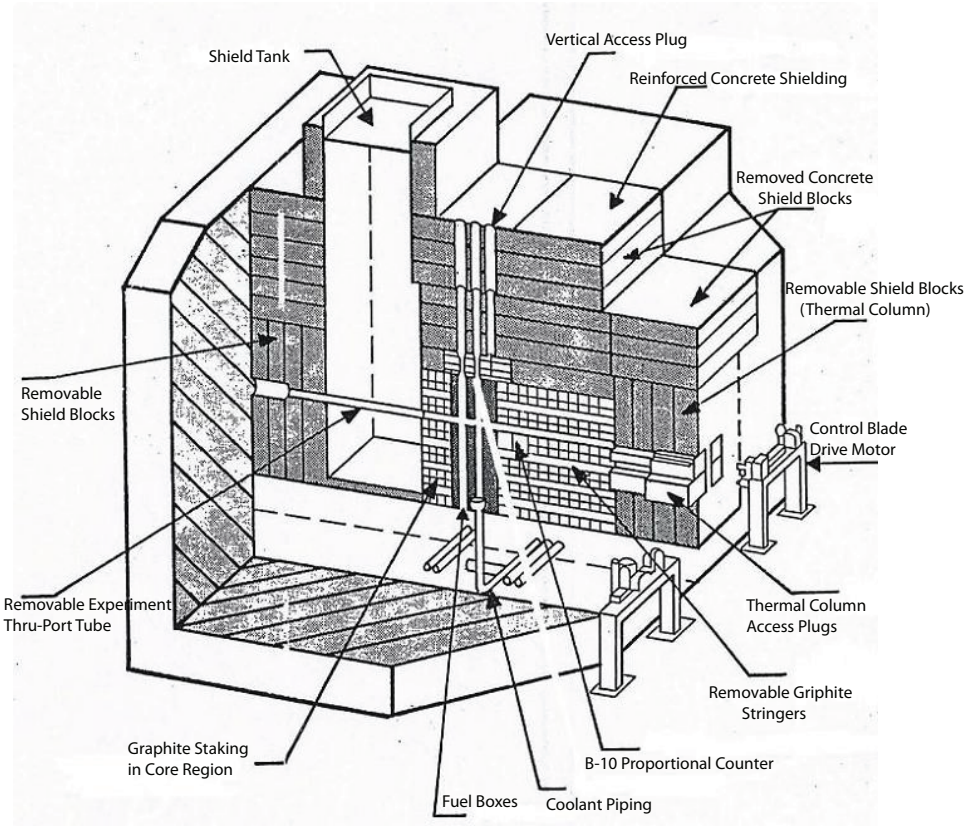

Figure 1-1. Axial projection of the UFTR, including all access ports.

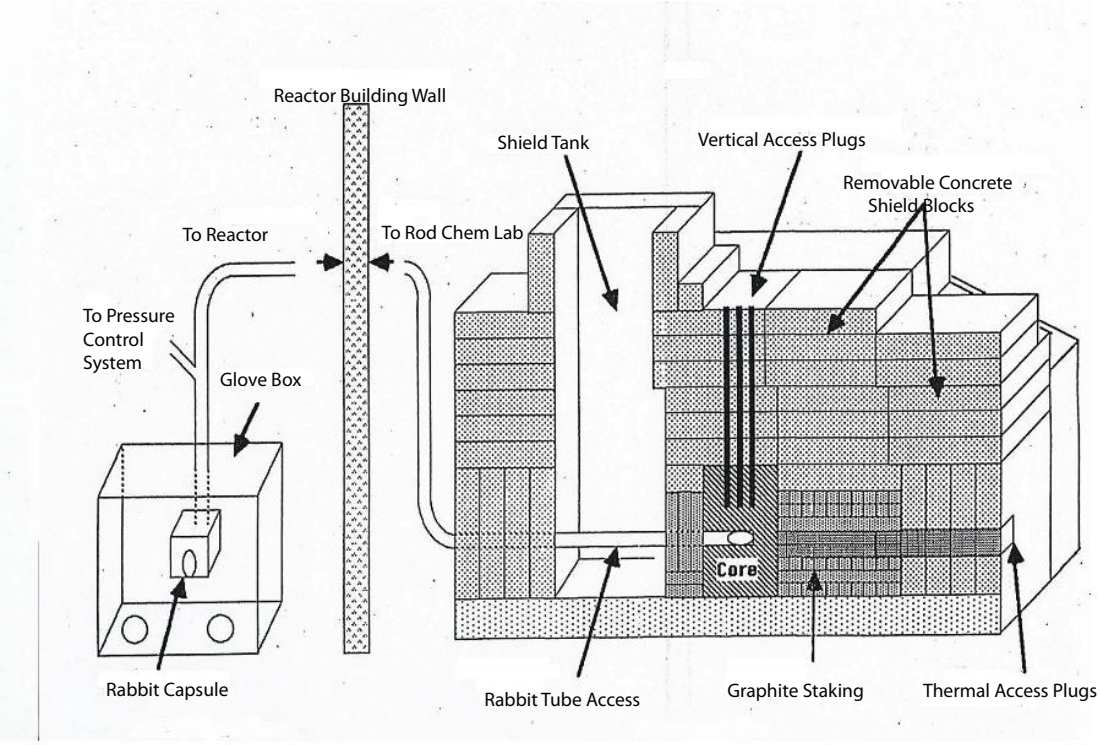

Figure 1-2. Axial projection of the UFTR with its RABBIT system.

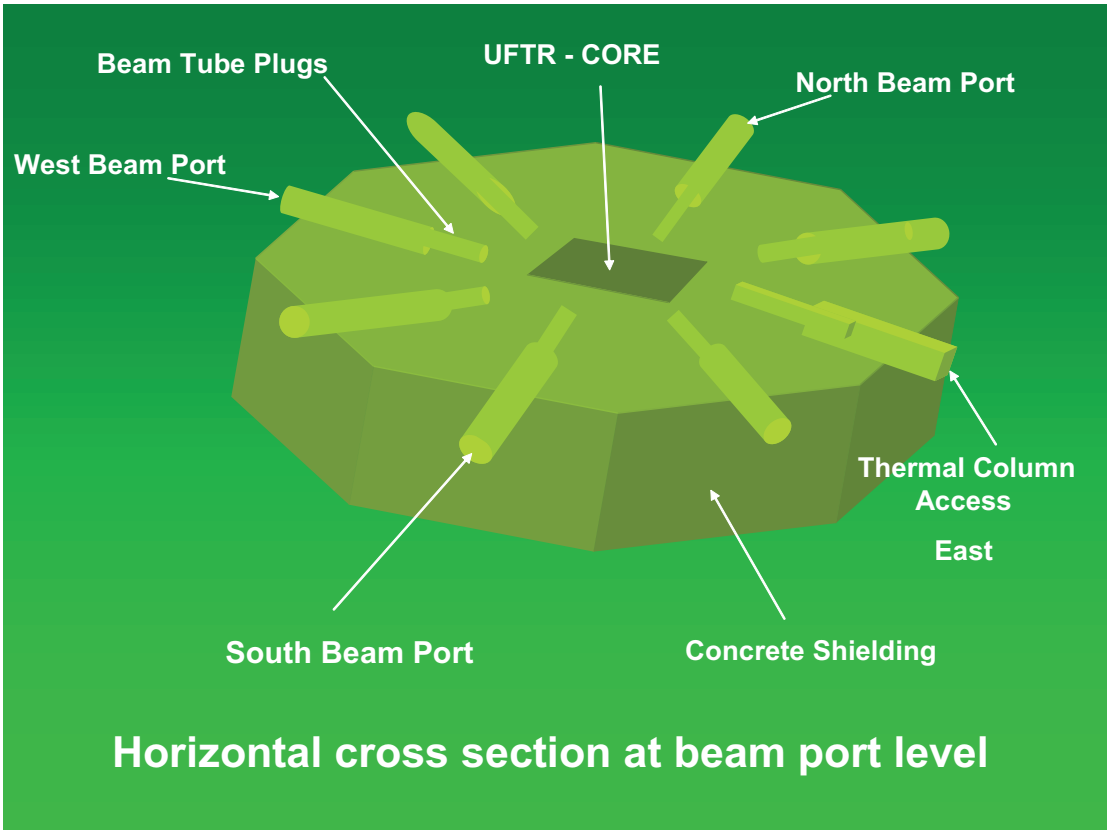

Figure 1-3. Horizontal beam ports drawing.

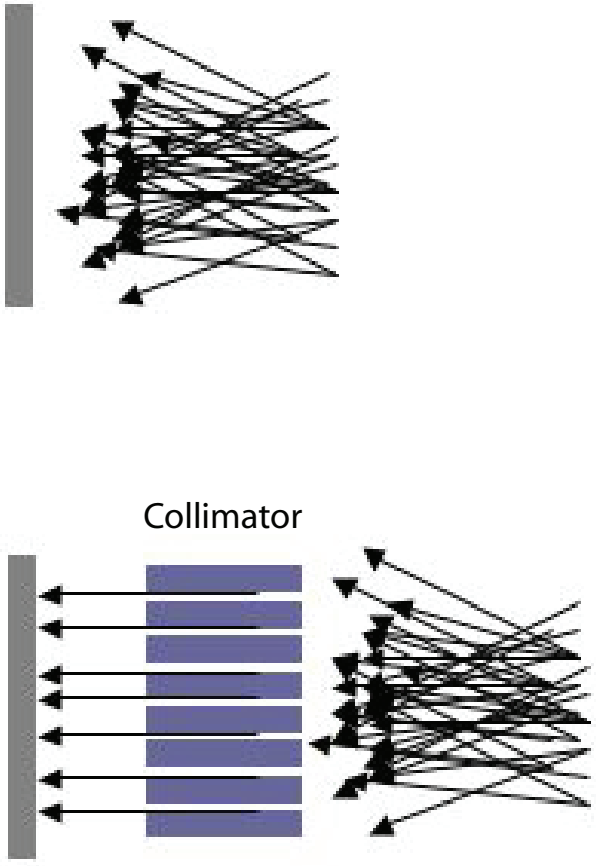

Figure 1-4. Collimator filtering a stream of rays in a general problem. Top without a collimator. Bottom with a collimator.

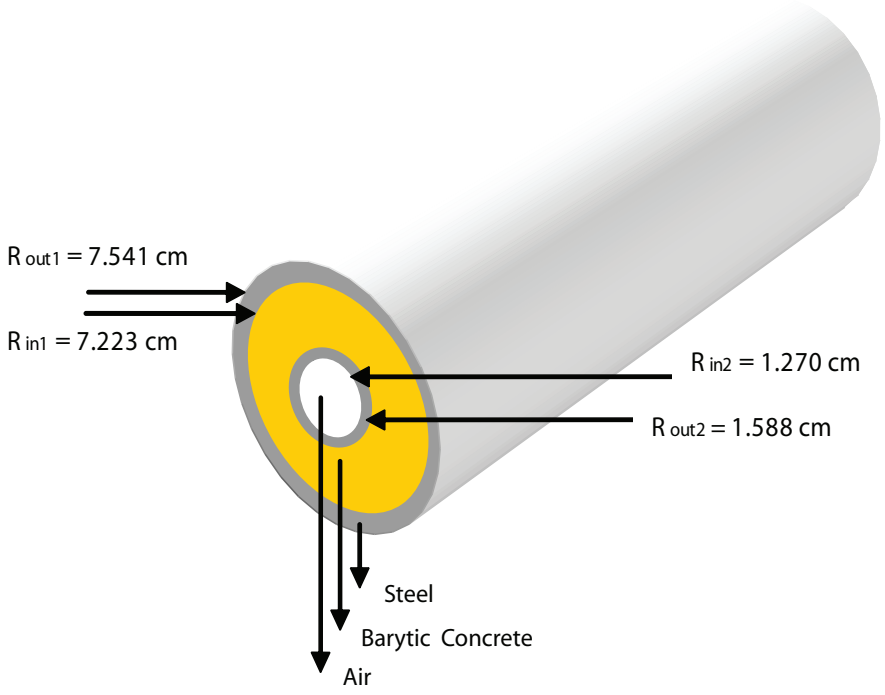

Figure 1-5. A Collimator 3D drawing.

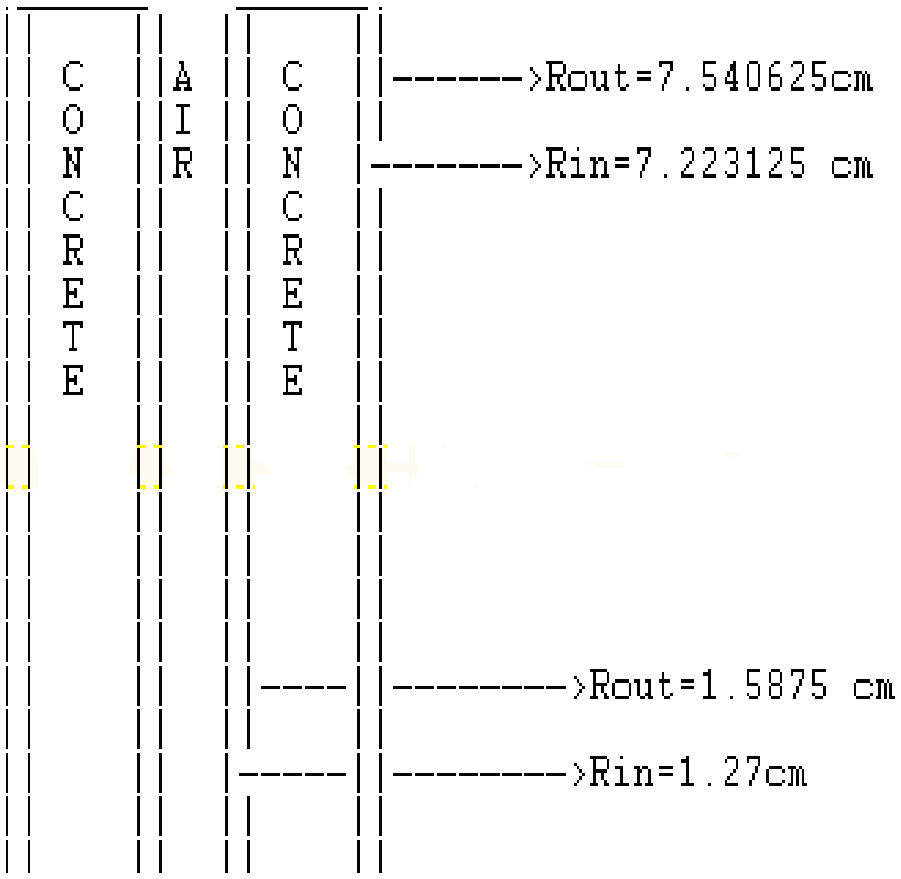

Figure 1-6. Collimator 2D projection.

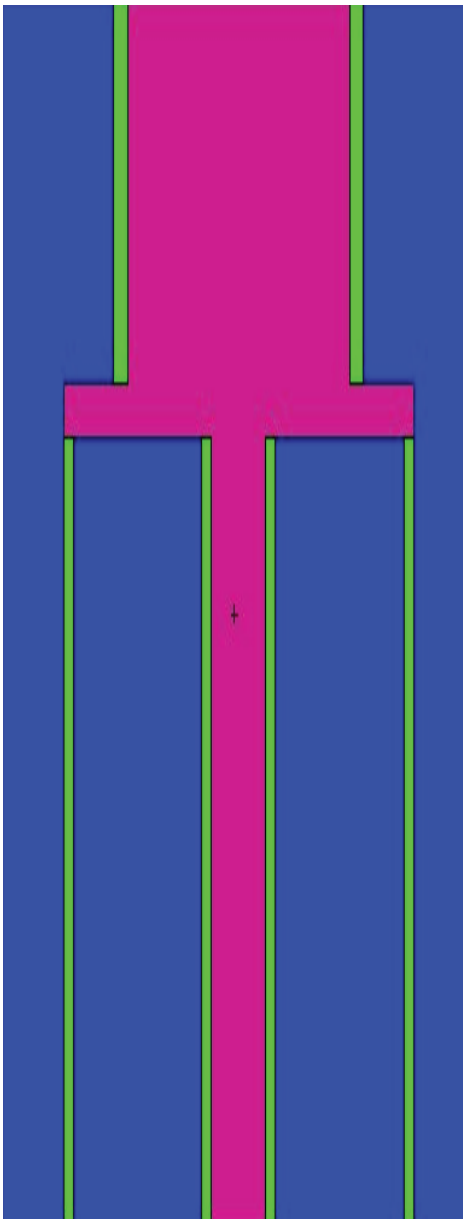

Figure 1-7. MCNP5 collimator x-y projection.

CHAPTER 2
REACTOR MODEL DEVELOPMENT

2.1 UFTR Reactor Model

This chapter discusses the University of Florida Training Reactor (UFTR) structure and measurements along with an explanation of its parts such as core and radiation beam ports. A two axial projections of the UFTR are shown in Figures 1-1 and 1-2.

UFTR Features

The UFTR is a light water (H_2O) and graphite moderated, water cooled reactor. The UFTR contains six horizontal beam ports, one horizontal thermal column, three vertical ports through the core, six vertical fuel boxes, graphite stacking, shielding blocks, and other geometrical features. The UFTR design features are specified to ensure that items important to safety are not changed without appropriate review.

The reactor is accommodated by a reinforced octagon shaped concrete cell with a total area of 30 ft x 60 ft square feet and 29 ft of head room. The specifications of the concrete biological shield are provided in Table 2-1.

Table 2-1. Shielding nominal specifications

Concrete shielding	Specifications
Sides, center	6ft., cast, barytes
Sides, end	6ft. 9 in. , cast, barytes
Middle	Barites concrete block
Top	5ft. 10 in.
End	3ft. 4 in.

2.2 UFTR Reactor Core Design

The UFTR core is composed of the six vertical fuel boxes as shown in Figure 2-1.

- S1 = Safety Blade ♯ 1
- S2 = Safety Blade ♯ 2
- S3 = Safety Blade ♯ 3
- RB = Regulating Blade
- F = Active Fuel Bundle
- D = Dummy Fuel Bundle

A full core model for the UFTR was generated with Hummingbird Exceed program and Monte Carlo Neutron Particle code version 5 (MCNP5) to obtain a complete detail for the reactor system components.

The reactor core's six fuel boxes are surrounded by reactor-grade graphite (yellow in Figure 2-1), that provides additional moderation. The 5ft x 5ft x 5ft (152.4cm x 152.4cm x 152.4cm) reactor grade graphite stringer is used to slow down neutrons released during fission and reflect neutrons back to the reactor core.

The six fuel boxes are arranged in two parallel rows of three boxes each, which are separated by about 30cm of graphite. In addition, the six boxes are flooded with light water. The water flows at a low mass velocity through the piping at the bottom of the fuel boxes, goes up through the fuel boxes cooling the core, and flows out of the core through the piping at the top.

2.2.1 UFTR Fuel Box

The UFTR core is composed of 6 vertical fuel boxes made of aluminum and filled with H_2O. There are up to four fuel bundles for each UFTR fuel box (*i.e*, a total of $6 \times 4 =$ 24 fuel bundles); two of the boxes contain a dummy bundle as shown in the Figure 2-1. Each fuel bundle contains 14 plates.

2.2.2 UFTR Fuel Plate

The UFTR fuel plate is made of Aluminum cladding due to its low absorption cross-section with a dimension of (0.635cm x 0.0381 cm x 2.54cm). The fuel bundle is composed of fourteen plates containing low-enriched Uranium Silicide (U_3Si_2) [Appendix A] and Aluminum [Appendix B].

2.3 Reactor Radiation Beam Ports Modeling

The reactor is surrounded by a concrete wall. The beam port consists of a cylindrical port varying in diameter along the length from the core to the outside of the concrete wall. There is a collimator plug which consists of a concrete plug with a 2.54 cm diameter steel alloy about the center as shown in Figure 1-5. When the beam port is not being used, a solid concrete plug replaces the collimator plug. Measurements for the beam port geometry are taken from blue prints of the UFTR and verified by physical measurements when appropriate. See Figure 2-2 for UFTR radiation beam ports.

UFTR Reactor South Beam Port

The model of the reactor south beam port runs in the south direction (-y direction) from -28.654 cm to -279.38 cm and in the north direction (+y direction) from 28.654 cm to 279.38 cm. The surface source for the model was taken from UFTR full core model surface tallies at y= -28.2575 cm. Calculations are done with and without the insertion of the collimator plug and discussed in chapter 5.

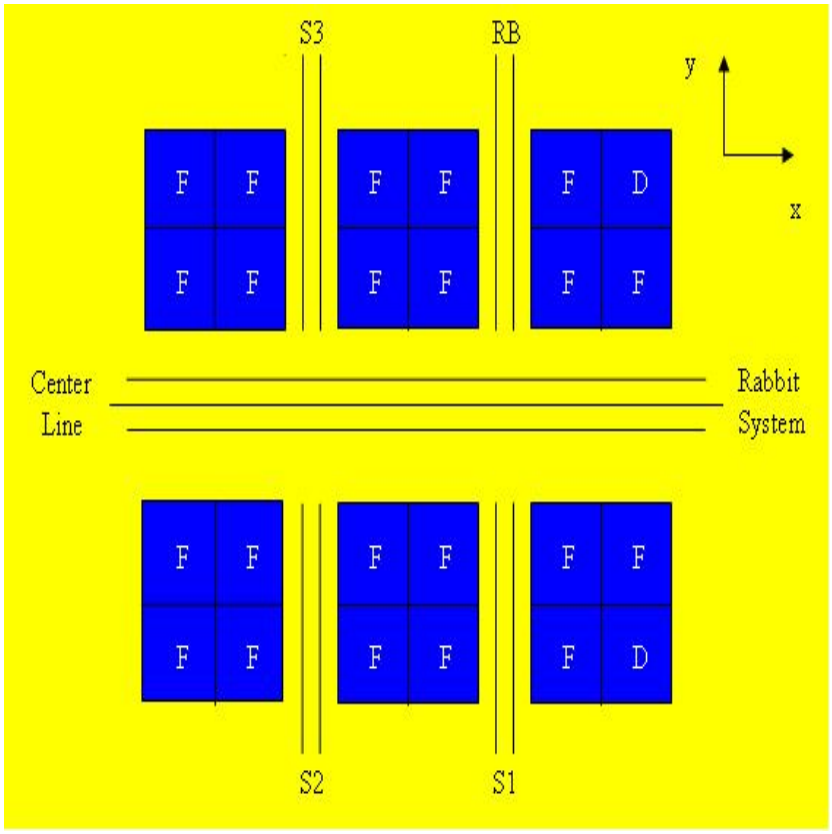

Figure 2-1. Radial projection of the UFTR core illustrating the fuel and the fuel box arrangement as surrounded by graphite stringers.

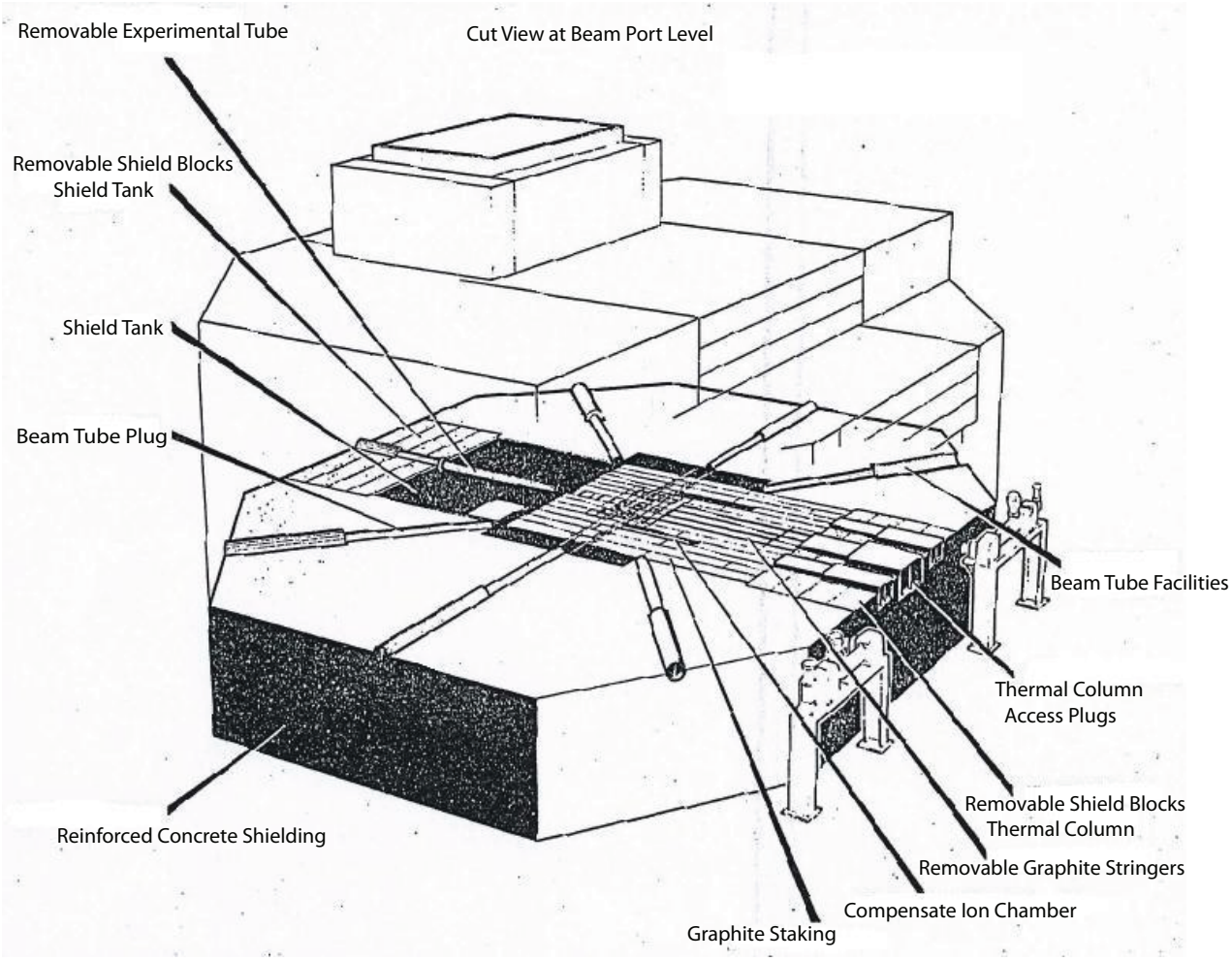

Figure 2-2. Horizontal section of the UFTR at beam tube level.

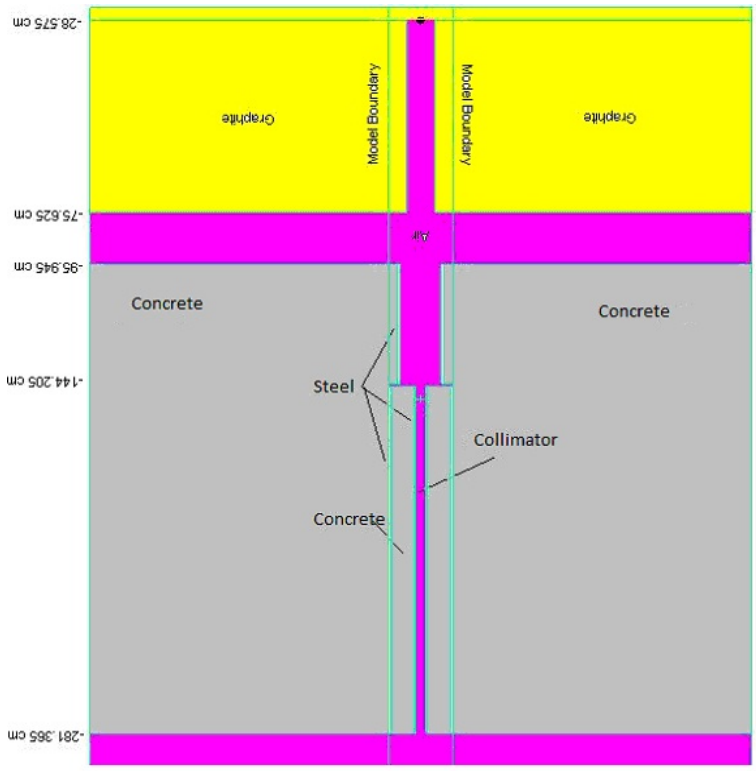

Figure 2-3. South beam port measurements.

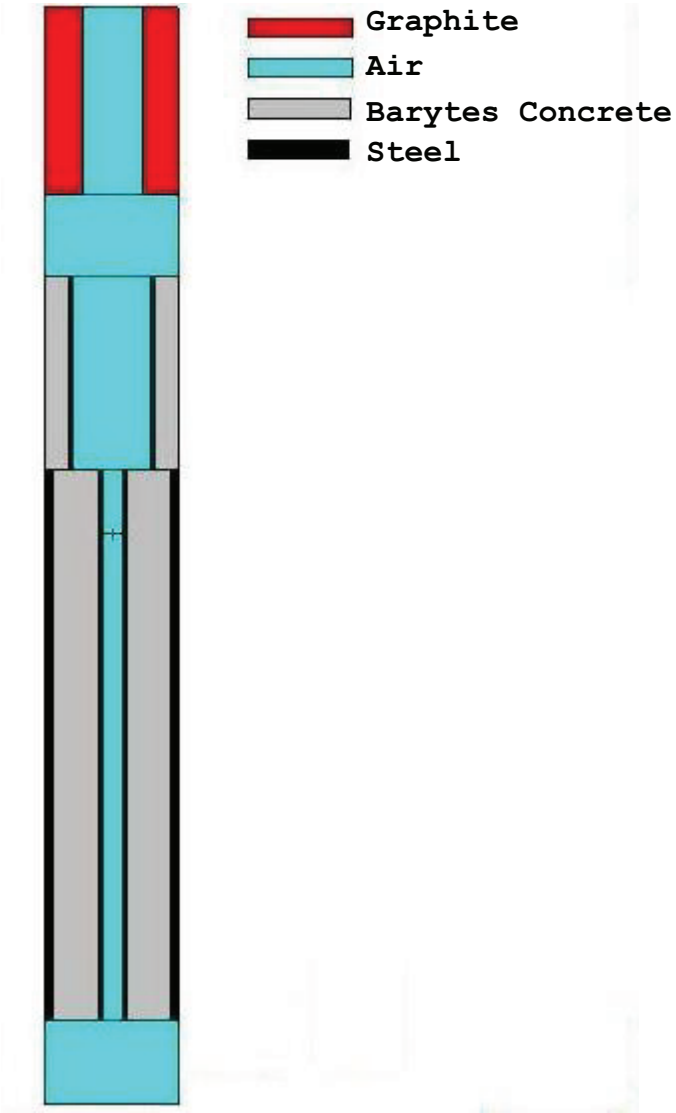

Figure 2-4. MCNP model with materials, generated with MCNP Visual Editor (VisEd).

CHAPTER 3
MCNP5 BACKGROUND AND CALCULATIONS

3.1 General Features of MCNP5

Monte Carlo is a stochastic method well-suited to solve complicated three dimensional and time-independent neutron transport problems. The Monte Carlo technique is pre-eminently realistic (a theoretical experiment). Further details of the Monte Carlo method as used in MCNP5 can be found in the MCNP5 manual.

3.2 UF Cluster PC Computers

The MCNP5 code was run on an 8 node (16 processor) cluster with the following features:

- AMD Dual Opteron processors at 2.4 Ghz
- 8 GB DDR RAM per node on a 533 Mhz system bus.
- 1000 Mbit full duplex network interfaces.
- 8-port keyboard, video, mouse (KVM) switch.

3.3 MCNP5 Deck

The geometry of the full reactor model was created in a 3D Cartesian coordinate system to give a better view of the geometry. A MCNP5 deck was built and run with Exceed (version 6.1) used to acquire the geometry plots.

The first step of this research was to model the authentic radiation beam port in MCNP5. The six horizontal beam ports were set up in the model such that their position can be adjusted based on the actual reactor operations. The ports were placed in the model by using the TRn card (coordinate transformation). After that, the beam port designs were attached to the UFTR core design provided. Plots of these designs were made with Exceed.

The second step was the calculation of the core multiplication (k_{eff}) and the collection of neutron fission source results from the six fuel boxes of the UFTR core. The k_{eff} was found with MCNP5 using KCODE. To collect the neutron fission source density distribution at fixed points, the Watt Fission Spectrum input was used with

KCODE and KSRC cards, where the KSRC card was used to fix the location of the initial neutron fission source in the six fuel boxes in the reactor core.

The third step was (a) determination of multi-group neutron flux distribution and neutron flux intensity for 47 energy groups throughout the radiation beam port, and (b) determination of neutron reaction rate for gold foil target.

3.3.1 Criticality Determination

The following is a verification of the overall criticality analysis of the University of Florida Training Reactor (UFTR) core model using MCNP5. The deck was run as a KCODE source problem for criticality calculations. The KCODE card specifies the MCNP5 criticality source that is used for determining k_{eff}. This requires KSRC or SDEF or SRCTP files for the initial spatial fission source and use enough settle cycles to reach fundamental spatial mode.

The KCODE source card values were set as shown in Table 3-1. The initial source points for KCODE calculations were set as 3 points (x_i y_i z_i) per fuel plate using the KSRC card.

Table 3-1. KCODE values - Criticality Source Card

Parameters	Values
Number of particle histories per cycle	5×10^4
Number of skipped cycles	100
Total number of cycles	800

3.3.2 Fixed Source Methods Applied

Once the deck was run as a KCODE source problem, the source can be expressed using two different methods:

1. Fixed Source Method with SSR card (by RSSA file)
2. Fixed Source Method with SDEF card

The second method was employed, as discussed in the next section

3.3.2.1 Fixed source method with surface source read (SSR)

To obtain the neutron source, on a MCNP5 calculation was performed using the criticality source KCODE card, the KSRC source points card for a fixed source problem, and the surface source write (SSW) card to acquire the WSSA surface source file.

For KCODE calculations, particles are written only for active cycles. The SSW card was used to obtain the source information. This card is used to write a surface source file or to write a KCODE fission volume source file for use in a subsequent MCNP5 calculation.

The SSW in this case was used to write the KCODE fission value source file and it was used in the junction of the reactor core with radiation south beam port.

In a KCODE calculation, the fission neutron sources and prompt photons produced from fission during each cycle are written to the WSSA file. Calculation to a WSSA file is done with a CEL option on a SSW card. The fission source is written by the KCODE card. Particles crossing specified surfaces can also be written by specifying S_i (problem surface number). In this case, SSW used surface -20 (Table 3-2).

Particle-crossing information is written to the WSSA file. A track that crosses a certain surface in the correct direction will be recorded only if it enters or leaves the right cell. During execution, surface source information is written to the scratch file WXXA. Upon normal completion, WXXA becomes WSSA. The simulation to get the WSSA source card for the reactor core was carried out using the information of original run from Table 3-2.

The values of the SSW/SSR cards were set as follows:

Table 3-2. Surface source write (SSW) and surface source read (SSR) cards

	Surface Card	Surface
Reactor core run - original run	SSW	-20
South beam port run - current run	SSR	old 20 new 500

The surface 20 and surface 500 are set at position py -28.575 of the junction of the reactor core and the south beam port.

Then, the particles were sent throughout the south beam port to obtain the multi-group neutron flux distribution. Due to poor statistics achieved on the multi-group neutron flux distribution calculations when using the FMESH4 card for 47 energy groups, the Fixed Source Method with SDEF card was used instead. Multi-group neutron flux distribution is discussed on chapter 4.

3.3.2.2 Fixed source method with SDEF

To determine a neutron fission density distribution in the MCNP5 code, a criticality source KCODE calculation is performed. A KSCRC source points card is used for a fixed source problem with neutron fission energy sampled from the Watt fission spectrum.

To tally neutron fission source density for each fuel plate, 100 meshes were defined. Five meshes across the width of the plate, one mesh representing the thickness, and twenty meshes axially.

The 3-D neutron fission density distribution ($\sharp/\text{cm}^3$-sec) plots throughout the six fuel boxes is represented in the Figs. 3-1, 3-2, 3-3 and 3-4.

To generate the spectrum of the neutron fission source distribution, a fission spectrum was generated based on the continuous energy Watt spectrum formulation [9]. The MCNP5 Watt fission spectrum continuous energy form is given by Eqn. 3–6. The verified fission spectra form is obtained by plotting (Fig. 3-10) Eqns. 3–1 and 3–6 over the energies of the 47 energy groups [Appendix E] in the BUGLE-96 cross-section library [15]. The spectra in Fig. 3-10 are not identical due to ^{235}U enrichment differences.

The derivative of the *fission spectrum*, $\chi(E)$, in respect to E is defined as the average number of fission neutrons emitted per unit energy with energy E in E to E+dE and expressed by

$$\chi(E) = 0.453e^{-1.036E} \sinh \sqrt{2.29E} \tag{3–1}$$

$\chi(E)$ represents the fission spectrum when thermal neutrons induce fission in ^{235}U. The fission spectrum of ^{235}U is preferred over the fission spectrum of ^{238}U due to $\sigma_f^{235} \gg \sigma_f^{238}$ along the energy distribution (Fig. 3-11). The group-wise neutron fission source distributions for 47 [Appendix E] energy groups are shown in the Figs. 3-6, 3-7, 3-8, and 3-9.

Performing a criticality calculation followed by a fixed source calculation (compared to only performing a criticality calculation) allows significant reduction of computation time since a properly converged source is assumed to be obtained from the criticality calculation, any subsequent calculations can be performed by using the more computationally efficient fixed source simulation.

The fixed source requires one of the three cards:

- SDEF
- SSR (with RSSA file)
- User defined source subroutine

Here, SDEF was used in combination with *si* (source information) and *sp* (source probability). Once obtained the neutron fission source, the source was collected and set to a new file for a second run with SDEF card where *si* is the fixed source locations from KSCRC card, and *sp* is the neutron fission source values.

SDEF was set as

sdef pos=d1 erg=d3 VEC=0 -1 0 dir= 1

si x_1 y_1 z_1 x_2 y_2 z_2 ...

sp a_1 b_2 c_3 d_4 ...

Three different methods were applied to obtain more efficient results in the calculation of *multi-group* neutron flux distribution through out the radiation south beam port:

1. A single shot of the fixed source was given using the SDEF card. Total simulation time was $\approx$ 24 days
2. A single shot of the fixed source was given using the SDEF and phys:n cards. The phys:n card was used to reduce neutron absorption in the collimator region. Total simulation time was $\approx$ 9 days.
3. A single shot of the fixed source was given using the SDEF and phys:n cards up to the beginning of the collimator region. Then the SSR and phys:n cards were used for the second run. Total simulation time was $\approx$ 8 hours.

The SSR card was used to write the surface source file instead to write a KCODE fission volume source file as in the previous section.

In conclusion, the combination of the fixed source method with SDEF and SSR cards showed to have a better statistics results for the relative error than the SSR method by itself when the source was shot throughout the radiation south beam port to calculate the multi-group neutron flux distributions.

MCNP Watt Fission Spectrum. The energy dependent Watt fission spectrum (Fig. 3-10) has two functions a(E_1) and b(E_1) which are tabulated with incident energy. The spectrum is calculated using the following equation:

$$g(E_1, E_2) = \frac{e^{-E_2/a}}{I} \sinh(\sqrt{bE_2}) \tag{3–2}$$

Where:

$$I = \frac{1}{2}\sqrt{\frac{\pi a^3 b}{4}} e^{x_0}[erf(\sqrt{x} - \sqrt{x_0}) + erf(\sqrt{x} + \sqrt{x_0})] - ae^{-x\sinh(abx)} \tag{3–3}$$

$$x = \frac{E_1 - U}{a} \tag{3–4}$$

Table 3-3. Possible MCNP5 constants for the Watt Fission Spectrum

Neutron Induced Fission	Incident Neutron Energy(MeV)	a(MeV)	b(MeV^{-1})
n + ^{235}U	Thermal	0.988	2.249
"	1	0.988	2.249
"	14	1.028	2.084
n + ^{238}U	Thermal	0.88111	3.4005
"	1	0.89506	3.2953
"	14	0.96534	2.8330

$$x_0 = \frac{ab}{4} \tag{3–5}$$

The range of final energies allowed is from zero to E_1-U, where U is a constant from the library. However, the Watt fission spectra in the Evaluated Nuclear Data Library, ENDL [7] is defined by a simple analytical function [12]:

$$f(a, b, E_2) = Ce^{-E_2/a}\sinh(\sqrt{bE_2}) \tag{3–6}$$

where

$$C = \sqrt{\frac{4}{\pi a^3 b}}e^{-ab/4} \tag{3–7}$$

and E_2 is the secondary neutron energy. The coefficients a and b vary weakly from one isotope to another (Table 3-3). The constants for neutron-induced fission are taken directly from the ENDF/B-V library. A typical *prompt* neutron fission spectrum of ^{235}U is given by Eqn. 3–1; it will be used to represent the verified Watt fission spectra (Fig.3-10).[4]

Uranium ^{235}U and ^{238}U .^{238}U undergoes a fission only when struck with a neutron of 1 MeV or more. Even though this fissionable nuclide plays an important role in nuclear fuel, is unable to sustain a stable fission chain reaction by itself and hence must always be used in combination with a fissile nuclide such as ^{235}U or ^{239}Pu. Fissile nuclides represent the principal fuels used in fission chain-reaction systems.

Figure 3-11 shows the total fission cross-section features of the fissile and fissionable nuclides present in the UFTR. The data were acquired from ENDF/B-VII at a temperature of 300°K (26.85°C). The ^{235}U fission cross section has a considerably different behavior than fissionable nuclide ^{238}U the entire energy range.

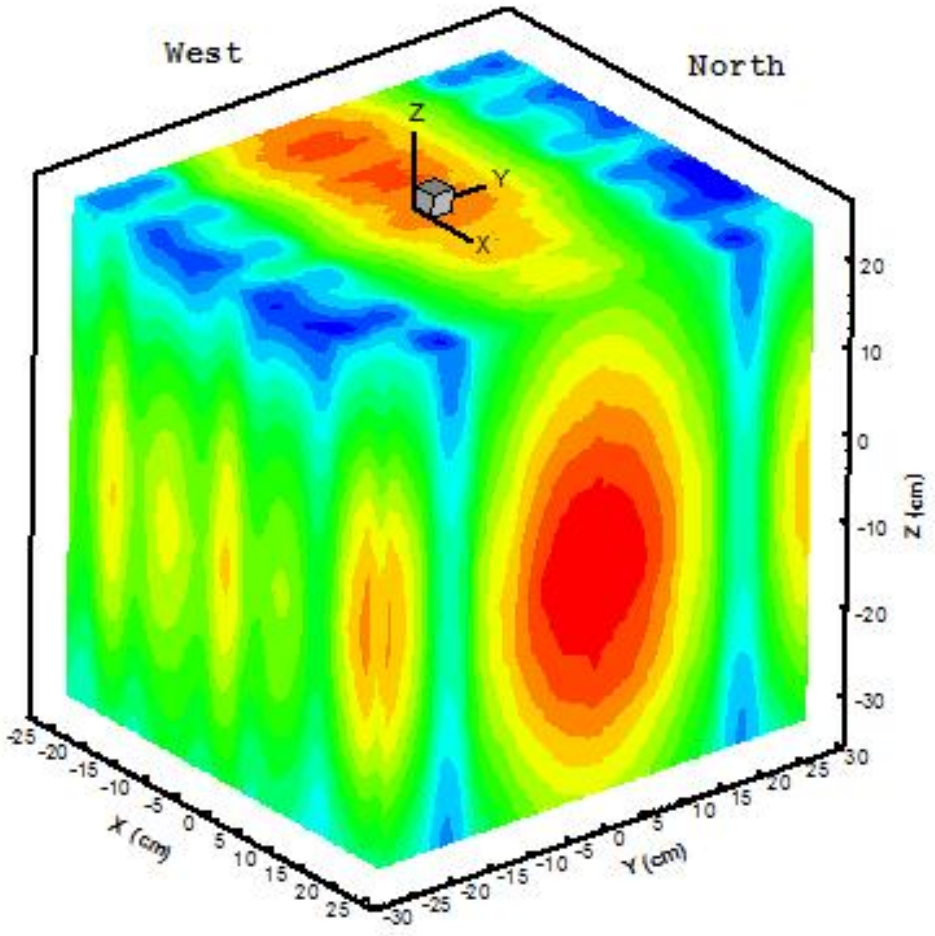

Figure 3-1. Neutron fission density distribution ♯/cm^3-sec for top view of the UFTR core.

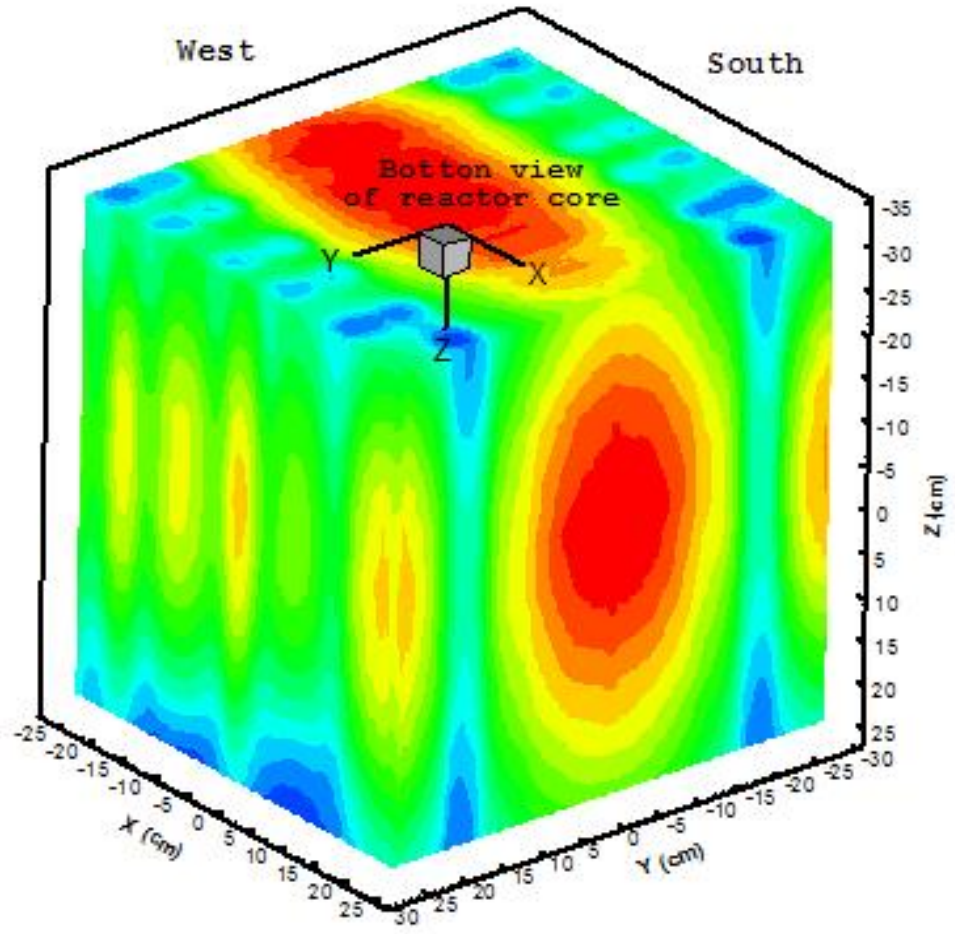

Figure 3-2. Neutron fission density distribution $\sharp/cm^3$-sec for bottom view of the UFTR core.

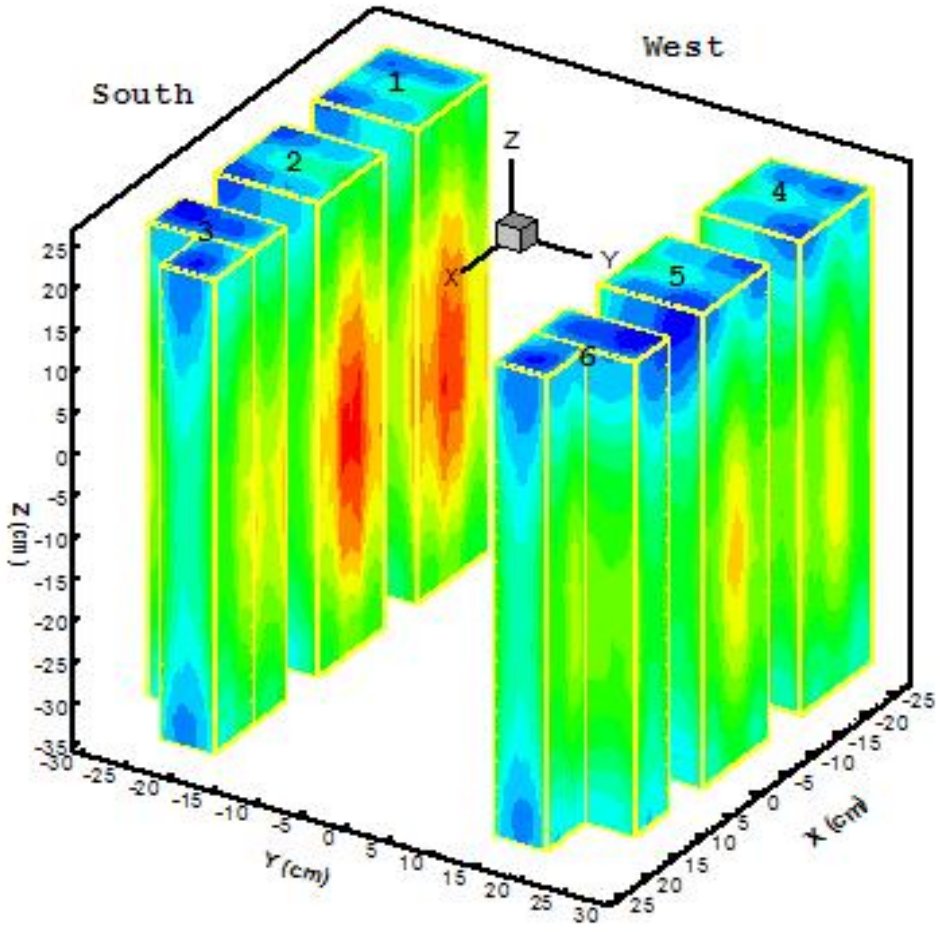

Figure 3-3. Neutron fission density distribution $\sharp/cm^3$-sec within six UFTR fuel boxes numbered from one to six showing the south view.

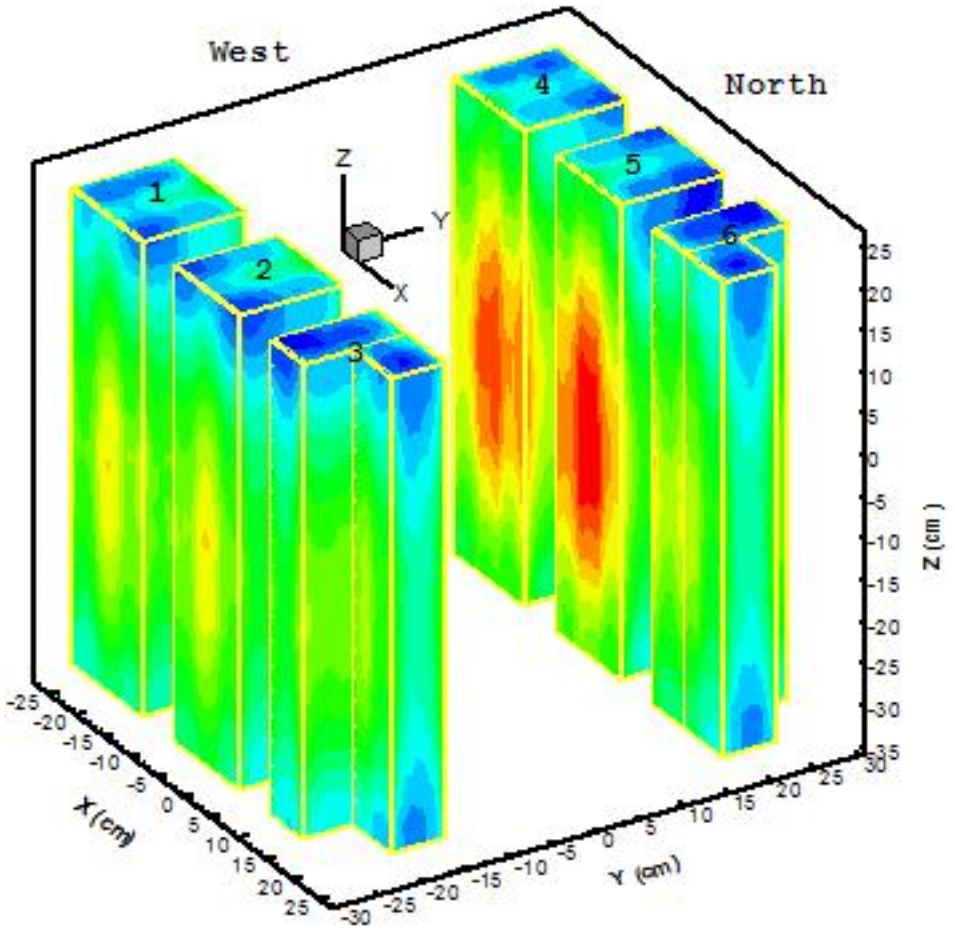

Figure 3-4. Neutron fission density distribution ♯/cm^3-sec within six UFTR fuel boxes numbered from one to six showing the north view.

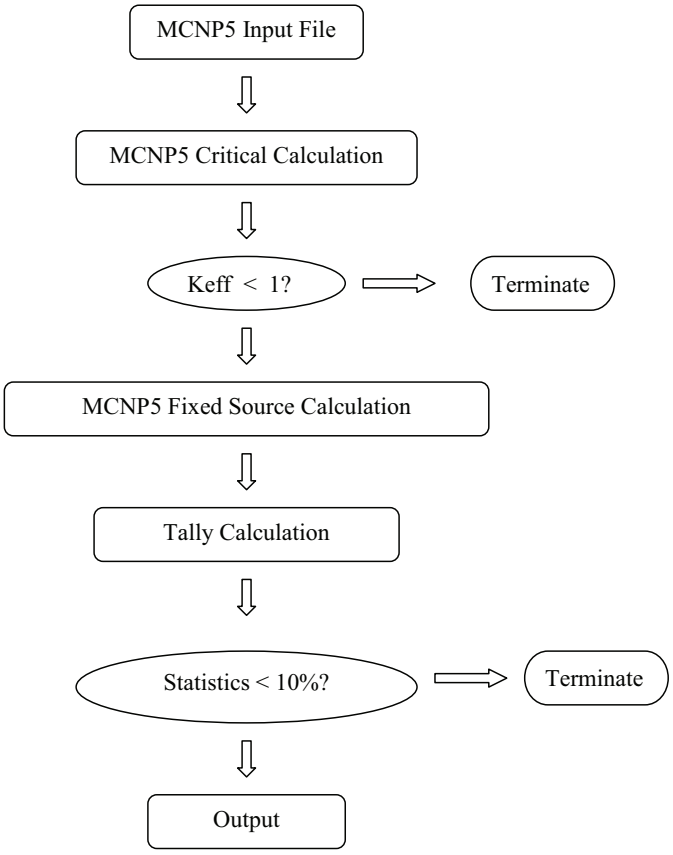

Figure 3-5. Flow chart calculation.

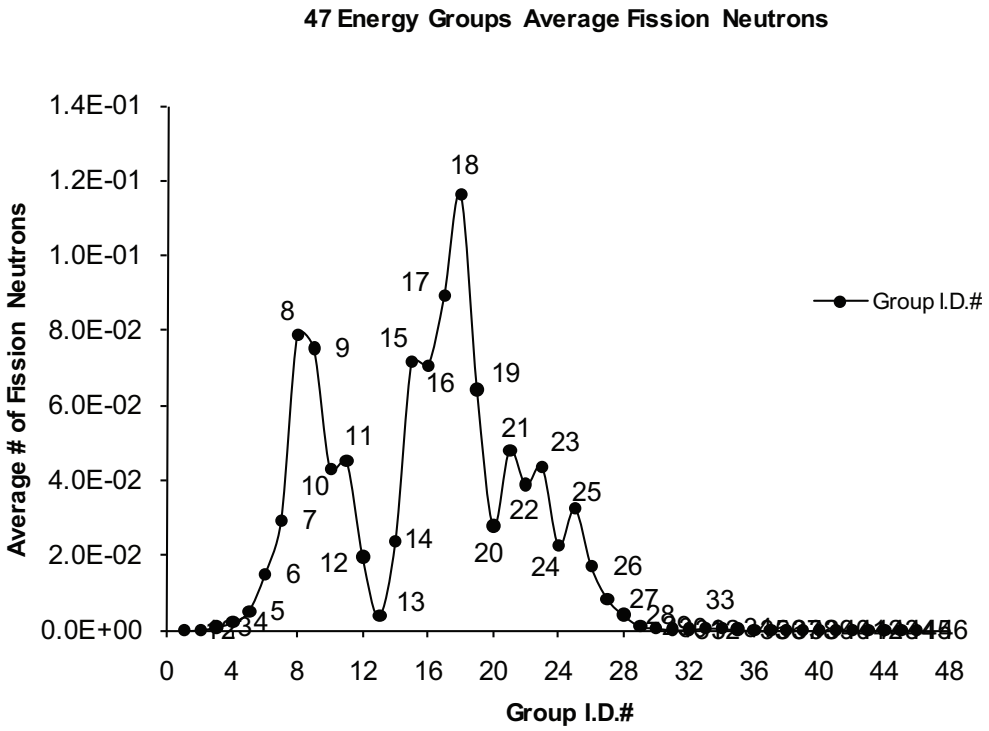

Figure 3-6. Average Fission Neutrons per group for Thermal Neutrons Fission in ^{235}U.

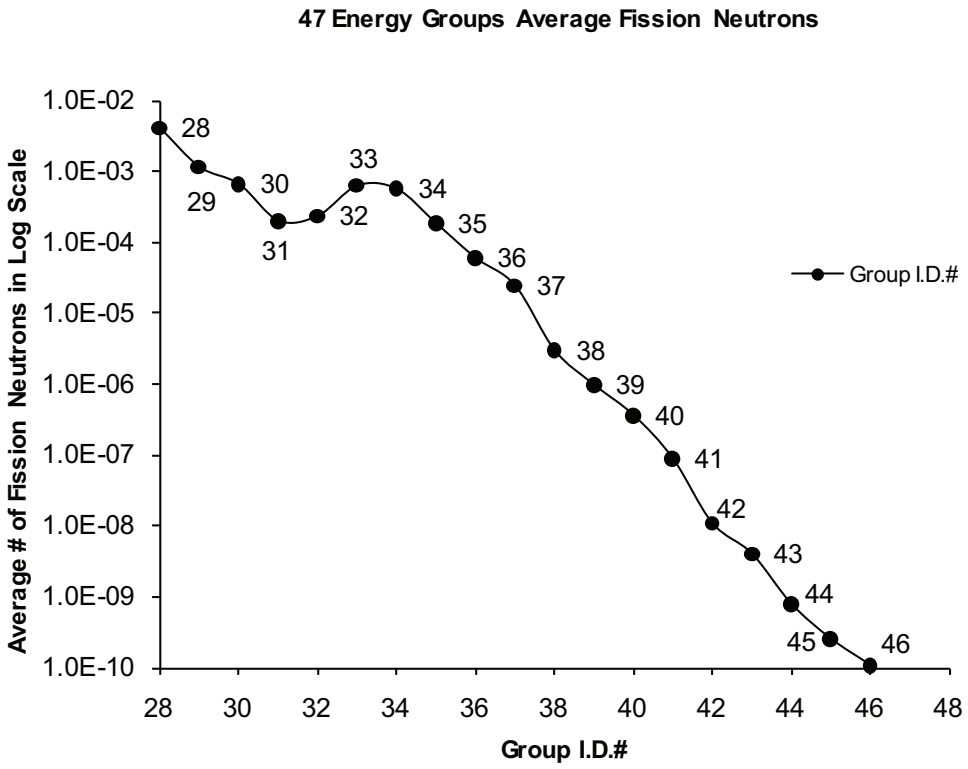

Figure 3-7. Average Fission Neutrons per group for Thermal Neutrons Fission in ^{235}U (Log Scale).

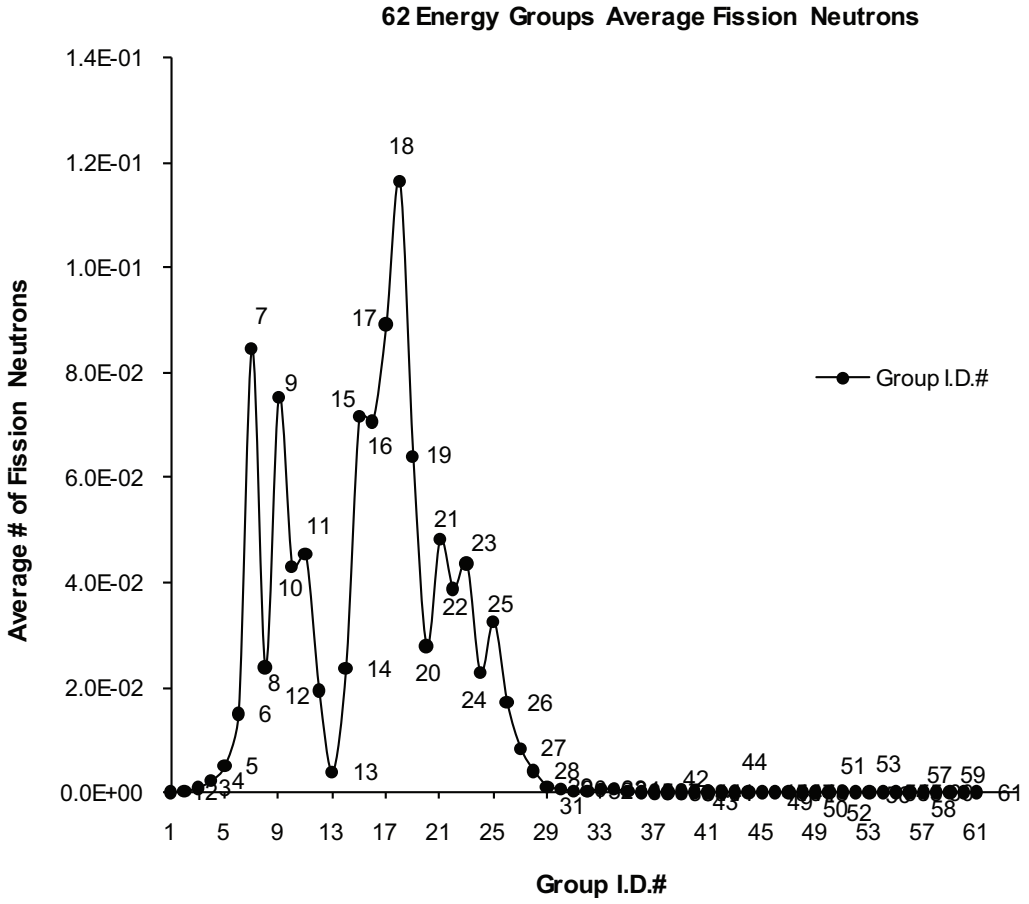

Figure 3-8. Average Fission Neutrons per group for Thermal Neutrons Fission in ^{235}U.

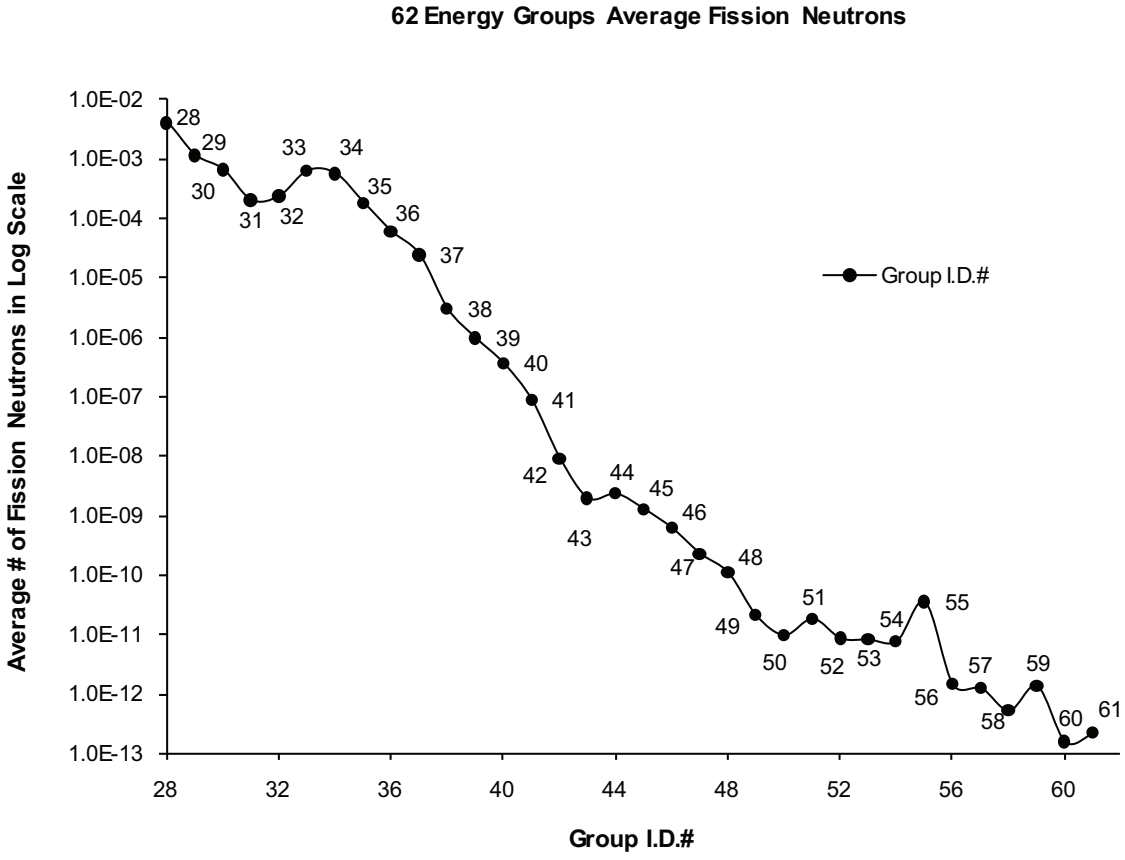

Figure 3-9. Average Fission Neutrons per group for Thermal Neutrons Fission in ^{235}U (Log Scale).

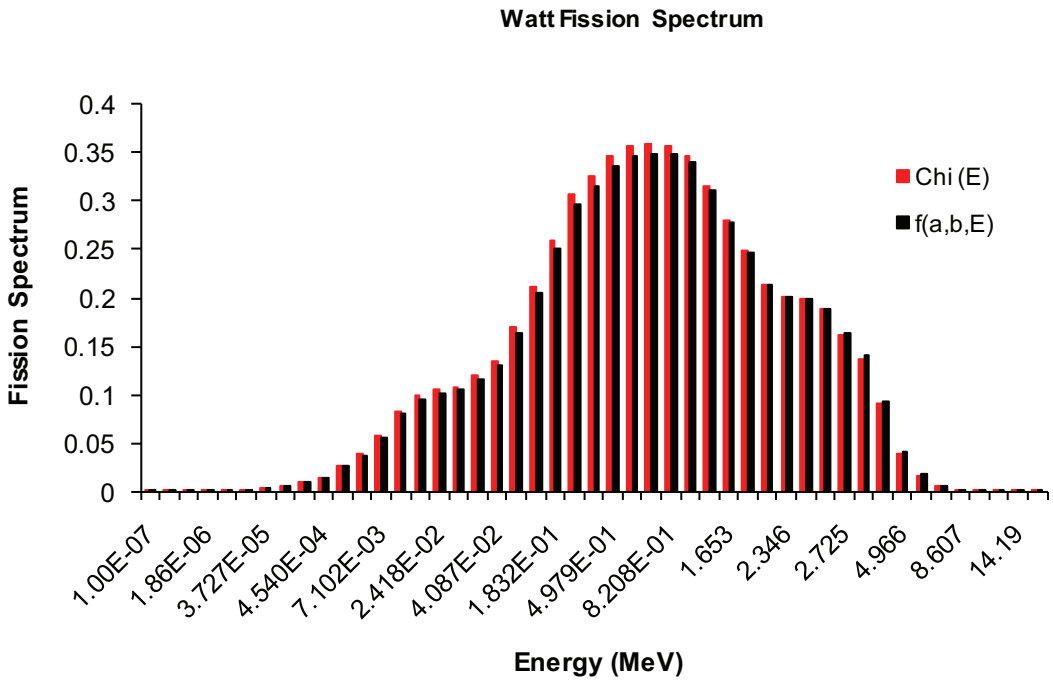

Figure 3-10. The Watt Fission Spectra when Thermal Neutrons Induce Fission in ^{235}U for $\chi(E)$ and f(a,b,E) (where a $=$ 0.988 b $=$ 2.249).

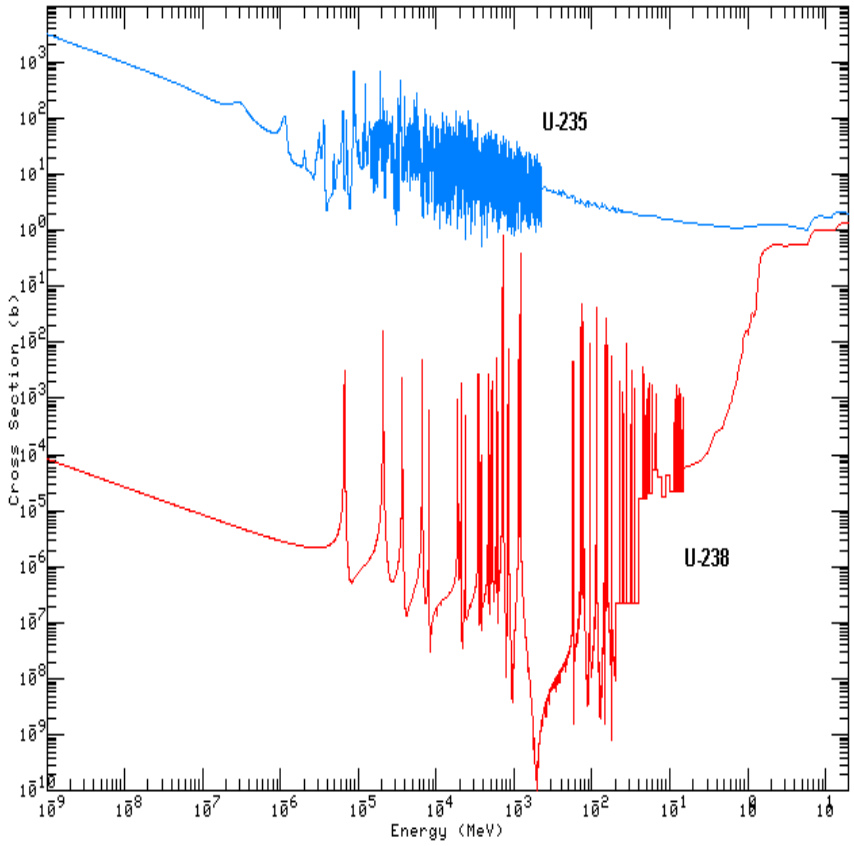

Figure 3-11. Schematic Neutron Fission Cross Section for U_{92}^{235} and U_{92}^{238} (Log Scale).

CHAPTER 4
MCNP5 MATHEMATICAL AND THEORETICAL DISCUSSION

4.1 General Features of MCNP5

The Monte Carlo N-Particle transport code version 5.0 (MCNP5), is a general purpose, continuous-energy, general geometry, time-independent Monte Carlo transport code. MCNP5 is a general Monte Carlo radiation transport code capable of transporting neutrons, photons, and electrons through virtually any material provided problem geometry.

The Monte Carlo method was developed during the 1940s. Random samples of parameters or inputs are used to assess the behavior of a complex system or process. Monte Carlo methods are frequently used when the model is complex, nonlinear, or involves many uncertain parameters.

4.2 F4 Tally

At the initiation of a particle from a source point, a particle track is created. The track refers to each component of a source particle during its entire history. A tally of particle track length in a given space is used in MCNP5 to calculate flux. Further tallying of the collisions along the track length are used to compute reaction rates and for source generation in KCODE calculations.

Let the following variables to be defined as:

- $\overrightarrow{r}$ = particle location in space
- E = particle energy
- t = time
- $\overrightarrow{\Omega}$ = unit vector in direction o particle motion
- Ψ = particle angular flux
- v = particle speed
- s = track length
- V = volume (cm^3)
- N = particle density ($\sharp/cm^3$)

The F4 tally in MCNP5 will converse to the following:

$$F_4 = \frac{1}{V}\int_V \int_t \int_E \Phi(\overrightarrow{r}, E, t)\, dE\, dt\, dV \tag{4–1}$$

Scalar flux is defined as the integral of angular flux over all directions,

$$\Phi(\overrightarrow{r}, E, t) = \int_{4\pi} \Psi(\overrightarrow{r}, \widehat{\Omega}, E, t)\, d\widehat{\Omega} \tag{4–2}$$

to calculate nuclear reaction rates and hence the chain reactions. The scalar flux is also a function of position, energy and time. The angular flux is useful for the calculation of reactions rates and of boundary crossings. It is defined as:

$$\Psi(\overrightarrow{r}, \widehat{\Omega}, E, t) = vN(\overrightarrow{r}, \widehat{\Omega}, E, t) \tag{4–3}$$

where v is the particle speed. The scalar flux can also be defined as a multiple of particle velocity v times the particle density N:

$$\Phi(\overrightarrow{r}, E, t) = \int_{4\pi} d\widehat{\Omega} vN(\overrightarrow{r}, \widehat{\Omega}, E, t) \tag{4–4}$$

Hence,

$$F_4 = \frac{1}{V}\int_V \int_t \int_E vN(\overrightarrow{r}, E, t)\, dE\, dt\, dV \tag{4–5}$$

Since $ds = vdt$,

$$F_4 = \frac{1}{V}\int_V \int_t \int_E N(\overrightarrow{r}, E, t)\, dE\, ds\, dV \tag{4–6}$$

The quantity $N(\overrightarrow{r}, E, t)$ is the track length density; therefore, the flux can be estimated by summing track lengths.

4.3 FM Card - Tally Multiplier

The FM card can modify any flux or current tally of the form $\int \varphi(E)\, dE$ into $\int R(E)\varphi(E)\, dE$, where R(E) is any combination of sums and products of energy-dependent quantities known to MCNP.

The FM card can also model attenuation. Here the tally is converted to:

$$\int \varphi(E)\, e^{-\sigma_t(E)\rho_a x}\, dE \tag{4–7}$$

, where x is the thickness of the attenuator, ρ_a is its atom density, and σ_t is its total cross section.

Two special FM card options are available. The first option sets R(E) $= 1/\varphi(E)$ to score tracks or collisions. The second option sets R(E) $= 1$ to score population or prompt removal lifetime.

Cross sections can be used as response functions with the FM card to determine reaction rates. MCNP5 thermal S(α,β) tables should be used if the neutrons are transported at sufficiently low energies that molecular binding effects are important.

4.4 FMESH4 Tally

Mesh tallies are invoked by using the FMESH card. As in the F card, a unique number is assigned to each mesh tally. Since only track-length mesh tallies are available, the mesh tally number must end with a 4, and may not be used to identify an F4 tally. The track length is computed over the mesh tally cells and normalized per starting particle, except in KCODE criticality calculations.

The FMESH card allows the user to define a mesh tally superimposed over the problem geometry. Results are written to a separate output file, with the default name MESHTAL. By default, the mesh tally calculates the track length estimate of the particle flux, averaged over a mesh cell, in units of particles/cm^2. If an asterisk precedes the FMESH card, energy time particle weight will be tallied, in units of MeV/cm^2.

The FMESH4 tally was used to compute the multi-group neutron flux distributions. Sets of 47 and 62 energy groups were analyzed for this tally. Three different energy ranges were studied depending on the neutron classification. The first class is thermal neutrons with a energy range of 0.1 eV $<$ E $<$ 1.0 eV, the second class is intermediate neutrons (1.0 eV $<$ E $<$ 1 MeV) and finally fast neutrons (E $>$ 1 MeV).

The following are keywords used with FMESH card that can be entered in any order,

- GEOM = mesh geometry: Cartesian or cylindrical
- AXS = direction vector of the cylindrical mesh axis
- VEC = direction vector, along with AXS that defines the plane for angle theta=0
- ORIGIN = x,y,z coordinates in MCNP cell geometry superimposed mesh origin
- IMESH = coarse mesh locations in x (rectangular) or r (cylindrical) direction
- IINTS = number of fine meshes within corresponding coarse meshes
- JMESH = coarse mesh locations in y (rectangular) or z (cylindrical) direction
- JINTS = number of fine meshes within corresponding coarse meshes
- KMESH = coarse mesh locations in z (rectangular) or theta (cylindrical) direction
- KINTS = number of fine meshes within corresponding coarse meshes
- EMESH = values of coarse meshes in energy
- EINTS = number of fine meshes within corresponding coarse energy meshes
- FACTOR = multiplicative factor for each mesh
- TR = transformation number to be applied to the tally mesh

4.5 Relative Error

For Monte Carlo calculations, the significance of understanding and calculating the variance and error in the calculated results cannot be overemphasized. MCNP reports the statistical error or uncertainty associated with every result.

The variance is inversely proportional to the square root the number of histories (N), such that relative error in the tally decreases with increasing N. The brute force of increasing N to improve precision rapidly reaches the point of diminishing returns. There are many variance reduction techniques that can be applied with MCNP5 to achieve precision within reasonable computational time.

Variance-reduction techniques in Monte Carlo calculations reduce the computer time required to obtain results of sufficient precision. Relative error R is defined as ratio of the variance $S_{\widehat{x}}$ to the mean estimate $\widehat{x}$ of the sample x_k,

$$R = \frac{S_{\widehat{x}}}{\widehat{x}} \tag{4–8}$$

The estimated variance of $S_{\widehat{x}}$ is given by

$$S_{\widehat{x}}^2 = \frac{S^2}{N} \tag{4–9}$$

with

$$S^2 = \frac{\sum_{i=1}^{N} \left(x_i - \widehat{x}\right)^2}{N-1} \approx \widehat{x^2} - \widehat{x}^2 (N \gg 0) \tag{4–10}$$

where the quantity S is the estimated standard deviation of the population of x based on the values of x_i that were actually sampled.

Let

$$\widehat{x^2} = \frac{1}{N} \sum_{i=1}^{N} x_i^2 \tag{4–11}$$

and

$$\widehat{x}^2 = \left(\frac{1}{N} \sum_{i=1}^{N} x_i \right)^2 \tag{4–12}$$

Combining Eqs. (3.10), (3.11), (3.12), and (3.13), R can be written (for N≫0) as

$$R = \sqrt{\frac{1}{N} \left(\frac{\widehat{x^2}}{\widehat{x}^2} - 1 \right)} = \sqrt{\frac{N^2}{N^2} \frac{\sum_{i=1}^{N} x_i^2}{\left(\sum_{i=1}^{N} x_i \right)^2} - \frac{1}{N}} \tag{4–13}$$

$$R = \sqrt{\frac{\sum_{i=1}^{N} x_i^2}{\left(\sum_{i=1}^{N} x_i \right)^2} - \frac{1}{N}} \tag{4–14}$$

Hence, if there are nonzero scores that are identical and equal to x, R becomes

$$R = \sqrt{\frac{nx^2}{(nx)^2}} = \frac{1}{\sqrt{n}}, N \gg n \tag{4–15}$$

To reduce the error in the tally results by z, z^2 times the original number of histories (n) must be calculated.

4.6 Variance Reduction Methods

4.6.1 Nonanalog Methods

The nonanalog Monte Carlo methods are a powerful tool used for many calculations, and traditionally they have been developed according to the need. A nonanalog Monte Carlo model attempts to follow “interesting”particles more often than “uninteresting”ones. An “interesting”particle is one that contributes a large amount to the quantity (or quantities) that needs to be estimated. Here, a combination of three variance reduction techniques are used to obtain better results in Monte Carlo calculations. These techniques are as follows: Geometry Splitting, Russian Roulette, Survival Biasing.

4.6.1.1 Geometry splitting (G.S.)

This technique is used when the ratio $\frac{w_i}{\pi(E_i)}$ is greater than an upper bound w_i=2.[5] It consists of replacing a particle of weight w_i by M_i particles of weight $\pi(E_i)$.[5] M_i is defined in the following way:

$$M_i = \begin{cases} Aint\frac{w_i}{\pi(E_i)}, & \text{with probability } (1-p) \\ Aint\frac{w_i}{\pi(E_i)} + 1, & \text{with probability } p \end{cases} \tag{4–16}$$

Where

$$p = \frac{w_i}{\pi(E_i)} - Aint\frac{w_i}{\pi(E_i)} \tag{4–17}$$

Aint(x) is the large integer such that Aint(x)$\leq$x.[5]

4.6.1.2 Russian roulette (R.R.)

This is a procedure in which a probability $p = \frac{w}{\pi(E)}$ is predetermined. The weight w of a particle at energy E can be replaced with an increased weight $w' = \pi(E)$ or with probability (1-p) the particle is terminated.[5]

4.6.1.3 Survival biasing (S.B.)

Survival biasing also known as *implicit absorption* or *implicit capture* allows more particles to have non-zero contribution to the score than the analog simulation (natural simulation). When particles collide in analog simulation, there is a probability that this particle to be absorbed by the nucleus and killed. However, in survival biasing (nonanalog simulation) the particle is never killed by absorption; instead, the particle (neutron) with weight W_n is reduced to w_n. Where

$$w_n = \left(1 - \frac{\sigma_a}{\sigma_t}\right) . W_n \tag{4–18}$$

- W_n - neutron weight.
- σ_a - microscopic absorption cross section.
- σ_t - total microscopic cross section.

MCNP5 implements survival biasing. By default setting this parameter to the neutron energy interval desired full advantage of this method will be achieved. Herein, the PHYS:N card from MCNP5 is set from 20 to 1e-14. If no survival biasing is needed just set the PHYS:N card to the maximum energy $\backsim$ 20Mev for both edges (PHYS:N 20 20).

4.6.2 Efficiency of the Nonanalog Method

The efficiency of a Monte Carlo simulation depends on the type of variance reduction applied to the problem in question. The MCNP5 code uses different cards to represent different types of variance reduction. However, only the PHYS and IMP commands were used. The command PHYS is used to avoid time-consuming tracking, physics, or unimportant tally contributions in the beam port. The command IMP is used to improve statistics.

4.6.2.1 PHYS card

The PHYS command is used to specify energy cutoffs and the physics treatments to be used for photons, neutrons and electrons.[11] The PHYS card is set as follows: PHYS:N 20 1E-14 where cross section table below 20 MeV is retained and for neutrons below 1E-14 MeV analog absorption (natural simulation) will be used, while above 1E-14 MeV survival biasing is used.

4.6.2.2 IMP card

The importance card (imp:n) specifies the relative cell importance for neutrons, one entry for each cell of the problem. The imp:n card can go in the data card section or it can be placed on the cell card line at the end of the list of surfaces. The imp:n card throughout out the beam port cells had a increase of a factor of two to keep neutron population roughly constant.

CHAPTER 5
MCNP5 SIMULATION RESULTS

5.1 Introduction

Using the Monte Carlo Neutron Transport Code (MCNP), neutron fission density distribution, multi-group neutron flux distribution, neutron energy flux, and neutron reaction rate were computed using a fixed source method with the sdef card. To compute neutron fission density distribution, the Watt fission spectrum was used. To compute the multi-group neutron flux distribution, FMESH4. The neutron tallies energy flux were found with *F4 tally cards . To calculate neutron reaction rate at certain locations of the radiation beam port using the gold foil (^{197}Au) as a target, the tally F4 with the tally multiplier FM4 was applied. The tally multiplier FM4 modifies the tally to achieve desired unit calculations. With the application of Monte Carlo variance reduction methods a relative error of less than 10% was obtained.

Application of nonanalog methods

The results, from Table 5-1, prove that the survival bias technique is a very useful tool in reducing computer time.

Table 5-1. MCNP5 - Total Transport Time (ctm) - 1CPU

nps	G.S. - R.R.	G.S. - R.R. - S.B.
5 million	111 min.	29 min.
10 million	195 min.	57 min.
50 million	768 min.	288 min.

However, when the two nonanalog simulations are compared the improvement of the relative error is not significant (Table 5-2); survival biasing has minimal impact in the statistics of the tally.

The figure of merit (FOM), in Table 5-3 is used to demonstrate the effectiveness of a Monte Carlo simulation when survival bias technique is applied. The FOM increases as computer time decreases such that a larger FOM means an effective Monte Carlo simulation.

Table 5-2. MCNP5 - Relative Error% for tally type F4

nps	Analog Simulation	Non-Analog (no S.B.)	Non-Analog (S.B.)
5 million	57.74%	55.53%	53.86%
10 million	50.21%	40.98%	38.86%
50 million	26.76%	19.38%	19.24%

G.S. = Geometry Splitting, R.R. = Russian Roullete, S.B. = Survival Biasing

Table 5-3. Figure of Merit (FOM)

nps	Variance Reduction	FOM $\times 10^{-3}$
5 million	G.S. - R.R.	1.8
5 million	G.S. - R.R. - S.B.	4.6
—	—	—
10 million	G.S. - R.R.	1.9
10 million	G.S. - R.R. - S.B.	7.2

G.S. = Geometry Splitting, R.R. = Russian Roullete, S.B. = Survival Biasing

5.2 UFTR Beam Port

5.2.1 UFTR Reactor South Beam Port Analyzes

In this section, the 47 energy-group cases will be analyzed for the south beam port. For the south beam port multi-group neutron flux distribution study, the neutron fission density distribution was calculated throughout the reactor core. However the fission neutron contribution was mainly from the fuel plates in fuel box 2 as shown in Figs 3-3, 3-4, 5-1 and 5-2.

5.2.2 Energy Groups Analyzed

The specifications in Table 5-4 are in accord with UFTR energy range measurements. Tables 5-7 show the group I.D.'s and cases that were studied for the radiation south beam port.

Table 5-4. Energy range for UFTR measurements

Energy	Energy Range		
Thermal	0.1 eV	-	1.0 eV
Epithermal	1.0 eV	-	1.0 MeV
Fast	1.0 MeV	-	17.332 MeV

Energy range for 47 energy groups

When geometry splitting (G.S.) and russian roullete (R.R.) variance reductions were combined with survival bias (S.B.), the simulation time was reduced significantly.

Table 5-5. General analyses for 47 energy groups for 16CPU's using (G.S. - R.R.)

Group I.D.♯	nps	Total CPU Time (min)	Relative Error%
45	2.2 billion	418,944	9.84
37	2.9 billion	558,746	9.83
17	2.9 billion	558,746	9.02

G.S. = Geometry Splitting, R.R. = Russian Roullete

Table 5-6. General analyses for 47 energy groups for 16CPU's using (G.S. - R.R. - S.B.)

Group I.D.♯	nps	Total CPU Time (min)	Relative Error%
45	2.2 billion	167,578	9.80
37	2.9 billion	223,498	9.80
17	2.9 billion	223,498	9.00

G.S. = Geometry Splitting, R.R. = Russian Roullete, S.B. = Survival Biasing

Table 5-7. Cases of study for 47 energy groups

Cases	Group I.D.♯	Energy Range		
Case 1	45	0.87640 eV	-	0.41400 eV
Case 2	37	1.5850e-03 MeV	-	4.5400e-04 MeV
Case 3	17	1.653 MeV	-	1.3530 MeV

5.2.3 South Beam Port 3-D Multi-Group Neutron Flux Distribution

The scattering and countour plots of the multi-group neutron flux distributions were calculated along the radiation south beam port before and along the collimator in two separate runs to show plot of the neutron flux intensity distribution with more details. It's noticed that there is a high intensity of neutron flux where the south beam port is closer to the fuel box 2 due to a high intensity of neutrons in this region as observed in the figures below.

5.2.4 Impact of Different Moderators in the UFTR

Herein, the neutron energy flux for 62 energy groups [Appendix **??**] will be studied with different moderators to check the effectiveness of particular moderators surrounding

the UFTR core. Two other moderators (light and heavy water) will be compared to graphite to analyze their impact on the neutron energy flux in the south beam port region close to the fuel box 2 (Fig. 3-3).

- Graphite - Graphite (carbon) could be used as a reflector as well. Nuclear graphite is specifically produced for use as a moderator or reflector inside of a nuclear reactor.
- Light Water (H_2O) - In natural water, almost all of the hydrogen atoms are protium, ^1H. Light water is largely used in nuclear reactors because it is extremely inexpensive.
- Heavy Water (D_2O coolant) - *Heavy water* is chemically the same as regular (light) water, but with the two hydrogen atoms (as in H_2O) replaced with deuterium (^2H) atoms (hence the symbol D_2O, deuterium oxide). The presence of the neutrons in the deuterium atoms of heavy water is what makes it ”heavy”, about 11% denser than water.

Power-generating reactors use light water coolant as moderator. However, heavy water is better than light water at moderating (slowing) neutrons for several reasons, which make it useful in some nuclear reactor cores. Tables 5-8 and 5-9 show physical properties and parameters of the moderators in study.

Table 5-8. Physical properties of heavy water (D_2O) and light water (H_2O)

Property	D_2O	H_2O
Freezing point (°C)	3.82	0.00
Boiling point (°C)	101.4	100.0
Density (at 20°C, g/cm^3, liquid)	1.1056	0.9982
Temp. of maximum density (°C)	11.6	4.0

Table 5-9. Slowing Down Parameters of Typical Moderators

Moderator	A	α	ξ	ρ[g/cm^3]	$\xi\Sigma_s$[cm^{-1}]	$\xi\Sigma_s/\Sigma_a$
H_2O	-	-	0.920	0.9982	1.35	71
D_2O	-	-	0.509	1.1056	0.176	5670
C	12	0.716	0.158	1.6	0.060	192

The parameters in Table 5-9 are useful to identify which moderator is more efficient to slow down neutrons coming from the reactor core. The mathematical equations of these quantities are presented as follows:

- $\alpha = (\frac{A-1}{A+1})^2$, where A is the nuclear mass
- ξ is the mean lethargy gain per collision average number of collisions necessary to slow down a fission neutron from 2 MeV to 1.0 eV is found by

$$< \sharp >= \frac{\ln \frac{2\times 10^6}{1.0}}{\xi} = \frac{14.5}{\xi} \tag{5–1}$$

  where the mean lethargy gain per collision is given by

$$\xi \equiv < \Delta u >= \int_{\alpha E_i}^{E_i} [\ln\left(\frac{E_0}{E_f}\right) - \ln\left(\frac{E_0}{E_i}\right)] \frac{1}{1-\alpha}\, dE_f \tag{5–2}$$

  or

$$\xi = 1 + \frac{\alpha}{1-\alpha} \ln \alpha = 1 - \frac{(A-1)^2}{2A} \ln \frac{A+1}{A-1} \tag{5–3}$$

- $\xi\Sigma_s$ is the moderating power of a material. However, this parameter is not enough to describe the effectiveness of a material for neutron moderation because the moderator has to be a weak absorber of neutrons as well.
- $\frac{\xi\Sigma_s}{\Sigma_a}$ is the moderating ratio.

The best moderator (D_2O) is heavy water because it has the biggest moderating ratio.

Neutron Spectra in the Moderator

In this section the neutron spectra will be analyzed for different moderators. By changing the graphite (moderator) that surrounds the UFTR reactor core to other types of moderators, changes in the neutron spectra are observed. This can be observed in the Figures 5-39 and 5-41.

As shown in Figure 5-39 the thermal neutron energy flux is more intense in light water (H_2O) than heavy water (D_2O) and Graphite (C). This happens due to the neutron cross section of an isotope (Figs. 5-43, 5-44, 5-45, and 5-46).

In general, the values of absorption cross-section for light water are higher than for heavy water (Fig. 5-44). This is why light water coolant has a lower moderating ratio than heavy water. However, the scattering cross section for hydrogen is approximately over 10 times that of deuterium, mostly due to the large incoherent scattering length of hydrogen (Fig. 5-43). This is the reason why the thermal neutron flux for light water is more intense than that of heavy water.

When fast neutron energy flux is also considered graphite performed better than light water and heavy water due to the resonance of the neutron scattering cross section of graphite (C) for high energy groups (Fig. 5-43).

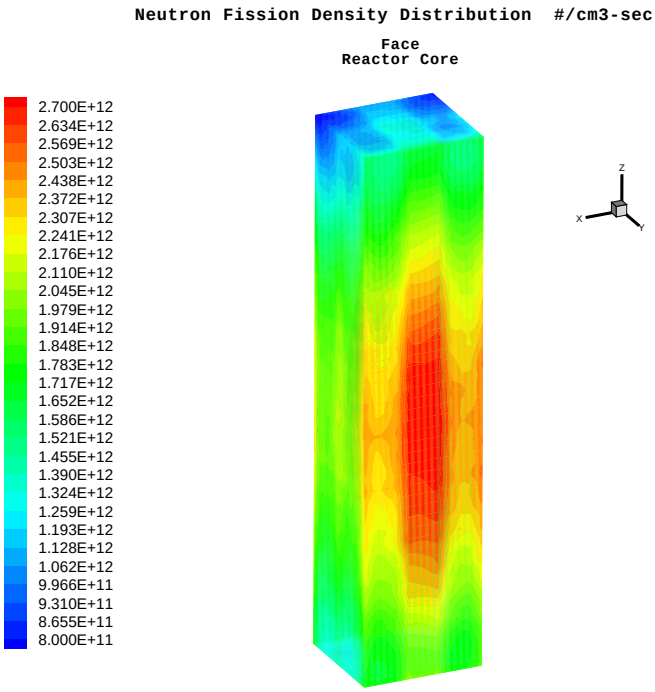

Figure 5-1. Neutron fission density distribution $\sharp/cm^3$-sec throughout the fuel box 2 facing the reactor core.

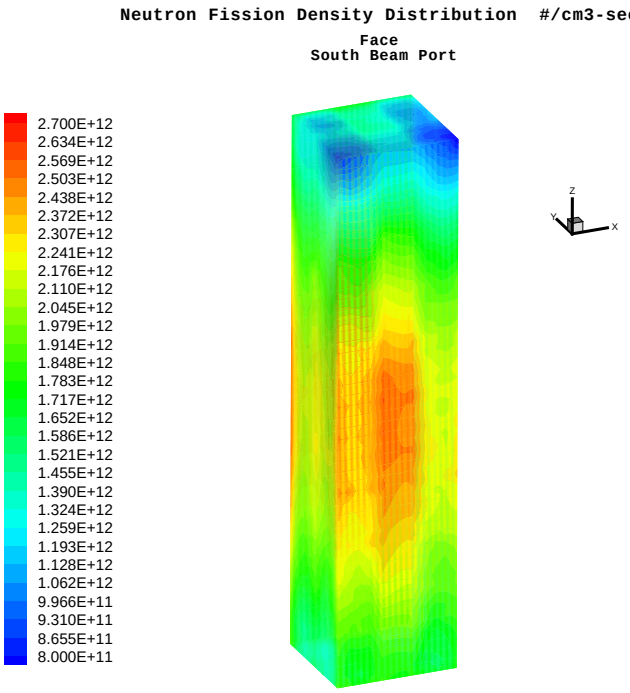

Figure 5-2. Neutron fission density distribution $\sharp/cm^3$-sec throughout the fuel box 2 facing south beam port.

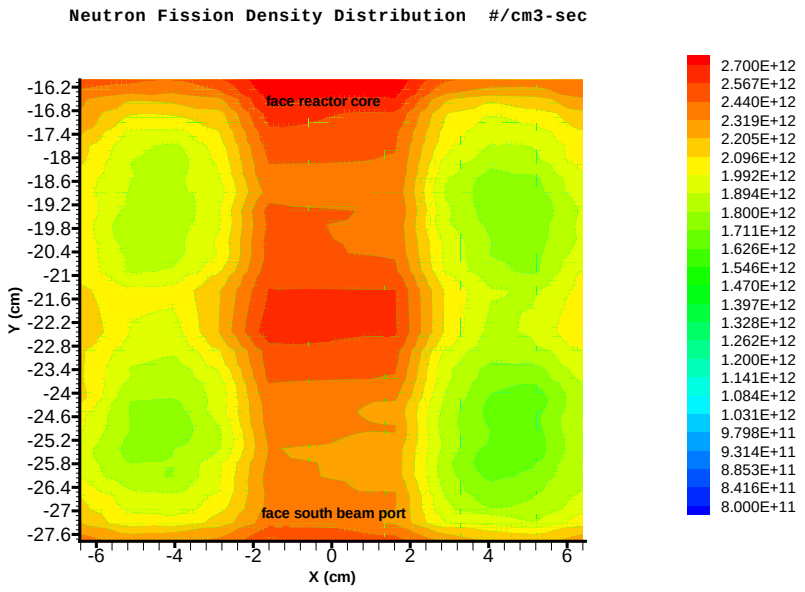

Figure 5-3. xy cross-section at z=-1 mid-section of the fuel box 2

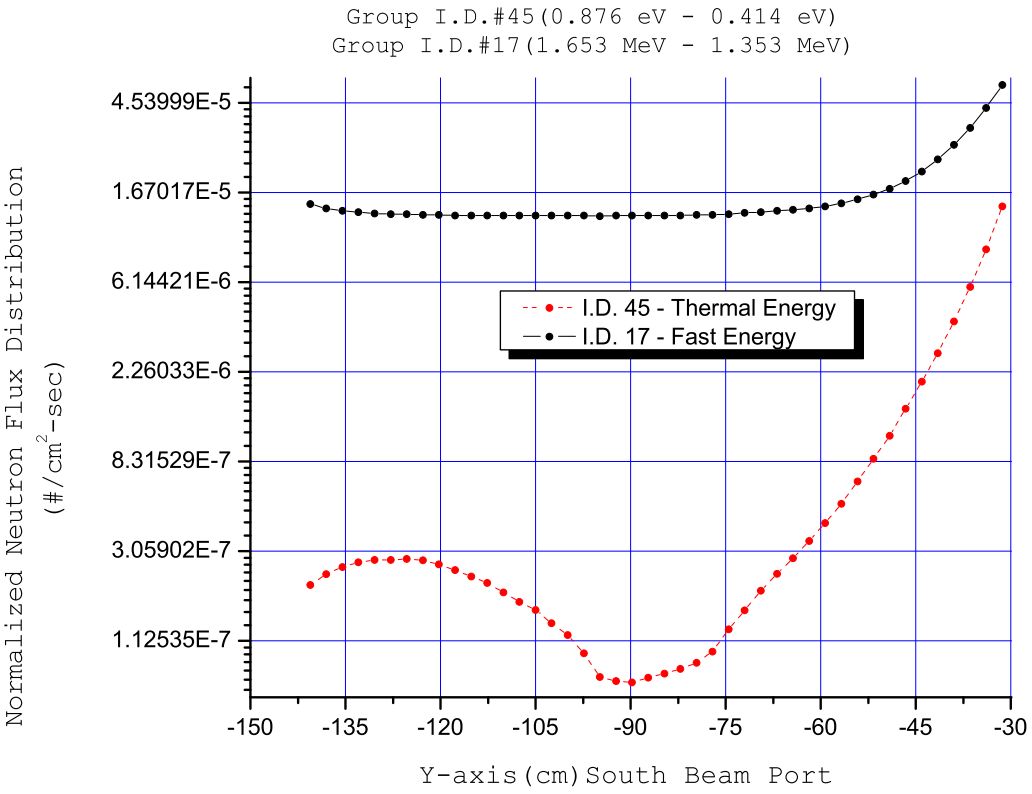

Figure 5-4. 2-D Neutron Flux Distribution for 47 energy groups along Y-axis (cm) before Collimator region.

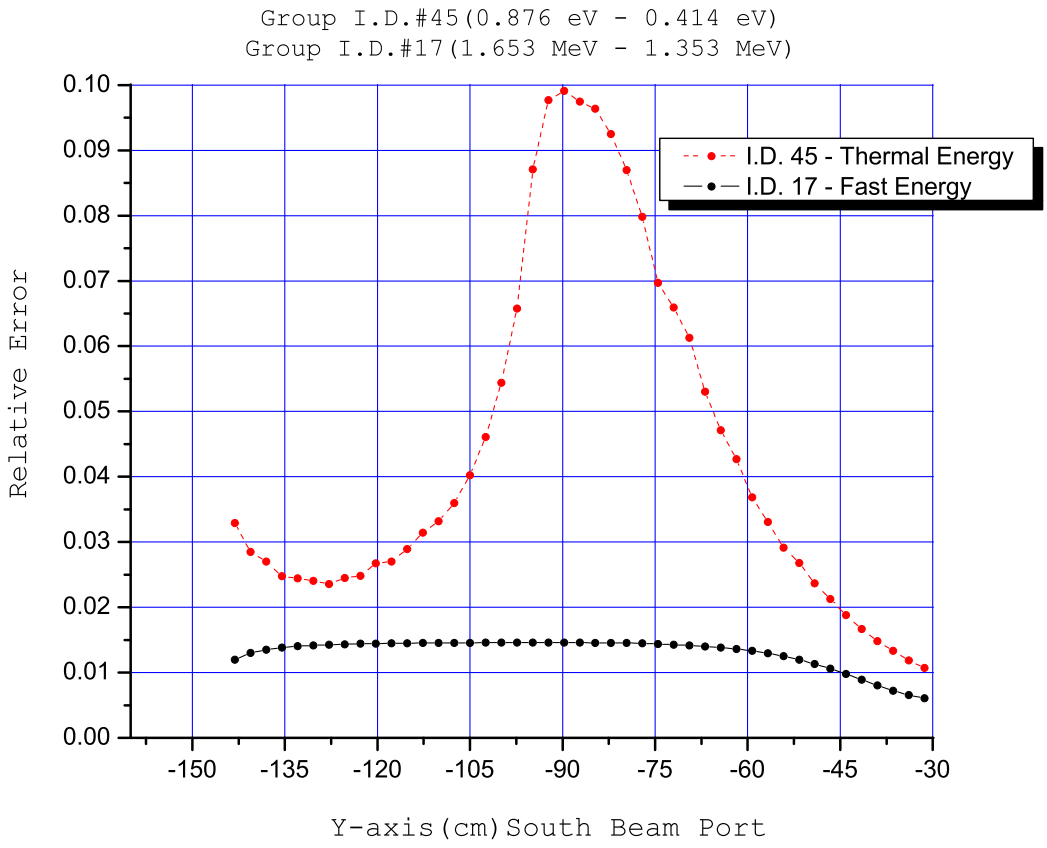

Figure 5-5. 2-D Neutron Flux Distribution Relative Error for 47 energy groups along the Y-axis(cm) before Collimator region.

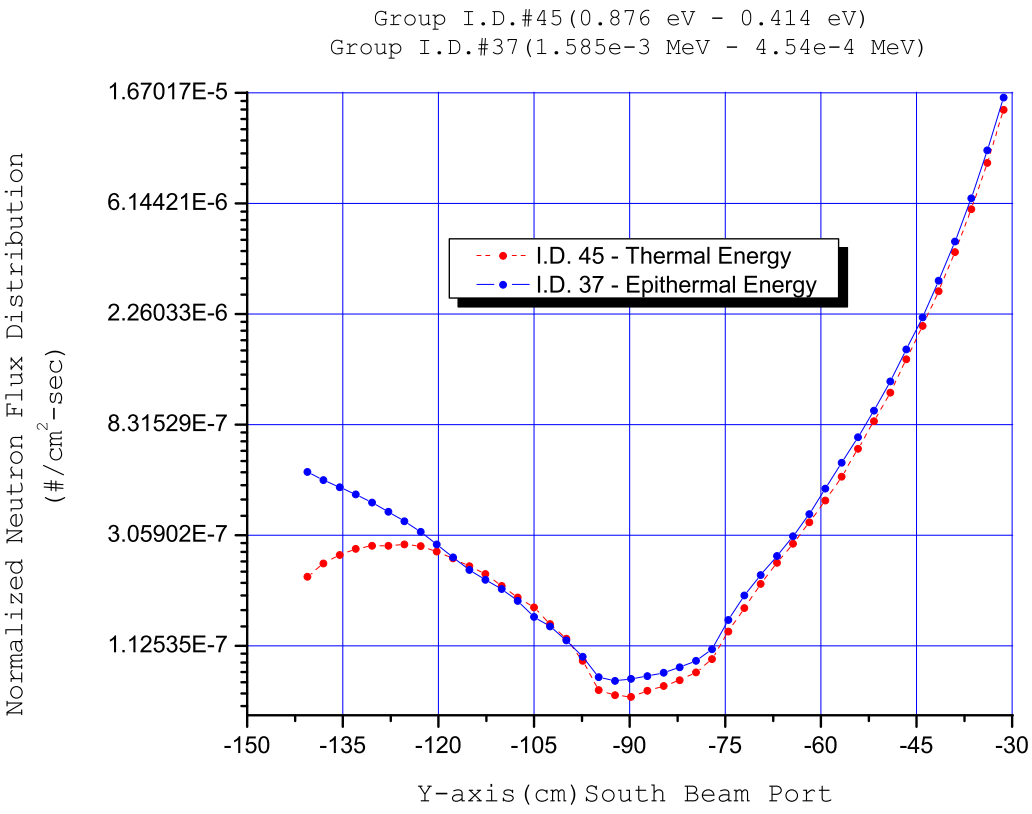

Figure 5-6. 2-D Neutron Flux Distribution for 47 energy groups along Y-axis (cm) before Collimator region.

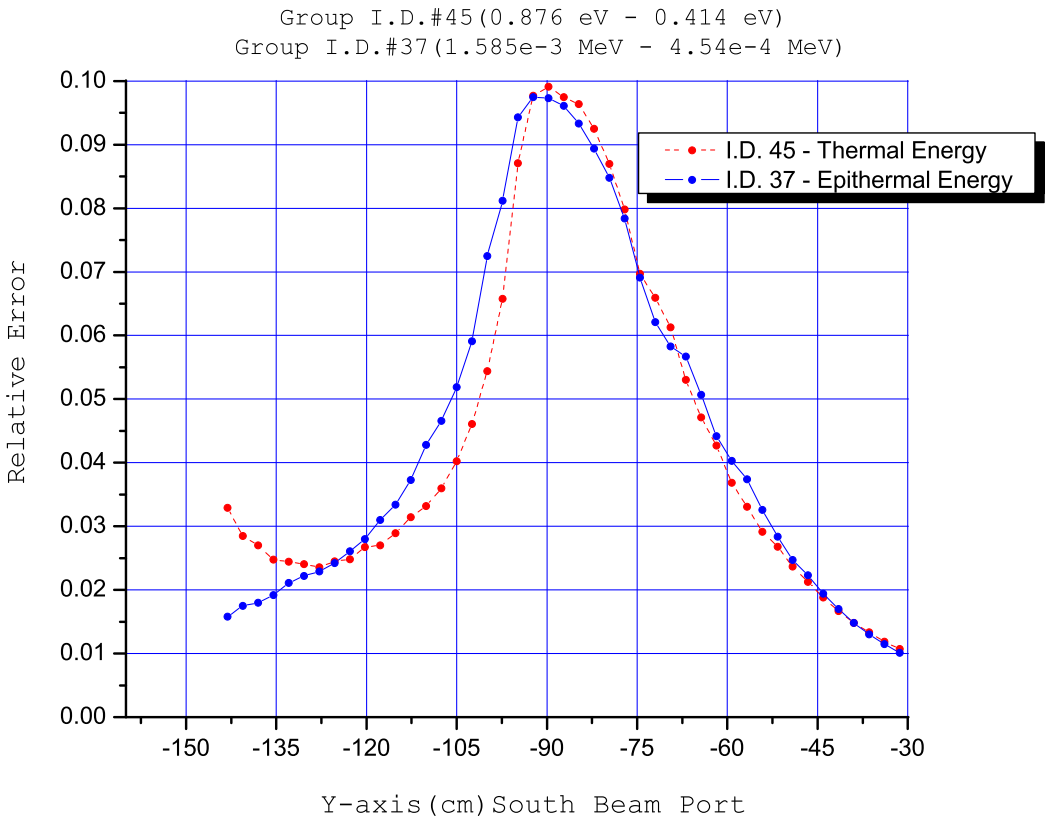

Figure 5-7. 2-D Neutron Flux Distribution Relative Error for 47 energy groups along the Y-axis(cm) before Collimator region.

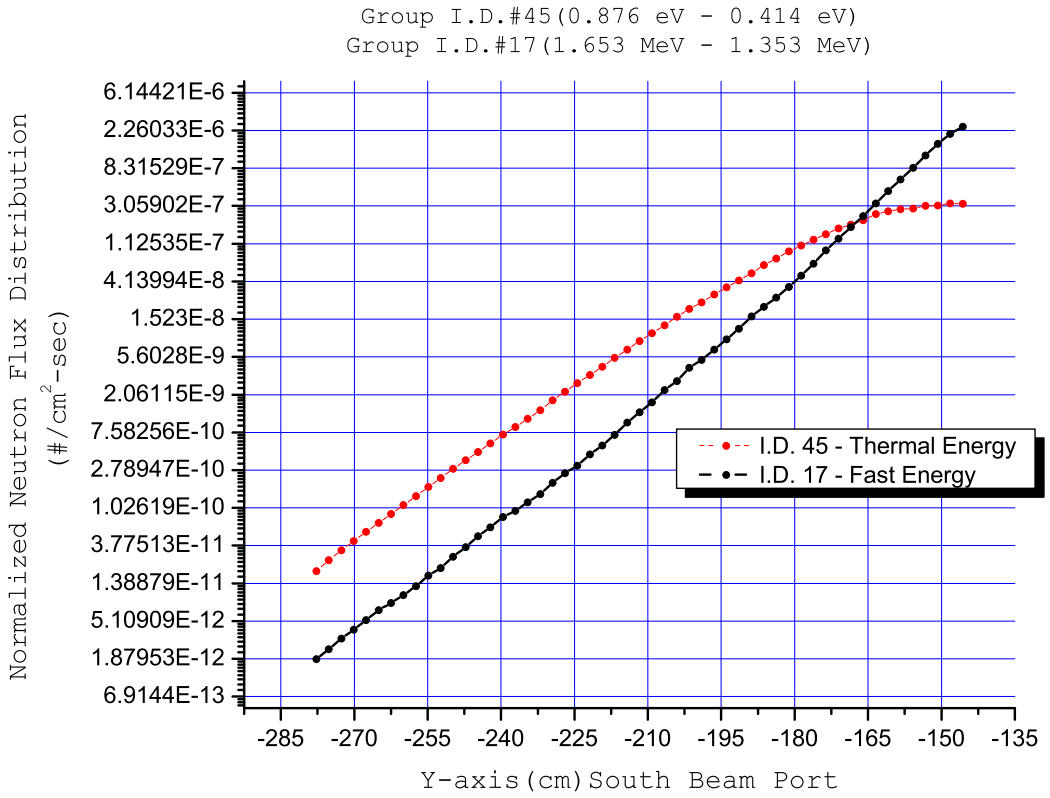

Figure 5-8. 2-D Neutron Flux Distribution for 47 energy groups along Y-axis (cm) in the Collimator region.

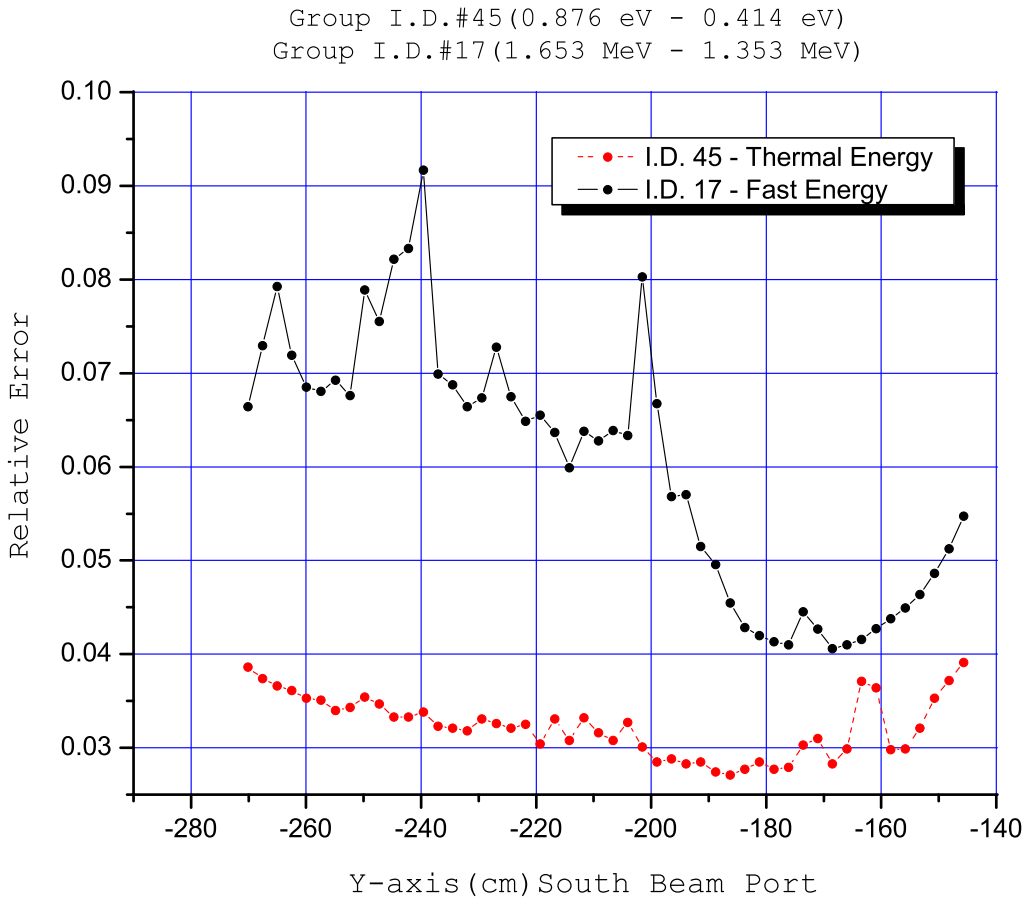

Figure 5-9. 2-D Neutron Flux Distribution Relative Error for 47 energy groups along the Y-axis(cm) in the Collimator region.

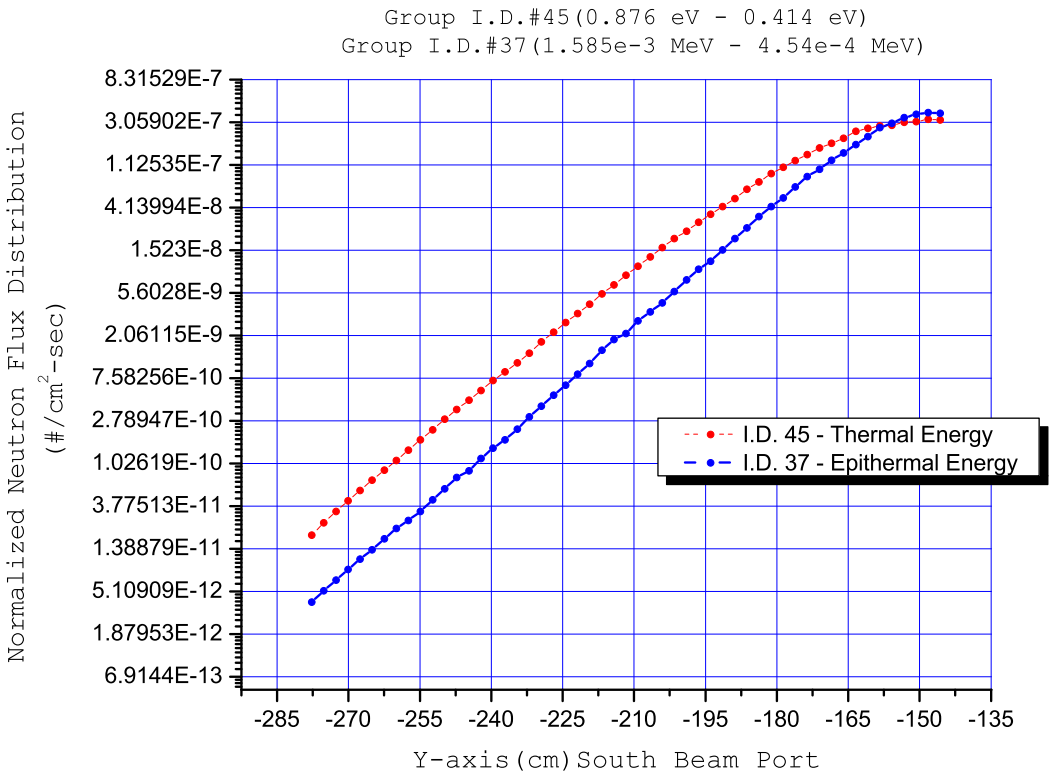

Figure 5-10. 2-D Neutron Flux Distribution for 47 energy groups along Y-axis (cm) in the Collimator region.

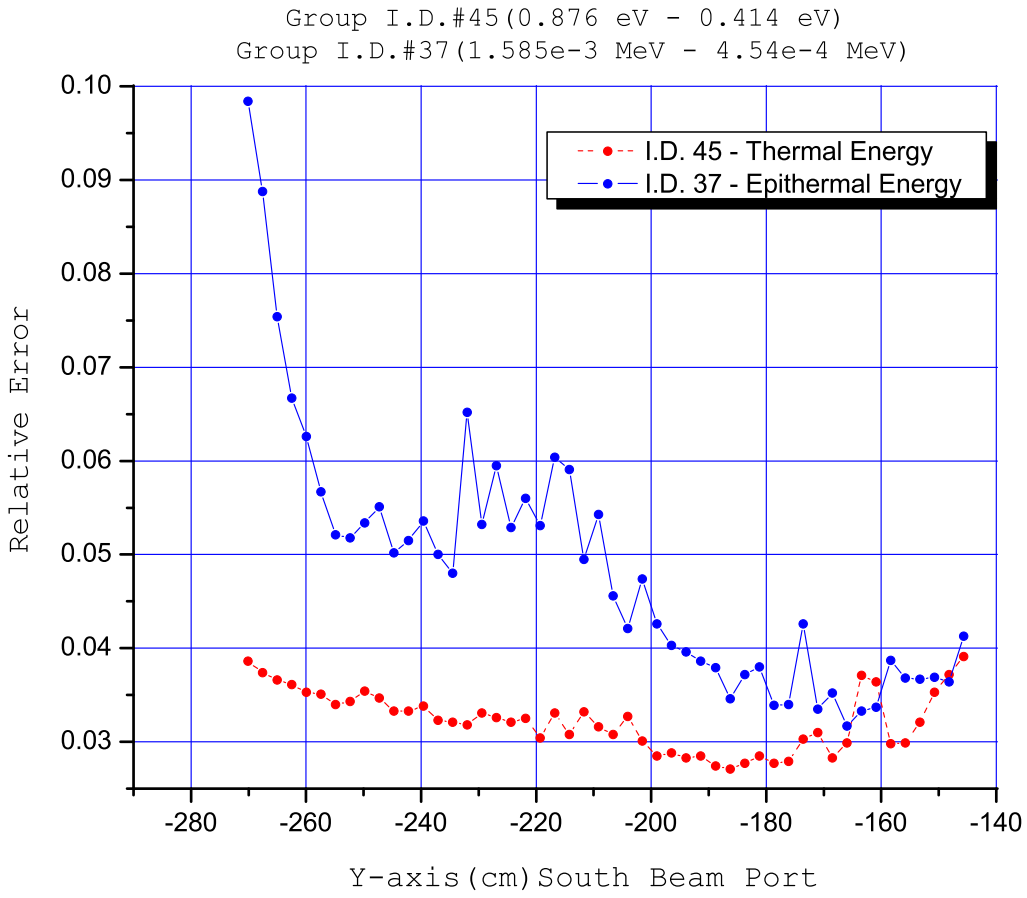

Figure 5-11. 2-D Neutron Flux Distribution Relative Error for 47 energy groups along the Y-axis(cm) in the Collimator region.

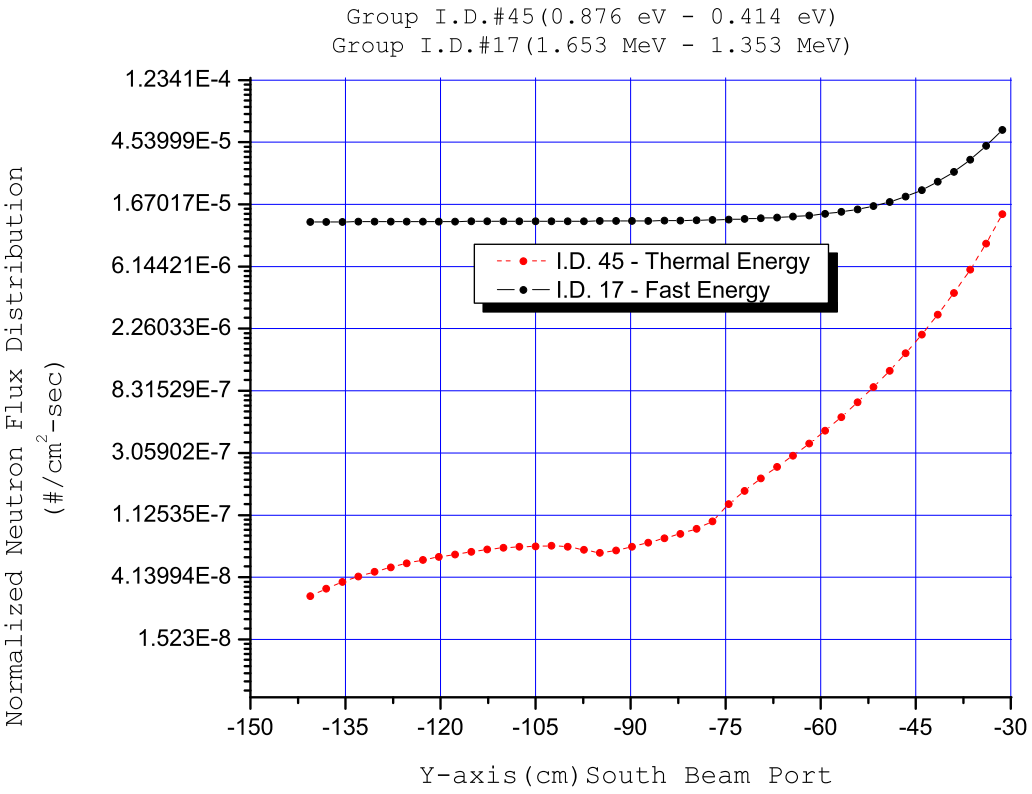

Figure 5-12. 2-D Neutron Flux Distribution Without Collimator for 47 energy groups along the Y-axis(cm) Before Collimator region.

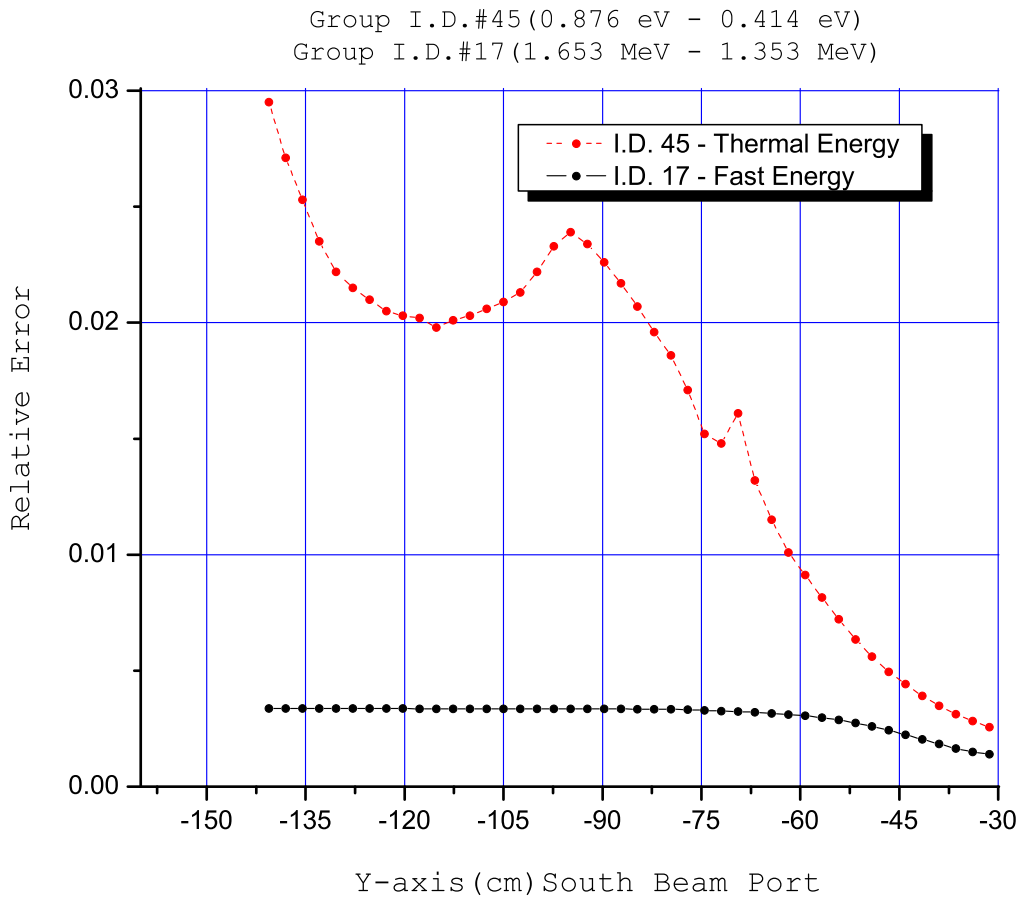

Figure 5-13. 2-D Neutron Flux Distribution Relative Error for 47 energy groups Without Collimator along the Y-axis(cm) Before Collimator region.

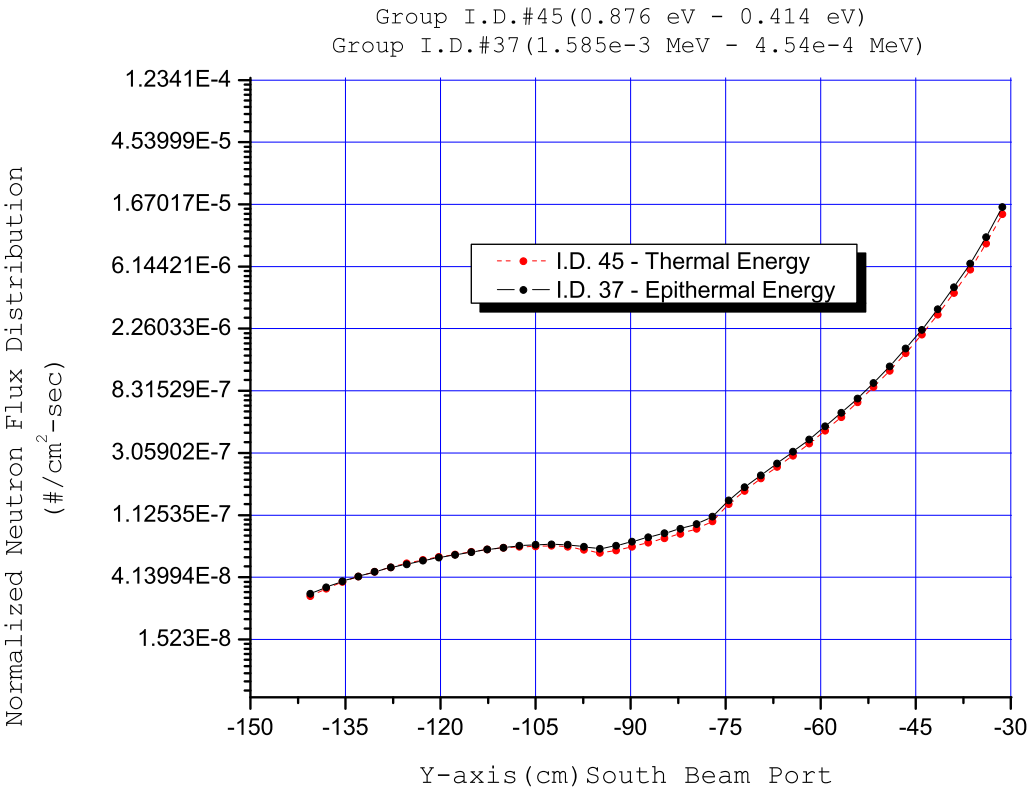

Figure 5-14. 2-D Neutron Flux Distribution Without Collimator for 47 energy groups along the Y-axis(cm) Before Collimator region.

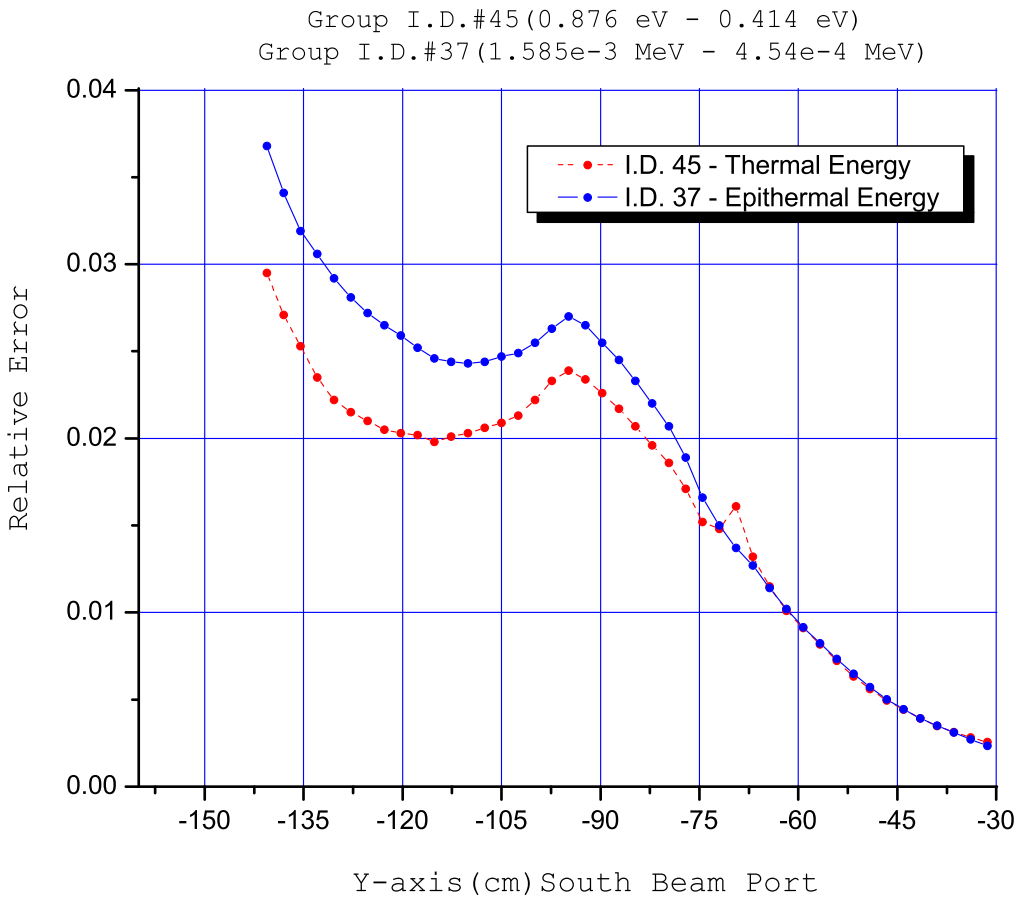

Figure 5-15. 2-D Neutron Flux Distribution Relative Error for 47 energy groups Without Collimator along the Y-axis(cm) Before Collimator region.

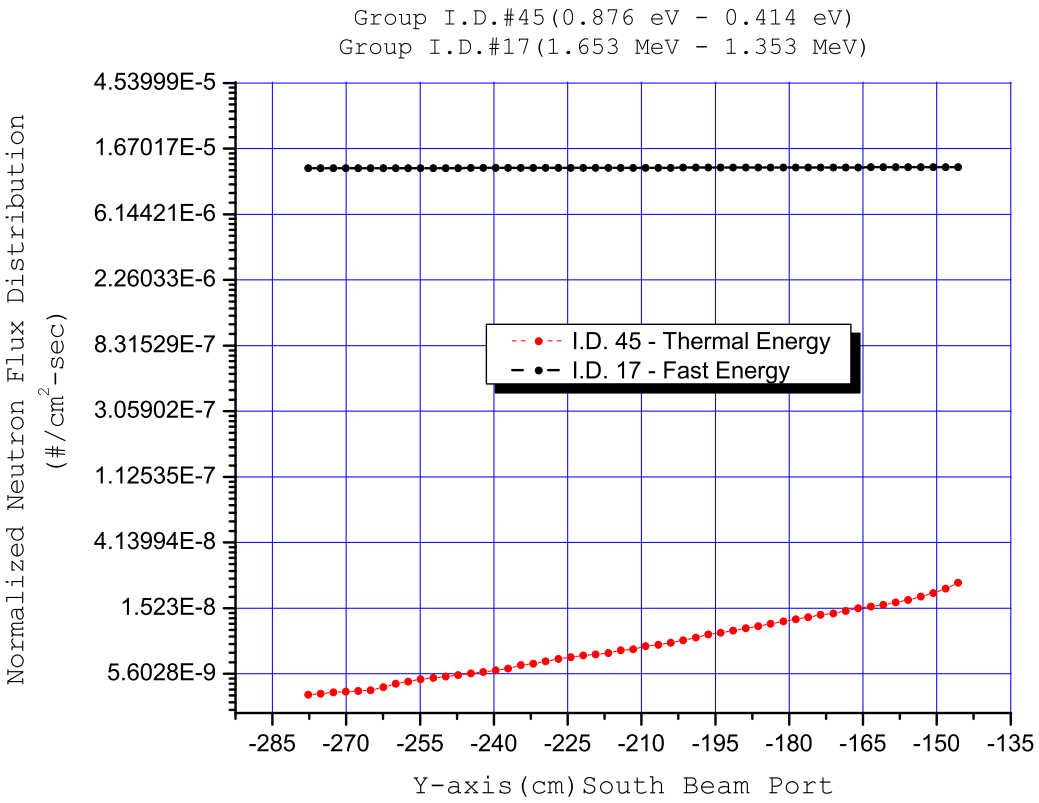

Figure 5-16. 2-D Neutron Flux Distribution Without Collimator for 47 energy groups along the Y-axis(cm) in the Collimator region.

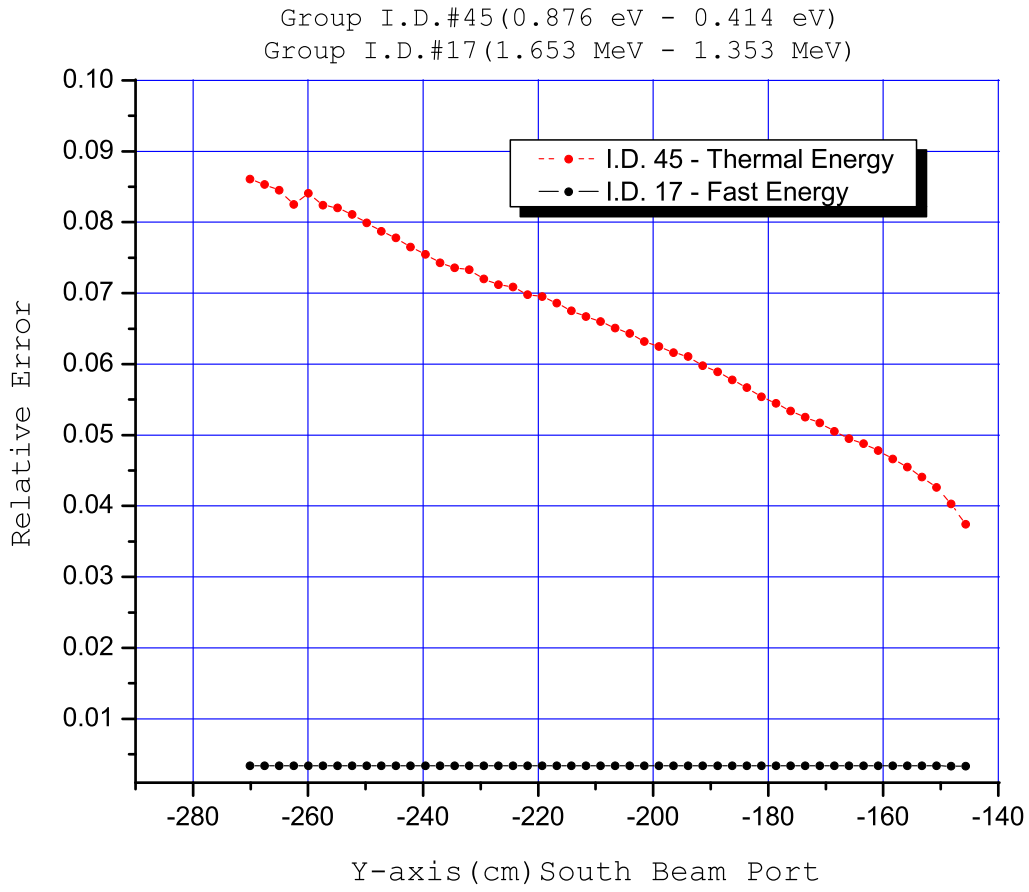

Figure 5-17. 2-D Neutron Flux Distribution Relative Error for 47 energy groups Without Collimator along the Y-axis(cm) in the Collimator region.

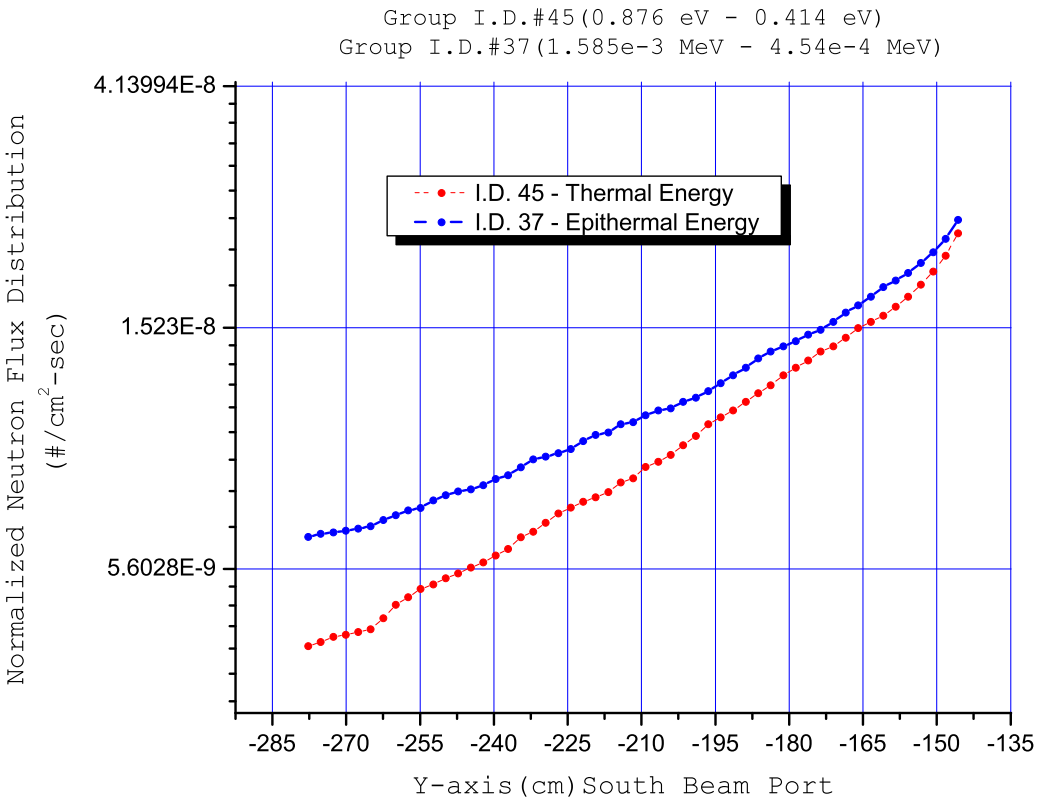

Figure 5-18. 2-D Neutron Flux Distribution Without Collimator for 47 energy groups along the Y-axis(cm) in the Collimator region.

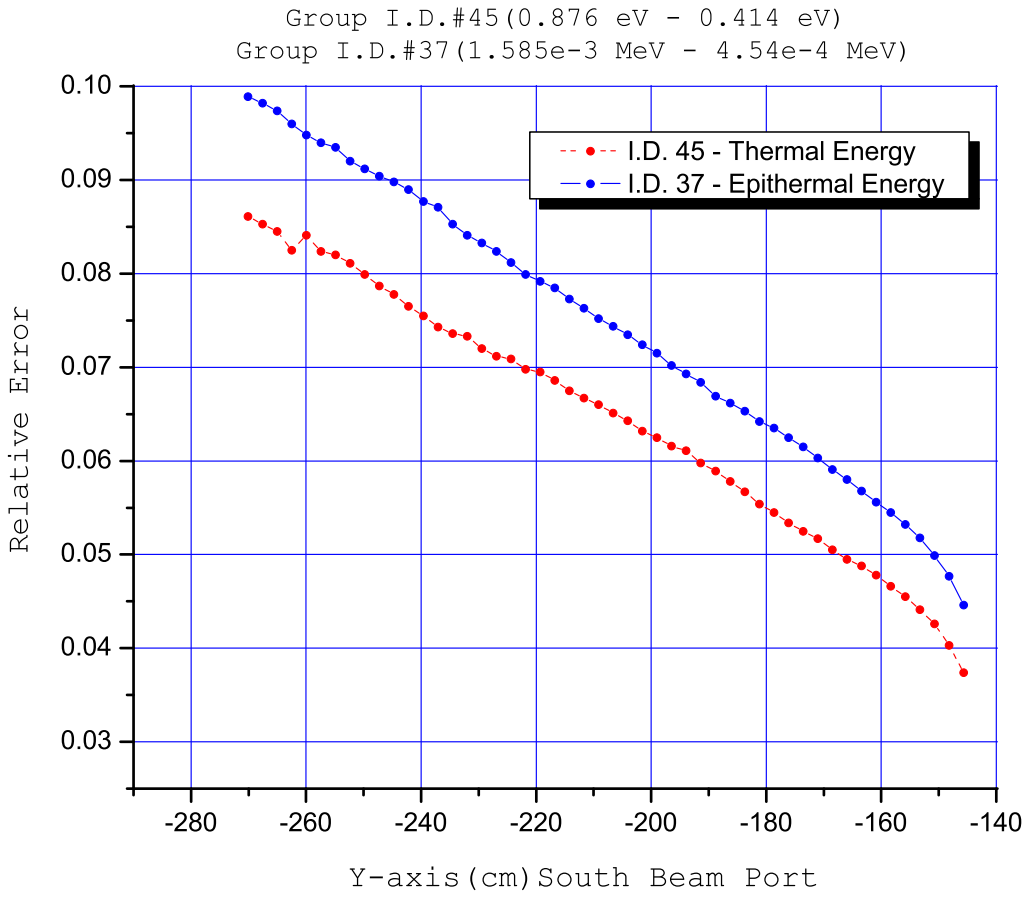

Figure 5-19. 2-D Neutron Flux Distribution Relative Error for 47 energy groups Without Collimator along the Y-axis(cm) in the Collimator region.

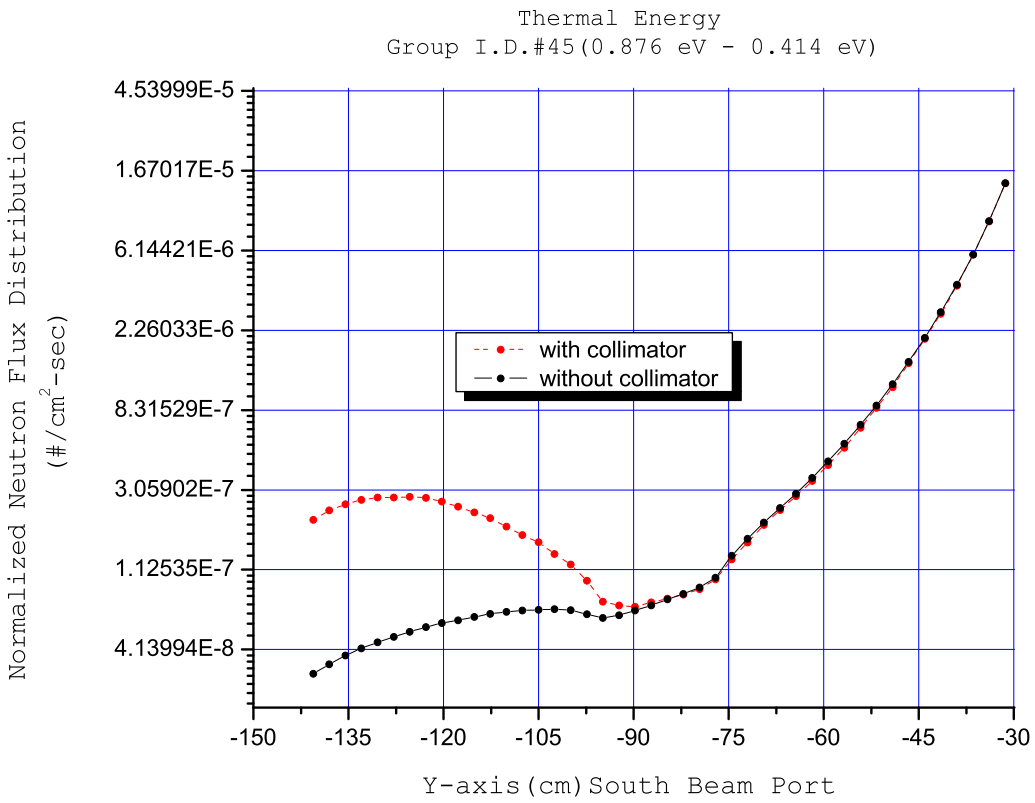

Figure 5-20. 2-D Neutron Flux Distribution With and Without Collimator for 47 energy groups along the Y-axis(cm) Before Collimator region.

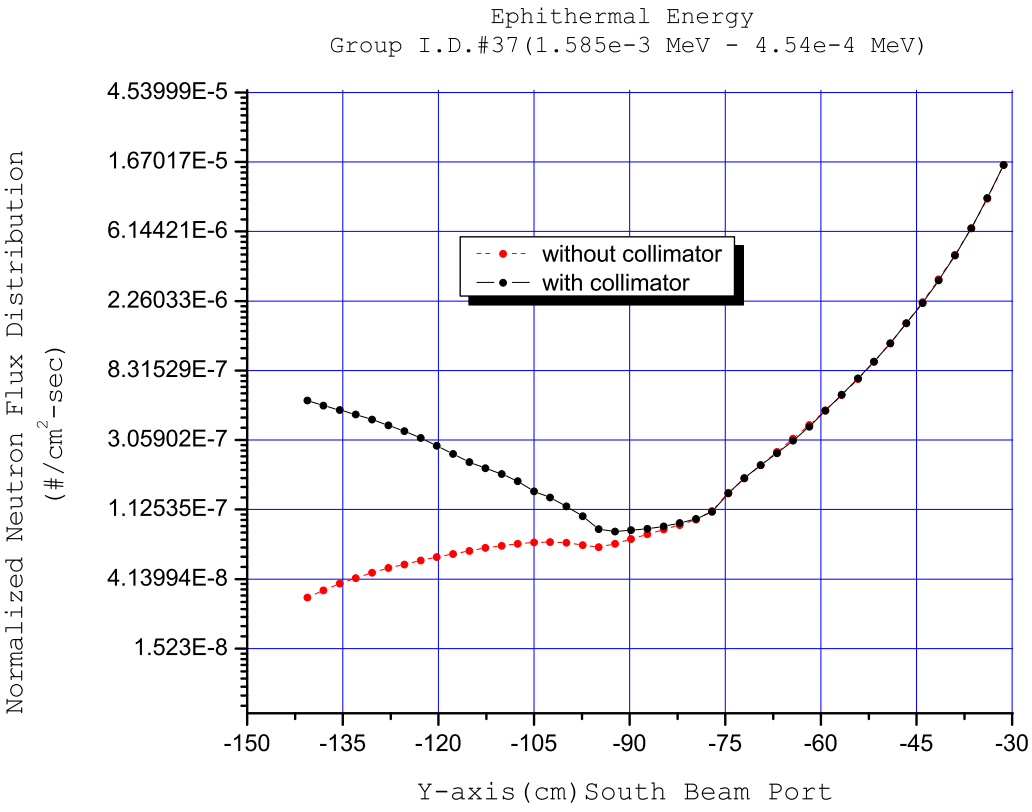

Figure 5-21. 2-D Neutron Flux Distribution With and Without Collimator for 47 energy groups along the Y-axis(cm) Before Collimator region.

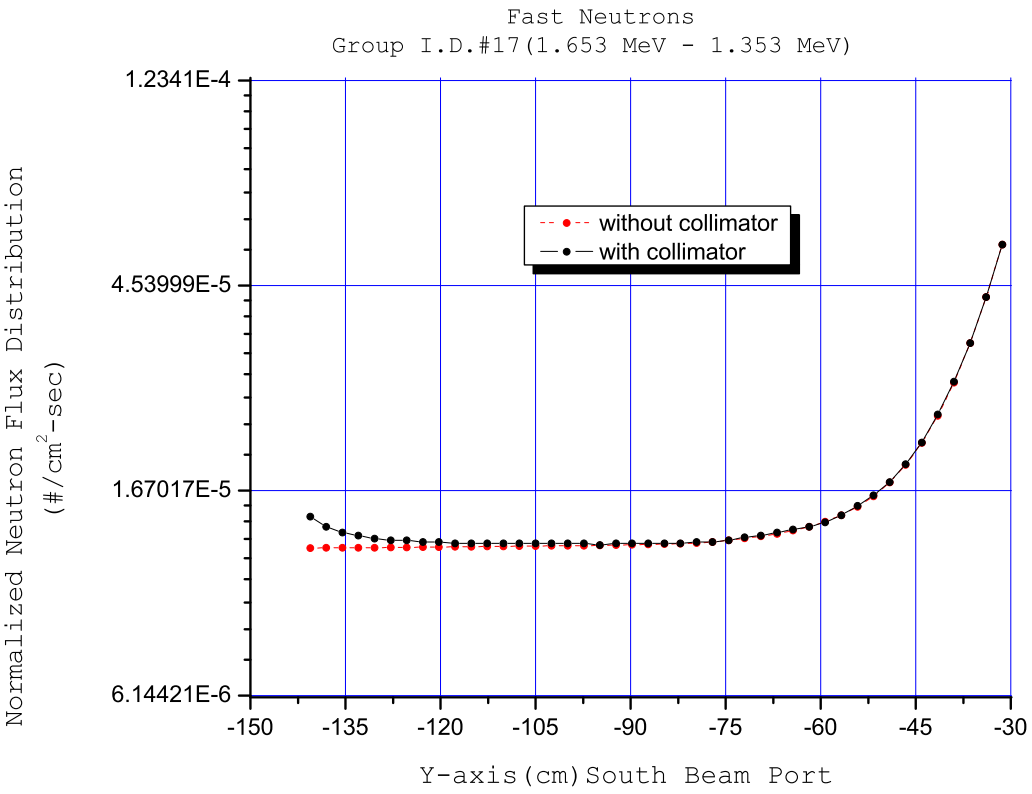

Figure 5-22. 2-D Neutron Flux Distribution With and Without Collimator for 47 energy groups along the Y-axis(cm) Before Collimator region.

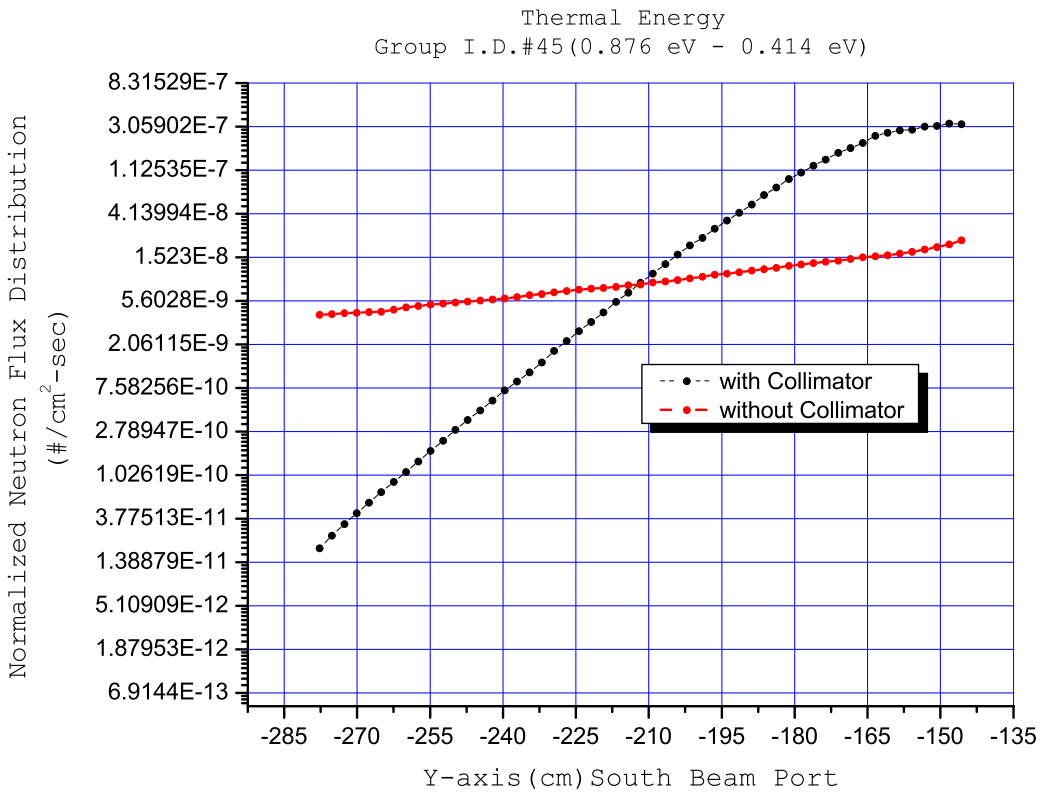

Figure 5-23. 2-D Neutron Flux Distribution With and Without Collimator for 47 energy groups along the Y-axis(cm) in the Collimator region.

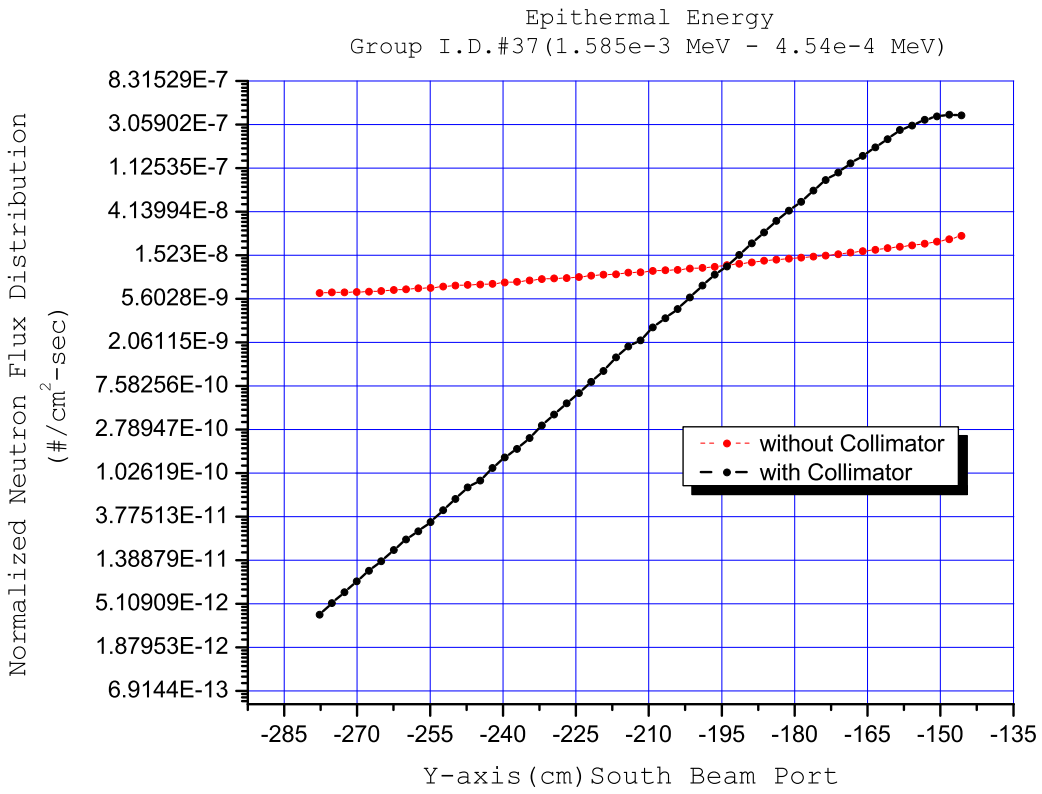

Figure 5-24. 2-D Neutron Flux Distribution With and Without Collimator for 47 energy groups along the Y-axis(cm) in the Collimator region.

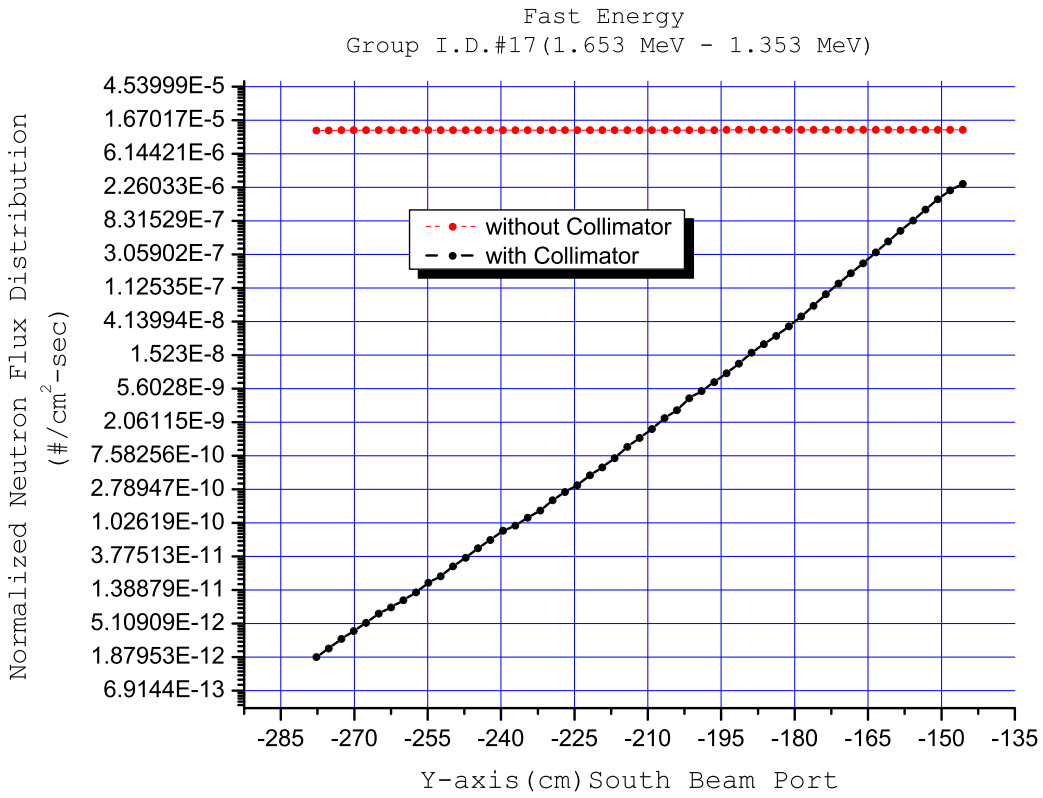

Figure 5-25. 2-D Neutron Flux Distribution With and Without Collimator for 47 energy groups along the Y-axis(cm) in the Collimator region.

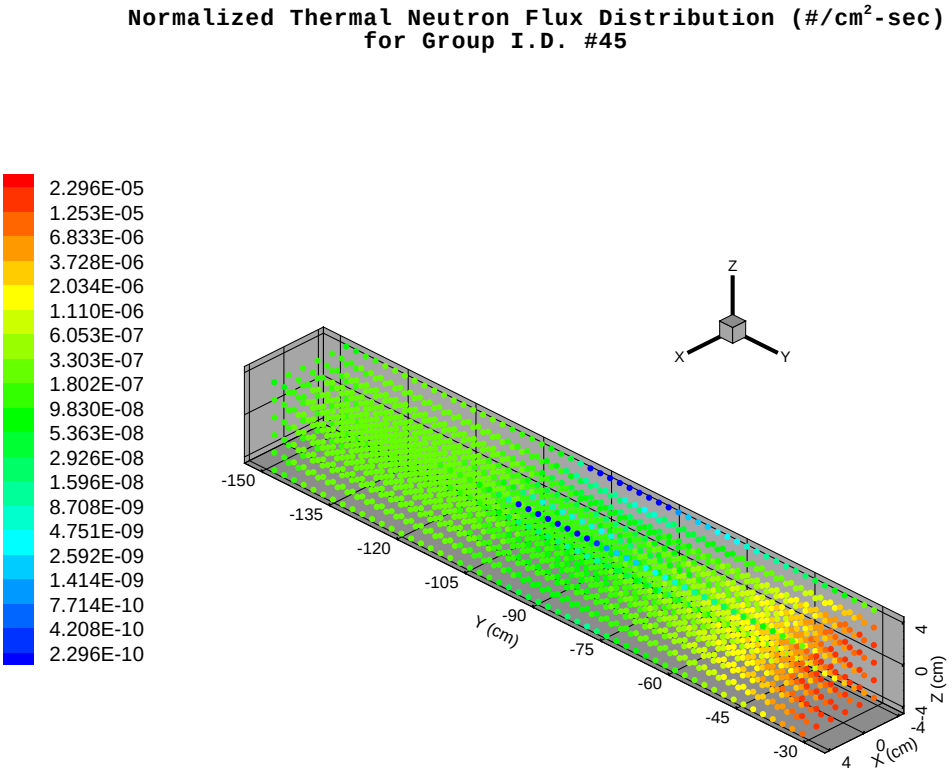

Figure 5-26. 3-D thermal neutron flux distribution along the Y-axis(cm) south beam port before collimator region.

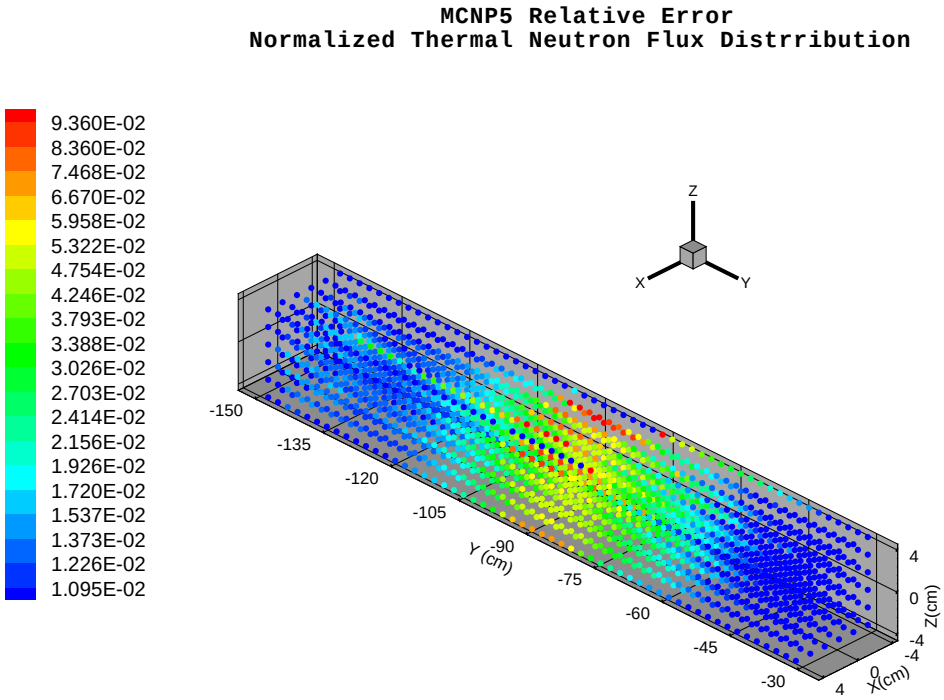

Figure 5-27. 3-D thermal neutron flux relative error along the Y-axis(cm) south beam port before collimator region.

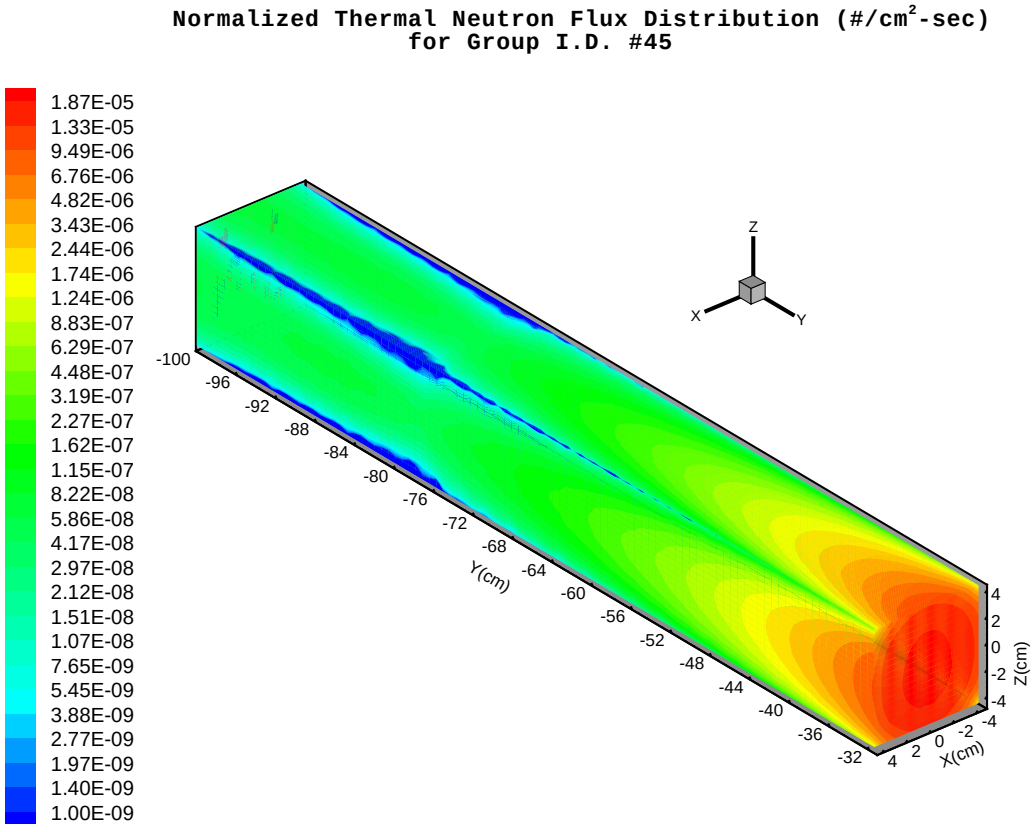

Figure 5-28. Contour 3-D thermal neutron flux distribution along the Y-axis(cm) south beam port before collimator region.

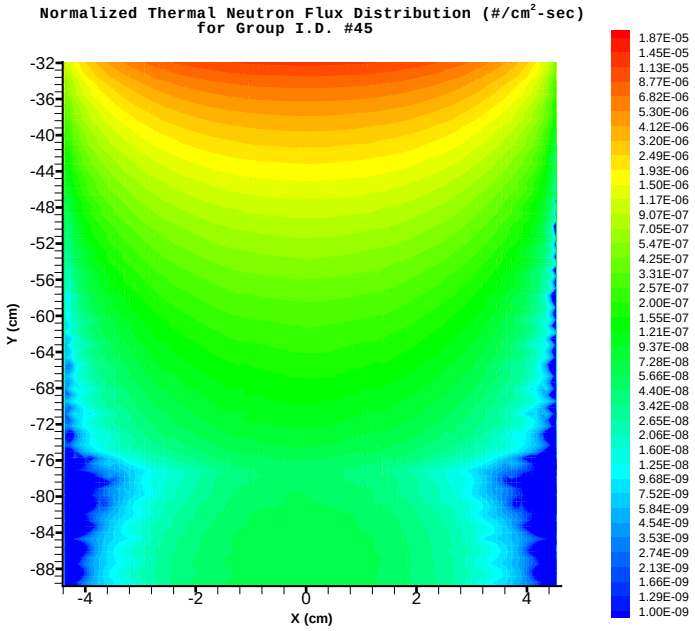

Figure 5-29. xy south beam port cross section .

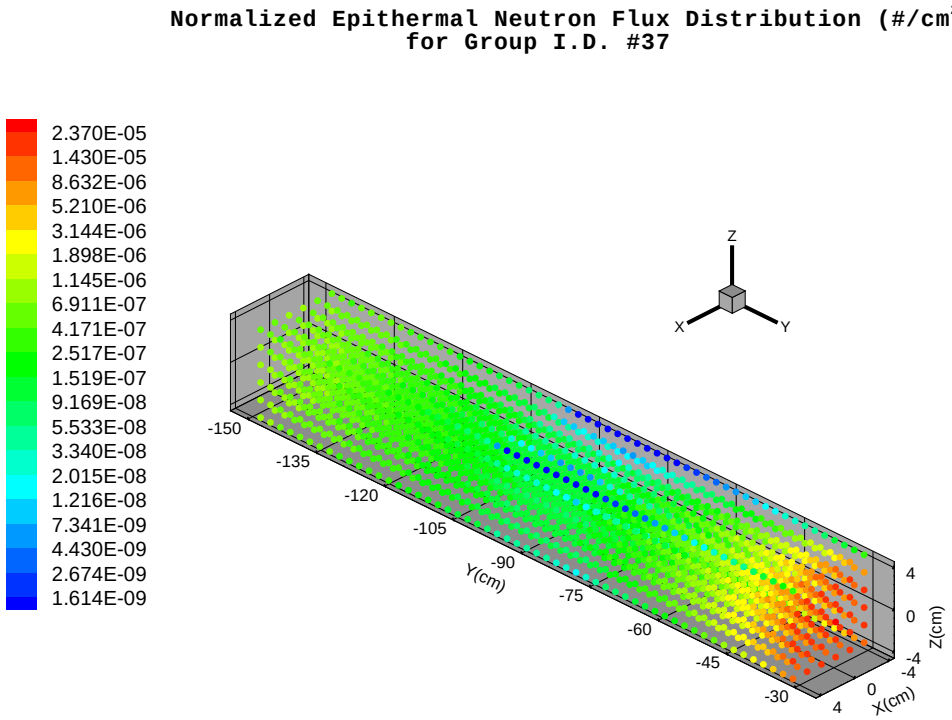

Figure 5-30. 3-D epithermal neutron flux distribution along the Y-axis(cm) south beam port before collimator region.

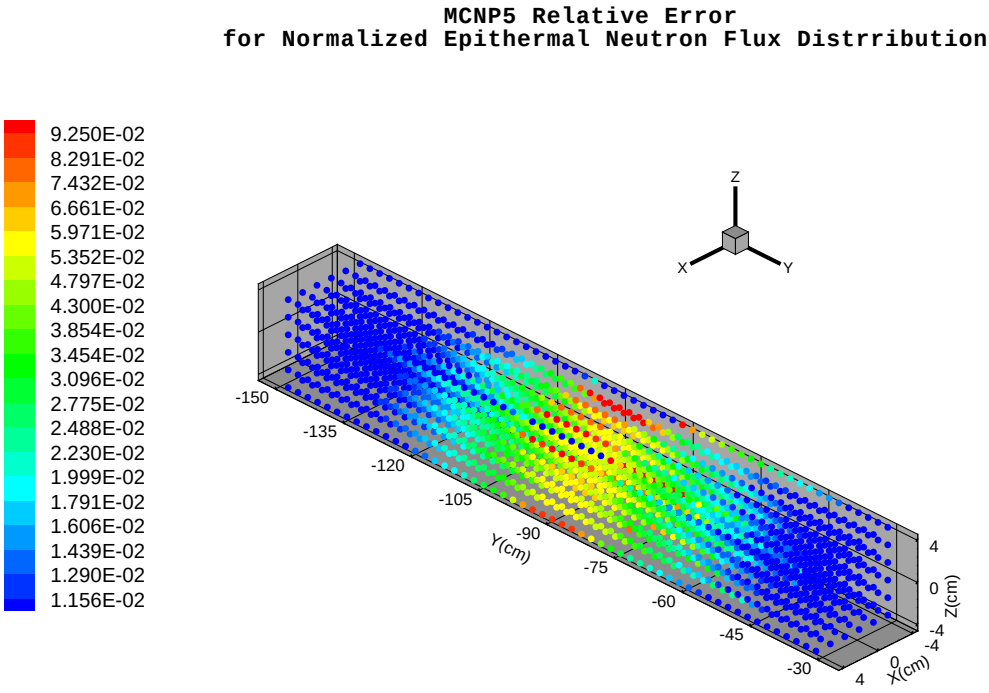

Figure 5-31. 3-D epithermal neutron flux distribution relative error along the Y-axis(cm) south beam port before collimator region.

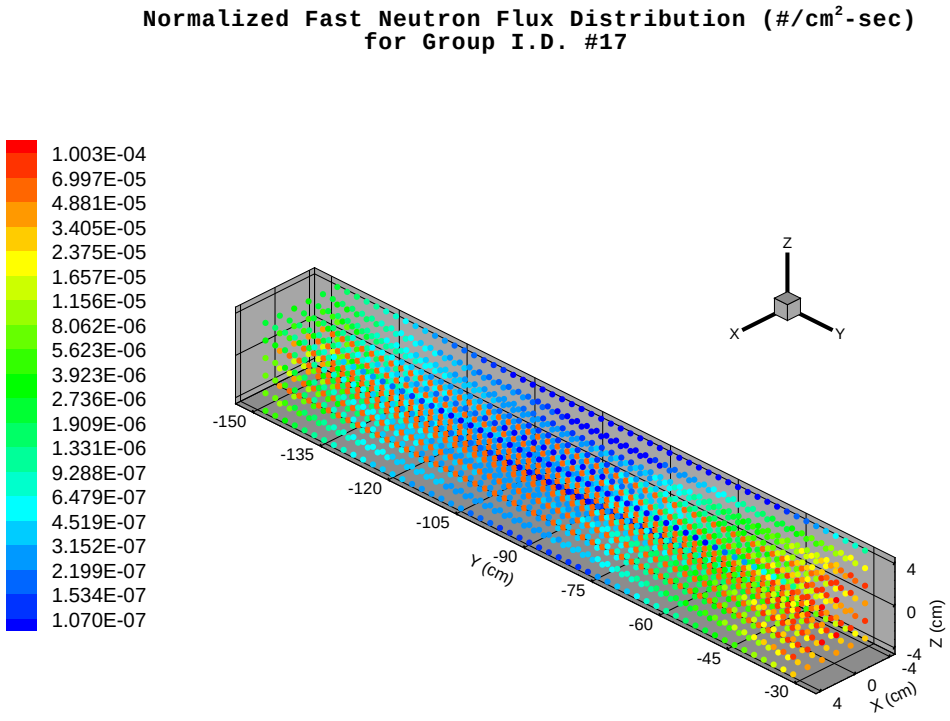

Figure 5-32. 3-D fast neutron flux distribution along the Y-axis(cm) south beam port before collimator region.

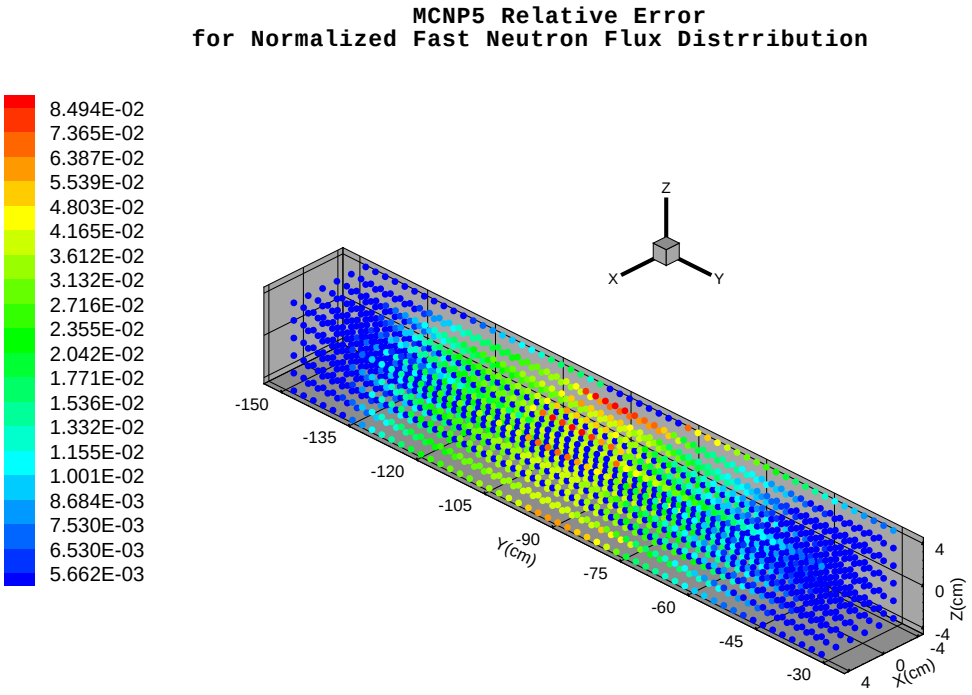

Figure 5-33. 3-D fast neutron flux distribution relative error along the Y-axis(cm) south beam port before collimator region.

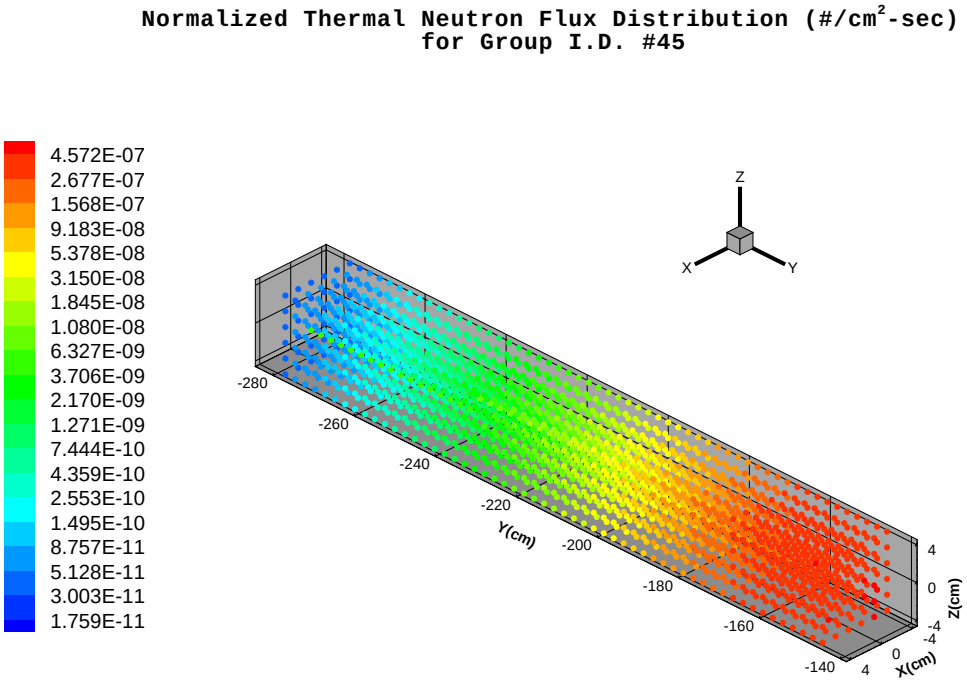

Figure 5-34. 3-D thermal neutron flux distribution along the Y-axis(cm) south beam port collimator region.

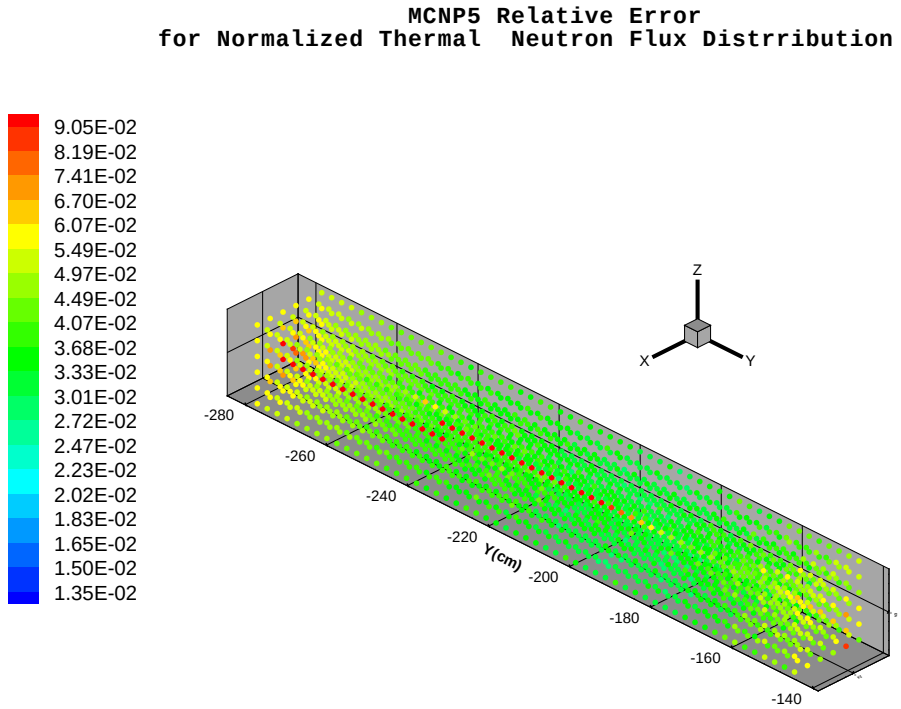

Figure 5-35. 3-D thermal flux distribution relative error along the Y-axis(cm) south beam port collimator region.

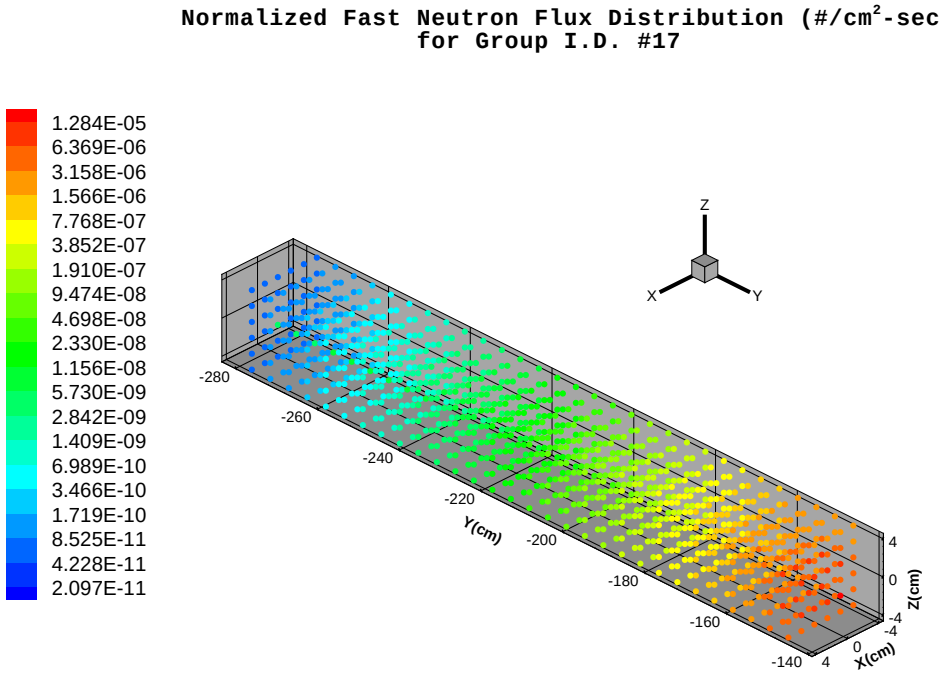

Figure 5-36. 3-D fast neutron flux distribution along the Y-axis(cm) south beam port collimator region.

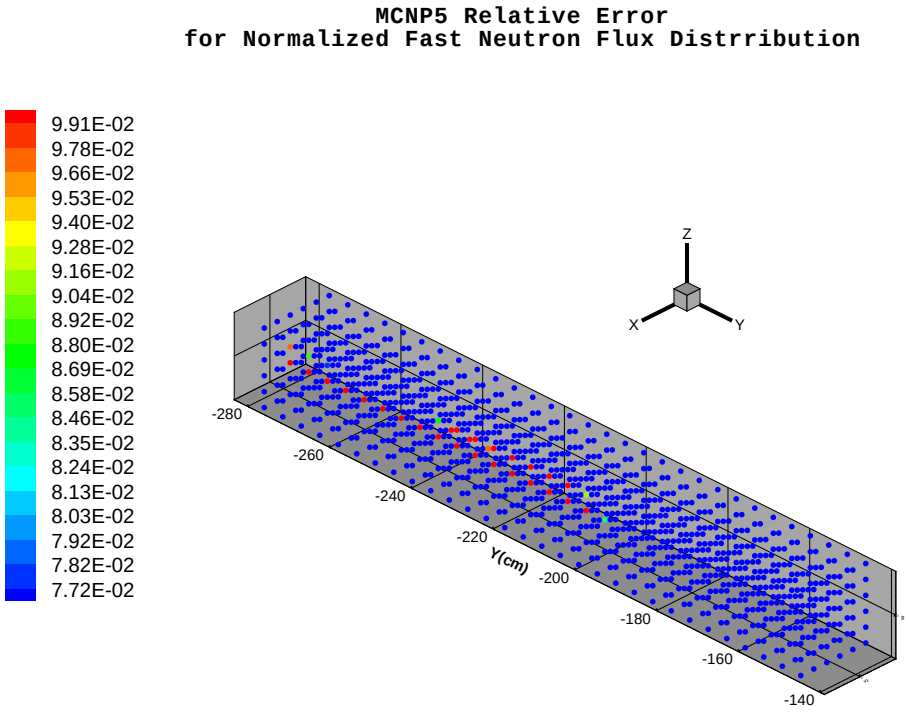

Figure 5-37. 3-D fast flux distribution relative error along the Y-axis(cm) south beam port collimator region.

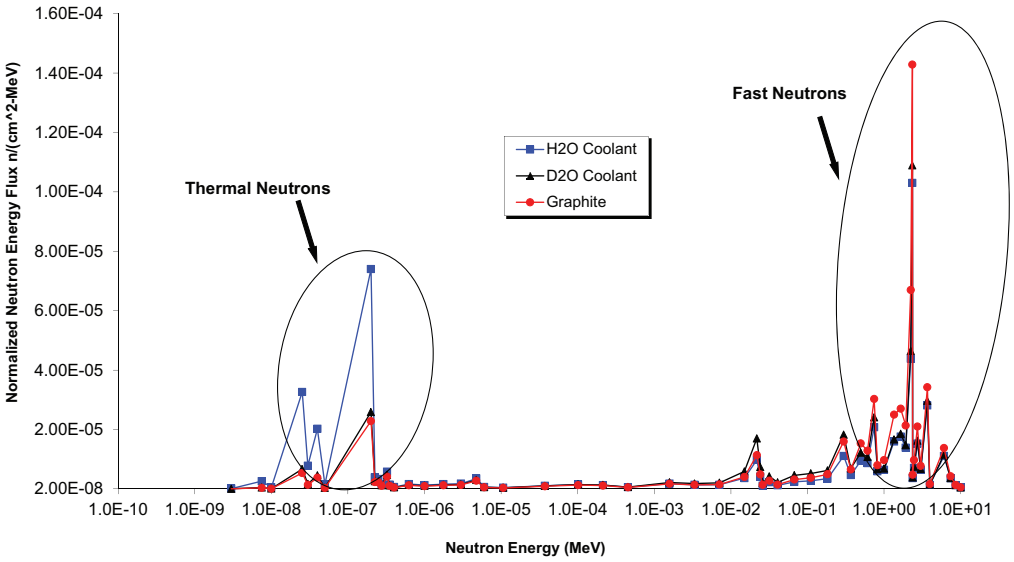

Figure 5-38. Neutron energy flux for different moderators region for 62 energy groups.

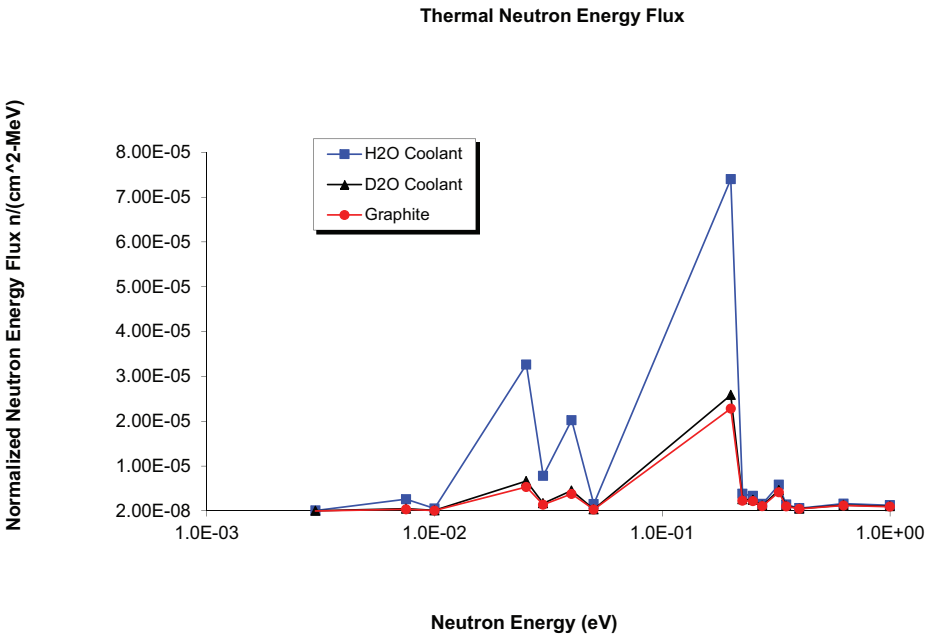

Figure 5-39. Thermal neutron energy flux for three different moderators within 62 energy groups.

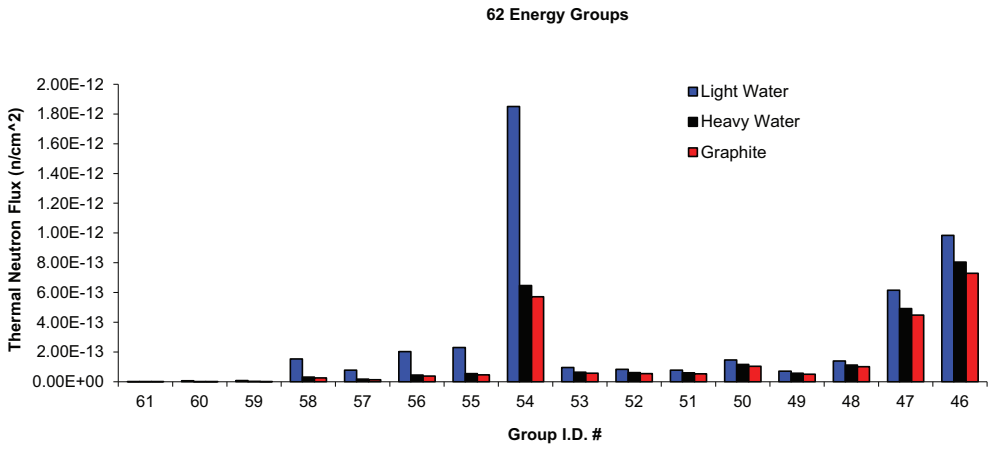

Figure 5-40. Improvement of thermal neutron energy flux for the three different moderators within 62 energy groups.

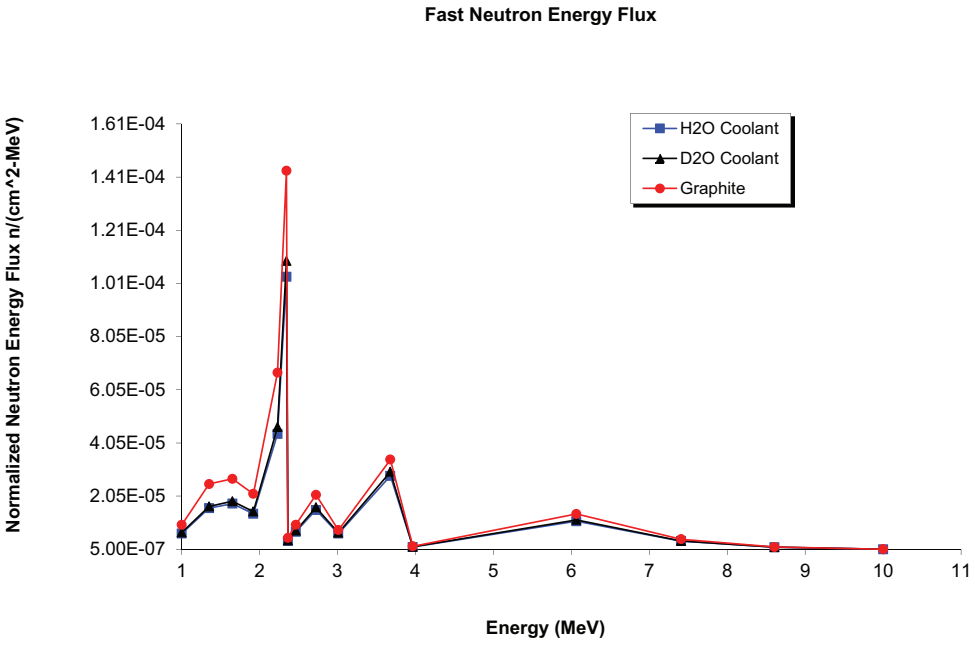

Figure 5-41. Fast neutron energy flux for three different moderators within 62 energy groups.

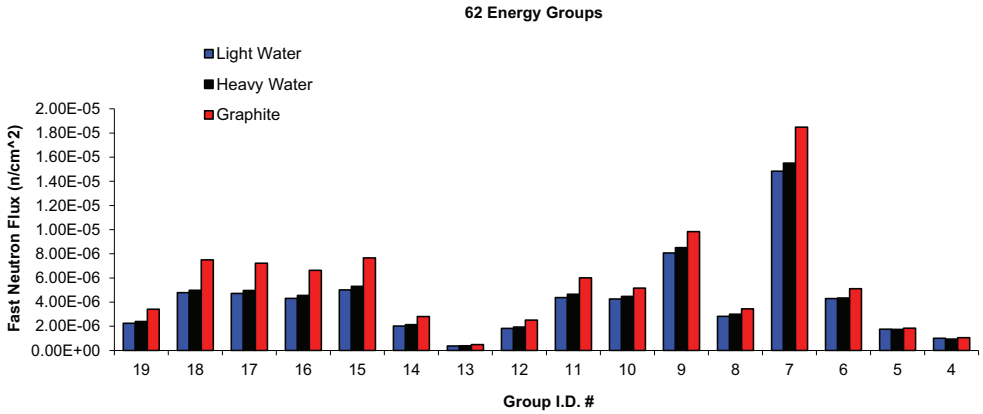

Figure 5-42. Improvement of fast neutron energy flux for the three different moderators within 62 energy groups.

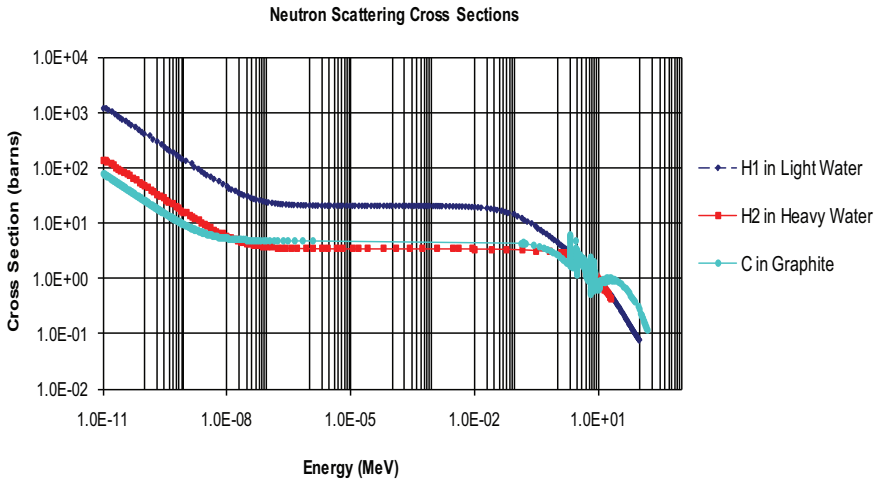

Figure 5-43. Neutron scattering cross sections for hydrogen, deuterium and C in H_2O, D_2O, and Graphite respectively.

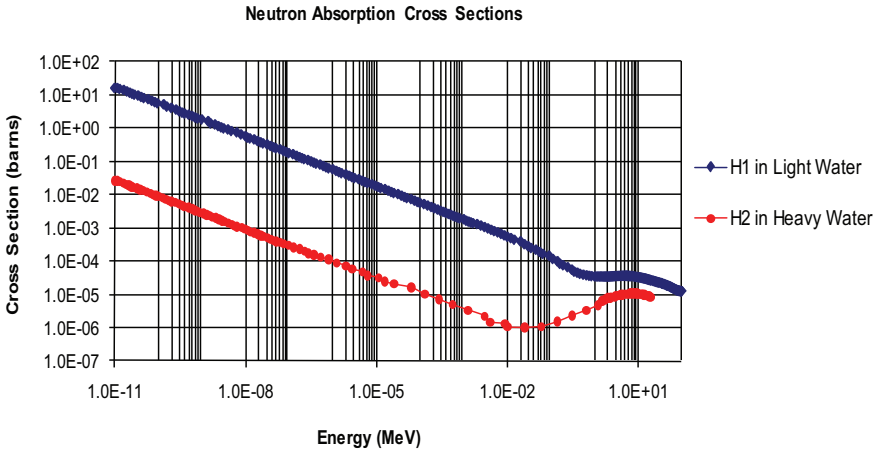

Figure 5-44. Neutron absorption cross sections for hydrogen and deuterium in H_2O and D_2O respectively.

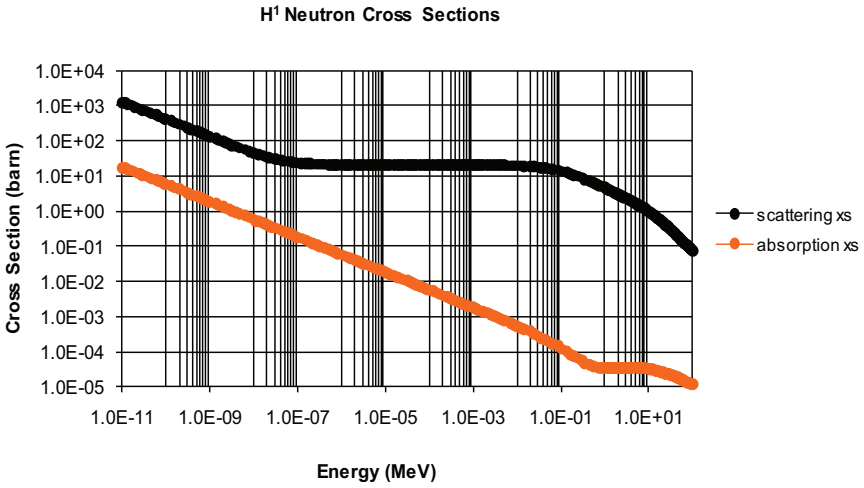

Figure 5-45. Neutron cross sections for hydrogen (H^1)

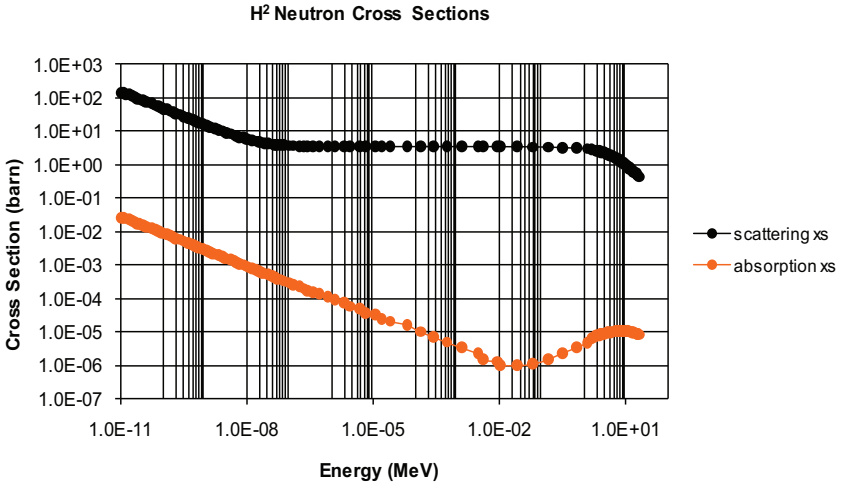

Figure 5-46. Neutron cross sections for deuterium (H^2)

CHAPTER 6
NEUTRON IRRADIATION CHARACTERIZATION OF GOLD FOIL

6.1 Reaction-Rate Equation

Nuclear interactions with high purity activation foils have been one of the most efficient ways of detecting neutrons and measuring the radionuclides produced in the foils from these interactions. Neutron reactions include:

Table 6-1. Absorptive Reactions

Reaction	Name
(n,α)	${}^{1}_{0}\mathrm{n} + {}^{A}_{Z}\mathrm{X} \rightarrow {}^{A-3}_{Z-2}\mathrm{Y} + {}^{4}_{2}\mathrm{He}$
(n,p)	${}^{1}_{0}\mathrm{n} + {}^{A}_{Z}\mathrm{X} \rightarrow {}^{A}_{Z-1}\mathrm{Y} + \mathrm{p}$
(n,fission)	${}^{1}_{0}\mathrm{n} + {}^{A1}_{Z1}\mathrm{X} \rightarrow {}^{A2}_{Z2}\mathrm{X} + {}^{A3}_{Z3}\mathrm{X} + {}^{1}_{0}\mathrm{n}$
(n,2n)	${}^{1}_{0}\mathrm{n} + {}^{A}_{Z}\mathrm{X} \rightarrow {}^{A-1}_{Z}\mathrm{X} + 2{}^{1}_{0}\mathrm{n}$
(n,γ)	${}^{1}_{0}\mathrm{n} + {}^{A}_{Z}\mathrm{X} \rightarrow {}^{A+1}_{Z}\mathrm{X} + \gamma$

Charged particles, ionizing (photons), and fast and thermal neutrons have been used to activate elements. Charged particles have a threshold; photon cross sections are generally smaller than neutron cross sections. Thermal neutrons are generally the most economical choice for activation. In a (n,γ) reaction, the nucleus is left in an excited state. This new, unstable configuration, eventually decays by emission of one or more delayed gammas.

The (n,γ) reaction, also named the radioactive capture reaction, is of particular significance because it spans the complete energy range of neutrons. The other reactions on Table 6-1 are normally threshold reactions and happen just above a definite energy.

This excited nucleus may de-excite by release of a γ and/or β. The three most common types of radioactivity decay are as follow: *photons (γ)*, *heavy charged particles (α)*, and *electrons positrons (β)*.

The (n,-γ) reaction can be defined with the classic Fredholm equation of the first kind [2] :

$$RR_i = N \int_0^\infty \sigma(E)\phi(r, E)\, dE \tag{6–1}$$

where,

RR_i = rate at which reactions are occurring in the sensor foil *i* (reactions/s),

N = number of target atoms in the foil,

σ(E) = energy-dependent microscopic cross-section ,

ϕ(E) = energy-dependent neutron flux in the sample (n/cm^{2}sec).

To solve for neutron flux, the Eqn. 6–1 must be changed into a discrete energy group structure for the flux and cross-section. Define φ as the magnitude of the neutron scalar flux ϕ (in n/cm^{2}sec) and ψ(E) as the neutron energy flux shape (in 1/MeV). Then, Eq. 6–1 can be written as:

$$RR_i = N\varphi \int_0^\infty \sigma(E)\psi(E)\, dE \tag{6–2}$$

where,

$$\int_0^\infty \psi(E)\, dE = 1 \tag{6–3}$$

The integral in Eqn. 6–2 is discretized using a fine mesh multigroup energy bin structure with E_g = 1,2,. . . ,G:

$$RR_i = N\varphi \sum_{g=1}^{G} \int_{E_g}^{E_{g+1}} \sigma(E)\psi(E)\ dE \tag{6–4}$$

For this procedure to be precise, E_{g+1} has to be chosen to be an energy above which the cross-section σ(E) is insignificant. Then, the group shape function is given by:

$$\psi_g = \int_{E_g}^{E_{g+1}} \psi(E)\, dE \tag{6–5}$$

The group cross-section is then defined as:

$$\sigma_g = \frac{\int_{E_g}^{E_{g+1}} \sigma(E)\psi(E)\,dE}{\int_{E_g}^{E_{g+1}} \psi(E)\,dE} \tag{6–6}$$

If we multiply and divide Eqn. 6–4 by the definition of group flux, we obtain:

$$RR_i = N\varphi \sum_{g=1}^{G} \left[\frac{\int_{E_g}^{E_{g+1}} \sigma(E)\psi(E)\,dE}{\int_{E_g}^{E_{g+1}} \psi(E)\,dE}\right] \left[\int_{E_g}^{E_{g+1}} \psi(E)\ dE\right] \tag{6–7}$$

Substitution of Eqn. 6–5 and Eqn. 6–6 into Eqn. 6–7 yields the reaction rate equation:

$$RR_i = N\varphi \sum_{g=1}^{G} \sigma_g \psi_g \tag{6–8}$$

6.2 Activity Equations

Eqn. 6–8, which represents the reaction rate, will be found using the induced activity of the foil irradiated in the neutron environment. After irradiation, the foils are counted on an efficiency-calibrated high purity germanium (HPGe) detector. HPGe spectrometry is used for analyzing environmental samples and determining radioisotope concentrations due to its excellent resolution. This detector has better characteristics such as resolution, absolute efficiency ε(E) and is more sensitive to the detection of impurities. [3, 14] If we ignore the decay of the foil over the time that it is counted, then the counts recorded on the detector over time can be linked to activity as in Eqn. 6–9:

$$A_c = \frac{C}{\varepsilon_d I_\gamma t_c} \tag{6–9}$$

where,

- A_c is the activity at time of counting in dps (desintegration per second)
- C is the total number of counts or the area below the peak got from the γ ray spectrum,
- ε_d is the detector counting efficiency (counts/γ),
- I_γ gamma-ray intensity $\rightarrow$ is the γ-ray yield for the specific γ-ray measured (γ/disintegration) [1, 10]

- t_c counting time (seconds)

6.2.1 Irradiation Activity

While a foil with N number of target nuclides is positioned in a neutron field, it will capture neutrons to create a daughter nuclide N_d.

$$N \xrightarrow{\sigma\phi N} N_d \xrightarrow{\lambda N_d} N_s \tag{6–10}$$

The rate of change with time ($\frac{dN}{dt}$) of the number of the parent nuclide N is:

$$\frac{dN}{dt} = -\sigma\phi N \tag{6–11}$$

then,

$$N(t) = N_0 e^{-\sigma\phi t} \tag{6–12}$$

The rate of change in respect to time ($\frac{dN_d}{dt}$) of the number of the daughter nuclide N_d is a function of the production and loss rates:

$$\frac{dN_d}{dt} = \sigma\phi N - \lambda N_d \tag{6–13}$$

where,

- σ - spectrum averaged cross-section
- ϕ - irradiation neutron flux
- N - number of target nuclides
- N_d - number of daughter nuclides
- λ - decay constant for the daughter nuclide
- $\sigma\phi$N - production rate
- λN_d - loss rate

The decay constant is related to the half-life by following equation:

$$\lambda = \frac{\ln 2}{T_{1/2}} \tag{6–14}$$

If the initial concentration of the daughter nuclide N_d is 0 at t=0, then

$$N(t) = N_0 e^{-\lambda t} \tag{6–15}$$

because there is only loss rate (λN) instead of production rate ($\sigma\phi$N).

Hence, the solution to the equation 6–13 for the number of daughter nuclides present during the irradiation is:

$$N_d(t) = \frac{\sigma\phi N_0}{\lambda}(1 - e^{-\lambda t}) \tag{6–16}$$

The number of disintegrations of a radioactive source in a given time is given by its **activity**. An activity of one becquerel (Bq) means one atom of the source disintegrates per second. One Curie (Ci) is 37 billion Bq.

The activity A of the foil is given by λN. Hence, the activity (A_0) at the end of the irradiation will be:

$$A_0 = \lambda N_d(t_0) \tag{6–17}$$

$$A_0 = \sigma\phi N_0(1 - e^{-\lambda t_0}) \tag{6–18}$$

When the induced activity approaches a horizontal asymptote or saturated activity (A_∞) for an infinitely long irradiation time, the activity will be represented by Eqn. 6–23

If the foil is irradiated for a period of three or four times longer than the value of daughter nuclide's half-life, the number of daughter nuclides has nearly reached a steady-state. The activity at this point is called saturation activity (A_∞). Solving Eqn. 6–13 for steady-state, the following is obtained:

$$0 = \sigma\phi N - \lambda N_d \tag{6–19}$$

Then,

$$A_\infty = \sigma\phi N = \lambda N_d \tag{6–20}$$

where

$$RR = \sigma\phi N \tag{6–21}$$

If the irradiation has proceeded for a time t_0 at which time the foil is removed with an activity A_0:

$$A_0 = A_\infty(1 - e^{-\lambda t_0}) \tag{6–22}$$

where,

$$A_\infty = \frac{A_0}{(1 - e^{-\lambda t_0})} \tag{6–23}$$

6.2.2 Activity After A_0

After exposure to the neutron flux, the foil is transferred to an appropriate radiation counter to measure its activity. Because the activity continuously decays; a careful record must be made of each of the times counted. If the counting is carried out over an interval between t_1 and t_2, the total number of counts C will be:

$$\int_{t_1}^{t_2} A(t)\,dt = \frac{C - B}{\varepsilon_d} \tag{6–24}$$

$$C = \varepsilon_d \int_{t_1}^{t_2} A(t)\,dt + B \tag{6–25}$$

$$C = \varepsilon_d \int_{t_1}^{t_2} A_0 e^{-\lambda(t - t_0)}\,dt + B \tag{6–26}$$

$$C = \varepsilon_d \frac{A_0}{\lambda} e^{\lambda t_0}(e^{-\lambda t_1} - e^{-\lambda t_2}) + B \tag{6–27}$$

where B is the number of background counts expected in t_2 - t_1. After combining Eqs.6–22 and 6–27, we obtain the saturated activity:

$$A_\infty = \frac{\lambda(C_{counts} - B)}{\varepsilon_d e^{\lambda t_0}(1 - e^{-\lambda t_0})(e^{-\lambda t_1} - e^{-\lambda t_2})} \tag{6–28}$$

These equations will be used to determine the activity of the gold foils following irradiation. Eqs. 6–20 and 6–21 show that A_∞ is equivalent to the rate at which the reactions are happening in the sample. Hence, the reaction rate is represented by:

$$RR = \frac{\lambda(C_{counts} - B)}{\varepsilon_d e^{\lambda t_0}(1 - e^{-\lambda t_0})(e^{-\lambda t_1} - e^{-\lambda t_2})} \tag{6–29}$$

If the gamma-ray intensity (I_γ from Table 6-2) is inserted into Eqns. 6–28 and 6–29 the saturated activity and the reaction rate will be:

$$A_\infty = \frac{\lambda(C_{counts} - B)}{\varepsilon_d I_\gamma e^{\lambda t_0}(1 - e^{-\lambda t_0})(e^{-\lambda t_1} - e^{-\lambda t_2})} \tag{6–30}$$

$$RR = \frac{\lambda(C_{counts} - B)}{\varepsilon_d I_\gamma e^{\lambda t_0}(1 - e^{-\lambda t_0})(e^{-\lambda t_1} - e^{-\lambda t_2})} \tag{6–31}$$

Activation foils are thus widely used for mapping the spatial variation of steady-state neutron fluxes in reactor cores, where the extreme temperature, pressure, and limited space severely constrain the types of conventional detectors that may be used.[8]

6.3 Reaction Rate Calculation using MCNP5

The reaction rates and the corresponding saturation activity were calculated for the gold foil at different locations along the beam port. This was accomplished using the FM tally from MCNP5. The reaction number used for FM tally was 102, which corresponds to the reaction cross-section (n,γ). The results acquired will be used to design the foil irradiation experiment in the UFTR reactor.

It is clear that the gold foil target in the beam port should be located close to the moderator region due to the high intensity of flux in this area. However, the gold foils

can be relocated as desired. It is observed when gold foil is put far from the moderator region, reaction rate statistics from MCNP5 code become very poor; yet, with the application of variance reduction called DXTRAN great results can be achieved.

DXTRAN is a variance reduction technique which is considered partially deterministic. DXTRAN usually should not be in problems which have reflecting surfaces or white boundaries. This type of variance reduction has great usability in regions where neutrons are highly absorbed such as a small gap in a concrete collimator. DXTRAN is a vary useful type of variance reduction used to obtain particles in a very small region by increasing in a desired tally. The DXTRAN sphere follow the principle that it must fully encircle the area of to obtain as much as possible collided particles in a cell. The failure of having the proper sphere radius would give a poor statistics output. Upon sampling a collision or source emission probability, DXTRAN estimates the correct weight fraction that should scatter or be emitted toward the sphere and arrive without collision. Therefore, the DXTRAN method puts this correct weight on the sphere.

Gold Foil Material Properties:

- Foil Reaction: ^{197}Au (n,γ) ^{198}Au
- Mass(g/mole): 196.967
- Density: 19.3g/cm^3
- Thermal Microscopic Cross Section: 8.80×10^{-23}cm^2
- Fast Microscopic Cross Section: 9.50×10^{-23}cm^2
- E_γ: 411.8 KeV
- 411.8keV photons per decay (I_γ): 95.54%
- Isotope Half-Life ($T_{1/2}$): 2.695 days
- Number Density: $5.910*10^{22}$ nuclei/cm^3

Table 6-2. Recommended γ-ray calibration energies and intensities

Parent	E_γ(KeV)	I_γ(%)
^{198}Au	411.80205	95.54
	675.8836	0.806
	1087.6842	0.159

Table 6-3. ^{197}Au gold foil reaction rate

Reaction Rate	Position (cm)	nps	16 CPU - Total Comp. Time (min)
14.3680E-08	-149	4 million	3,304.36
8.88150E-09	-164	5 million	3,493.22
4.87450E-09	-189	5 million	1,925.04

Gold-198 ($^{198}_{79}$Au)

$^{198}_{79}$Au is produced by the neutron activation of the stable $^{197}_{79}$Au (Gold-197). The $^{198}_{79}$Au decays by the beta emission (β) with half-life of 2.7 days to an isotope of mercury:

$$^{198}_{79}Au \rightarrow ^{198}_{80} Hg + \gamma + ^{0}_{-1} e \tag{6–32}$$

It emits a 412 KeV gamma (plus insignificant amounts of other energies). For many years Gold-198 grains, consisting of Gold-198 encapsulated in platinum, were used for permanent implant, especially for the head and neck region. However the method has largely fallen into disuse and Gold-198 grains no longer feature in UK suppliers catalogue.

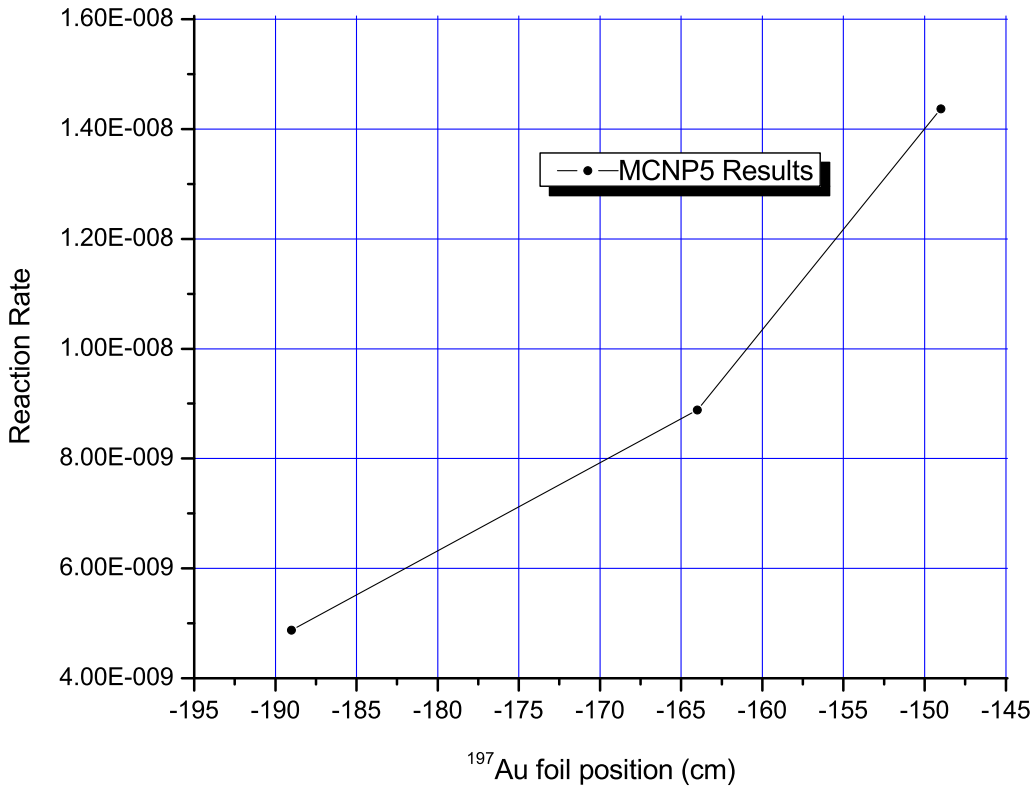

Figure 6-1. MCNP5 calculations for ^{197}Au foils at 3 different locations.

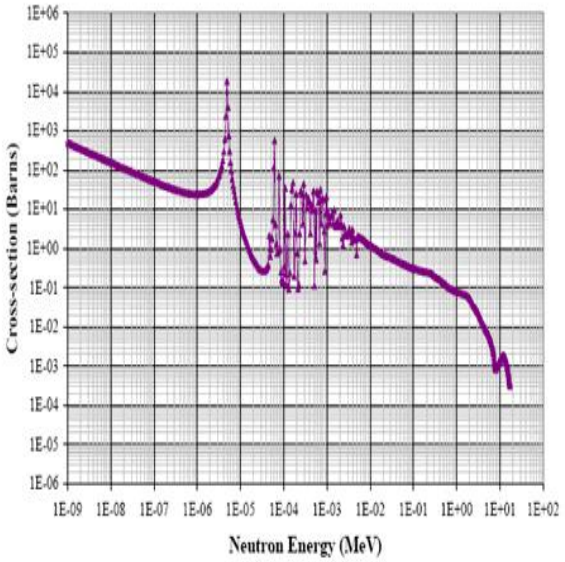

Figure 6-2. ^{197}Au (n,γ) ^{198}Au cross-section as a function of neutron energy

CHAPTER 7
CONCLUSION

The key objective of this research was to acquire the 2-D and 3-D normalized multi-group neutron flux distribution through out the University of Florida Training Reactor (UFTR) radiation beam port. In addition to that, develop an efficient model providing the multi-group neutron flux distribution in a reasonable total computation time by using variance reduction a Monte Carlo Technique.

This research created a benchmark Monte Carlo Neutral Particle version 5 (MCNP5) models of the UFTR radiation beam ports that can now be used for future simulation of the multi-group neutron flux distribution and neutron flux intensity at the different locations of the radiation beam ports. The MCNP5 model can also be used to benchmark the MCNP5 neutron reaction rate with experimental values from the reactor.

Criticality analysis of the UFTR core model using MCNP5 was performed to obtain 3-D neutron fission density distribution in the reactor core by using fixed source method a three point source.

Once neutron fission density distribution was calculated the multi-group neutron flux distribution, neutron energy flux, and neutron reaction rate were computed using a monodirectional source definition to save computational time. Three different types of variance reduction were applied to the work to obtain desired output: Geometry Splitting, Russian Roulette, and Survival Bias. Where, the PHYS and IMP commands were used.

Multi-group neutron flux distribution comparison with and without collimator was made in the radiation beam port to observe the absorption and reflection of neutrons due to the collimator.

Additional study was made in the neutron spectra to see the impact of different moderators surrounding the reactor core.

APPENDIX A
URANIUM SILICIDE

(0.1eV<E<1eV)

Table A-1. Uranium Silicide - (U_3Si_2)

Material	Symbol	Weight fraction	σ_f(barn)
Uranium 234	U-234	1.02×10^{-3}	0.074313
Uranium 235	U-235	1.24×10^{-1}	92.4428
Uranium 236	U-236	6.52×10^{-4}	0.0126479
Uranium 238	U-238	5.04×10^{-1}	2.83519×10^{-6}
Silicon	Si	4.97×10^{-2}	-

Table A-2. Uranium Silicide Impurities

Material	Symbol	Weight fraction	σ_a(barn)
Barium	Ba	1.36×10^{-6}	x
Berilum	Be	3.40×10^{-7}	2.029×10^{-3}
Boron 10	*B-10*	1.81×10^{-7}	9.094×10^{2}
Cadmium	*Cd*	3.40×10^{-7}	2.019×10^{2}
Calcium	Ca	1.36×10^{-5}	1.006×10^{-1}
Carbon	C	1.66×10^{-4}	7.794×10^{-4}
Chromium	Cr	1.25×10^{-5}	1.827×10^{-1}
Cobalt	Co	3.40×10^{-6}	8.710×10^{0}
Copper	Cu	6.85×10^{-5}	1.056×10^{0}
Europium	Eu	1.36×10^{-7}	1.303×10^{4}
Gadolinium	Gd	1.36×10^{-7}	x
Iron	Fe	4.13×10^{-4}	6.171×10^{-1}
Lead	Pb	3.40×10^{-7}	1.480×10^{-1}
Lithium	*Li*	6.79×10^{-8}	1.029×10^{-2}
Magnesium	Mg	6.79×10^{-6}	1.502×10^{-2}
Manganese	Mn	5.89×10^{-6}	3.317×10^{0}
Molybdenum	Mo	2.04×10^{-6}	6.221×10^{-1}
Nickel	Ni	2.94×10^{-5}	1.101
Nitrogen	N	3.74×10^{-5}	4.399×10^{-1}
Phosphorus	P	1.36×10^{-5}	4.493×10^{-2}
Samarium	Sm	1.36×10^{-7}	2.353×10^{1}
Silver	Ag	6.79×10^{-7}	8.166
Sodium	Na	6.79×10^{-6}	1.291×10^{-1}
Tin	Sn	6.79×10^{-7}	x
Tungsten	W	1.47×10^{-5}	4.502×10^{0}
Vanadium	V	3.06×10^{-6}	1.126
Zinc	Zn	2.60×10^{-6}	x
Zirconium	Zr	6.79×10^{-7}	2.691×10^{-1}

APPENDIX B
ALUMINUM

(0.1eV<E<1eV)

Table B-1. Aluminum - (Al)

Material	Symbol	Weight fraction
Aluminum	Al	3.21×10^{-1}

Table B-2. Aluminum Impurities

Material	Symbol	Weight fraction	σ_a(barn)
Zinc	Zn	6.41×10^{-5}	
Copper	Cu	3.21×10^{-6}	
Boron 10	B10	6.41×10^{-7}	
Cadmium	Cd	3.21×10^{-6}	
Lithium	Li	3.21×10^{-6}	
Silicon + Iron	Si + Fe	5.35×10^{-4}	
Oxygen	O	3.11×10^{-4}	

APPENDIX C
THE EFFECT OF THE IMPURITY IN THE FUEL ON THE UFTR K_{EFF}.

(Keff)

Table C-1. $\sim$ no ^{10}B in the Aluminum Cladding

Cases	^{10}B	Cd	Li	K_{eff}
Reference Case	2ppm	1ppm	0.1ppm	0.99958
Case 4	0.1ppm	1ppm	0.1ppm	1.00114
Case 5	0.1ppm	1ppm	0.4ppm (4x)	1.00102
Case 6	0.1ppm	1ppm	2ppm (20x)	1.00098

Table C-2. K_{eff} and Standard Deviation

Cases	K_{eff}	Standard Deviation
Reference Case	0.99958	0.00012
Case 4	1.00114	0.00015
Case 5	1.00102	0.00016
Case 6	1.00098	0.00015

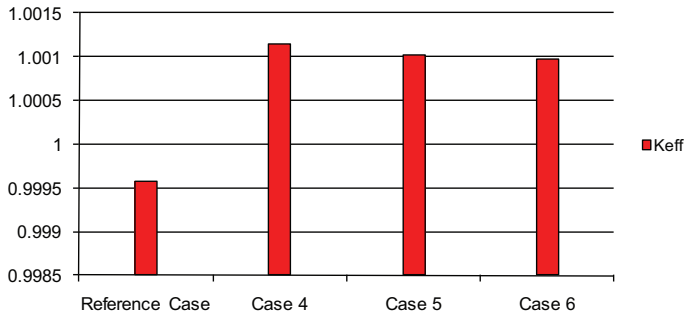

Figure C-1. Keff1.

Table C-3. ^{10}B in the Aluminum Cladding/ Variation of Cd concentration while Li is constant

Cases	^{10}B	Cd	Li
Reference Case	2ppm	1ppm	0.1ppm
Case 1	2ppm	2ppm (2x)	0.1ppm
Case 8	2ppm	4ppm (4x)	0.1ppm

Table C-4. K_{eff} and Standard Deviation

Cases	K_{eff}	Standard Deviation
Reference Case	0.99958	0.00012
Case 1	0.99916	0.00016
Case 8	0.99887	0.00016

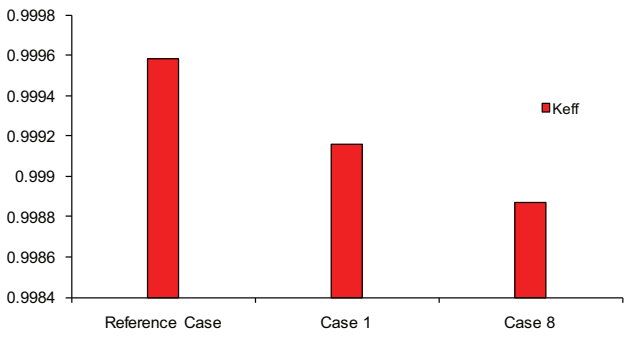

Figure C-2. Keff2.

Table C-5. ^{10}B in the Aluminum Cladding/ Variation of Li concentration while Cd is constant

Cases	^{10}B	Cd	Li
Reference Case	2ppm	1ppm	0.1ppm
Case 2	2ppm	1ppm	0.4ppm (4x)
Case 7	2ppm	1ppm	2ppm (20x)

Table C-6. K_{eff} and Standard Deviation

Cases	K_{eff}	Standard Deviation
Reference Case	0.99958	0.00012
Case 2	0.99939	0.00016
Case 7	0.99927	0.00012

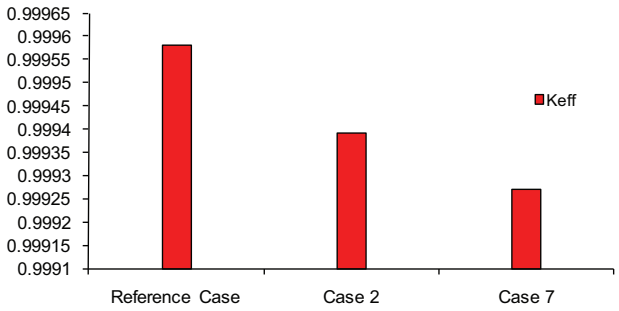

Figure C-3. Keff3.

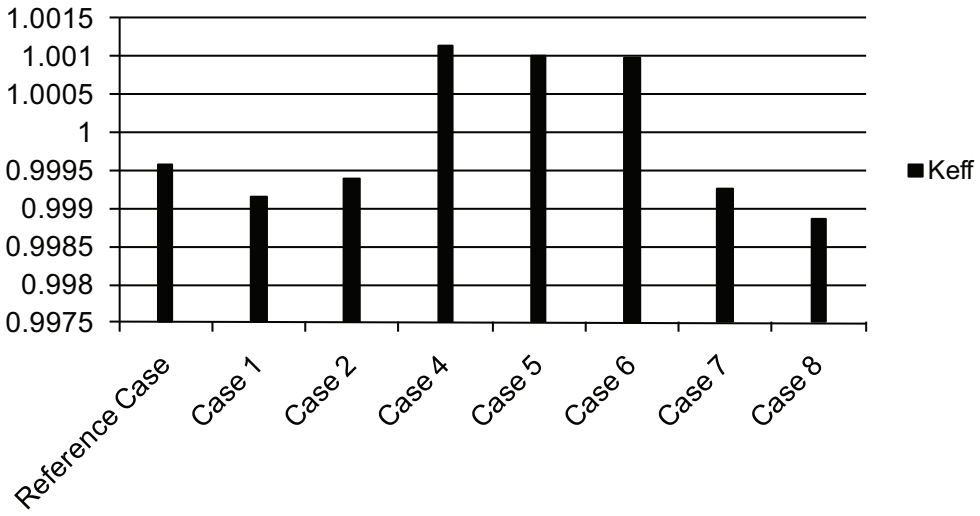

Figure C-4. $Keff_{final}$.

APPENDIX D
FISSION CROSS-SECTIONS

(ENDF/B-VII Fissionable Nuclides Cross-Section Plot in Log_{10} Scale at 300°K(26.85°C))

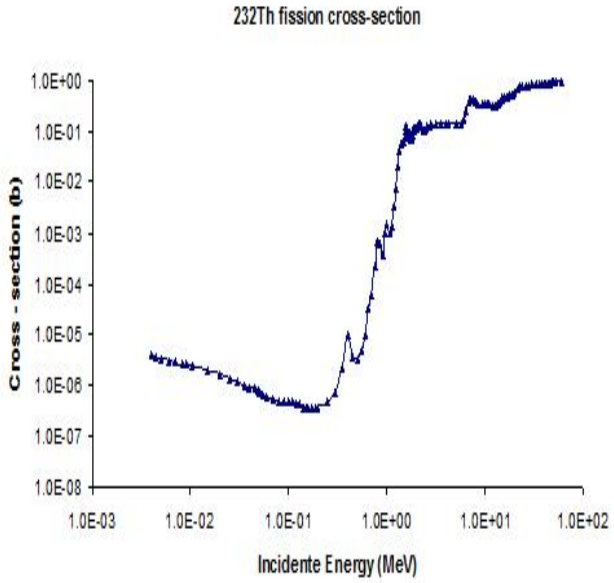

Figure D-1. ^{232}Th fission cross-section versus neutron energy (MeV).

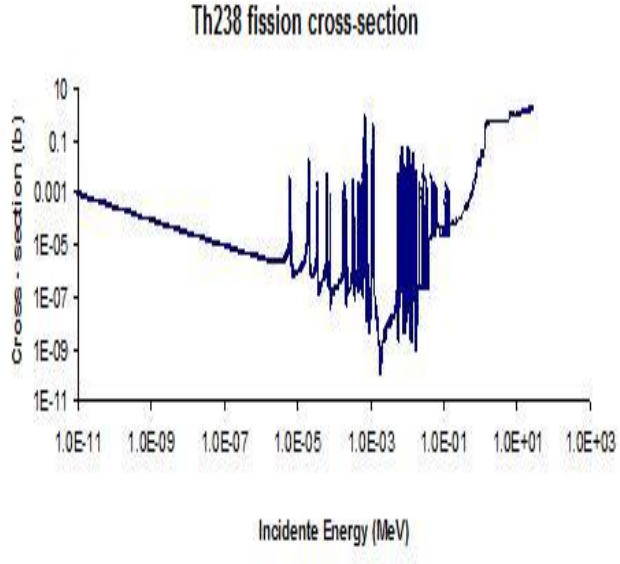

Figure D-2. ^{238}U fission cross-section versus neutron energy (MeV).

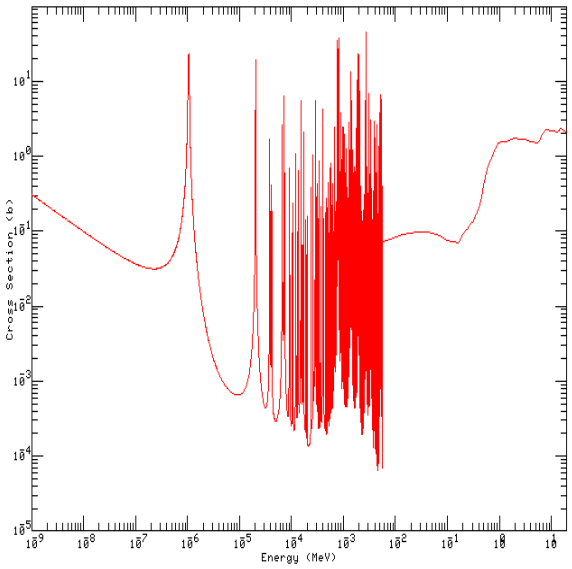

Figure D-3. ^{240}Pu fission cross-section versus neutron energy (MeV).

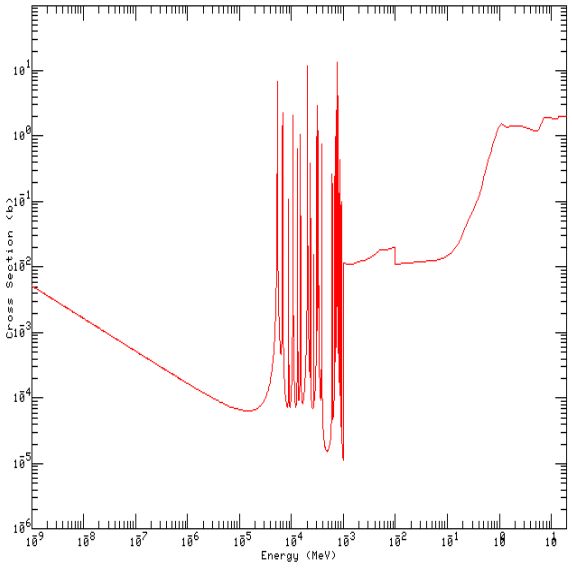

Figure D-4. ^{242}Pu fission cross-section versus neutron energy (MeV).

APPENDIX E
47 ENERGY GROUPS

(Average ♯ of Fission Neutrons χ(E)d(E))

Table E-1. 47 Energy Groups

$E_{highest}$ (MeV)	E_{lowest} (MeV)	Energy Group I.D.♯	Average ♯ of Fission Neutrons
17.33	14.19	1	3.0873e-05
14.19	12.21	2	1.4040e-04
12.21	10	3	8.8800e-04
10	8.607	4	2.1814e-03
8.607	7.408	5	5.0761e-03
7.408	6.065	6	1.4962e-02
6.065	4.966	7	2.9375e-02
4.966	3.679	8	7.8966e-02
3.679	3.012	9	7.5313e-02
3.012	2.725	10	4.2975e-02
2.725	2.466	11	4.5322e-02
2.466	2.365	12	1.9502e-02
2.365	2.346	13	3.7886e-03
2.346	2.231	14	2.3761e-02
2.231	1.92	15	7.1682e-02
1.92	1.653	16	7.0559e-02
1.653	1.353	17	8.9275e-02
1.353	1.003	18	1.1618e-01
1.003	8.208e-1	19	6.4226e-02
8.208e-1	7.427e-1	20	2.7925e-02
7.427e-1	6.081e-1	21	4.8114e-02
6.081e-1	4.979e-1	22	3.8767e-02
4.979e-1	3.688e-1	23	4.3574e-02

Table E-2. 47 Energy Groups cont.

$E_{highest}$ (MeV)	E_{lowest} (MeV)	Energy Group I.D.♯	Average ♯ of Fission Neutrons
3.688e-1	2.972e-1	24	2.2689e-02
2.972e-1	1.832e-1	25	3.2557e-02
1.832e-1	1.111e-1	26	1.7150e-02
1.111e-1	6.738e-2	27	8.4173e-03
6.738e-2	4.087e-2	28	4.0687e-03
4.087e-2	3.183e-2	29	1.1529e-03
3.183e-2	2.606e-2	30	6.6001e-04
2.606e-2	2.418e-2	31	2.0091e-04
2.418e-2	2.188e-2	32	2.3566e-04
2.188e-2	1.503e-2	33	6.2930e-04
1.503e-2	7.102e-3	34	5.6438e-04
7.102e-3	3.355e-3	35	1.8407e-04
3.355e-3	1.585e-3	36	5.9873e-05
1.585e-3	4.540e-4	37	2.4400e-05
4.540e-4	2.144e-4	38	2.9855e-06
2.144e-4	1.013e-4	39	9.6865e-07
1.013e-4	3.727e-4	40	3.6195e-07
3.727e-5	1.068e-5	41	8.8031e-08
1.068e-5	5.040e-6	42	1.0780e-08
5.040e-6	1.860e-6	43	4.0116e-09
1.860e-6	8.760e-7	44	7.8460e-10
8.760e-7	4.140e-7	45	2.5296e-10
4.140e-7	1.000e-7	46	1.0729e-10

APPENDIX F
BARYTES (BARITE) CONCRETE

(Barytes concrete shielding)

Table F-1. Elemental composition of barytes concretes in grams of element per cm^3 of concrete

Element		BA-a	BA-b	BA-H	BAHA	BAHA-d	BA-OR
ρ (g/cm^3)		3.50	3.39	2.57	2.35	2.28	3.30
H	in water	0.0243	0.0122	0.007	0.026	0.0298	0.036
	in ore	-	-	-	0.0045	-	-
O	in water	0.195	0.0975	0.710	0.0209	1.084	0.291
	in ore	0.872	0.872	0.710	0.494	1.084	0.971
	in cement	0.118	0.118	0.710	0.138	1.084	0.971
C		-	-	0.0233	-	-	-
Mg	in ore	-	-	-	-	0.0441	0.0099
	in cement	0.0038	0.0038	-	0.0046	0.0441	0.0099
Al	in ore	-	-	0.0123	0.0546	0.0565	0.0066
	in cement	0.0137	0.0137	0.0123	0.0161	0.0565	0.0066
Si	in ore	-	-	0.180	0.308	0.232	0.139
	in cement	0.0362	0.0352	0.180	0.0414	0.232	0.139
S		0.364	0.364	0.180	0.144	0.0094	0.287
Ca	in ore	0.0203	0.0203	0.148	0.109	0.209	0.135
	in cement	0.147	0.147	0.148	0.172	0.209	0.135
Fe	in ore	0.151	0.151	0.595	-	0.0338	0.277
	in cement	0.0091	0.0091	0.595	0.0107	0.0338	0.277
Ba		1.551	1.551	0.718	0.618	0.577	1.20

Table F-2. Constants for thermal neutrons for barytes concretes

Concrete Mix no.	Density ρ (g/cm^3)	Σ_a	D	L	K
BA-a	3.5	0.0197	0.440	4.72	0.212
BA-b	3.39	0.0176	0.667	6.17	0.162
BA-H	2.57	0.0220	0.912	6.45	0.155
BAHA	2.35	0.0128	0.421	5.75	0.174
BAHA-d	2.28	0.0111	0.412	6.10	0.164
BA-OR	3.30	0.0224	0.334	3.86	0.259

REFERENCES

[1] *Standard Test Methods for Detector Calibration and Analysis of Radionuclides.*, 1998.

[2] Aghara, S. and Charlton, W. "Characterization and quantification of an in-core neutron irradiation facility at a TRIGA II research reactor." *Nuclear Instruments and Methods in Physics Research B* 248 (2006): 181–190.

[3] Attix, F. H. *Introduction to Radiological Physics and Radiation Dosimetry.* New York: John Wiley Sons, 1986.

[4] Duderstadt, J. J. and Hamilton, L. J. *Nuclear Reactor Analysis.* New York: John Wiley Sons, 1976.

[5] Ghassoun, J. and Jehouani, A. "Russian roulette efficiency in Monte Carlo ressonant absorption calculations." *Applied Radiation and Isotopes* 53 (2000).4-5: 881–885.

[6] Grunauer, F. *Entwicklung eines Neutronen-Kollimators f urein medizinischbiologisches Bestrahlungssystem.* Ph.D. thesis, 1975.

[7] Howerton, R. J. *The LLL Evaluated Nuclear Data Library (ENDL): Evaluation Techniques, Reaction Index, and Description of Individual Evaluations.*, 1975.

[8] Knoll, G. F. *Radiation detection and measurement.* New Jersey: John Wiley Sons,Inc., 2000.

[9] Lamarsh, J. R. *Introduction to Nuclear Engineering.* MA: Addison-Wesley Publishing Company, 1983, 2nd ed.

[10] Lemmel, H. D. *X-ray and Gamma-ray Standards for Detector Calibration.*, 1991.

[11] Shultis, J. K. and Faw, R. E. *A MCNP Primer.*, 2004.

[12] Verbeke, J. M., Hagmann, C., and Wright, D. *Simulation of Neutron and Gamma Ray Emission from Fission and Photofission.*, 2009.

[13] Vernetson, W. G. *UFTR Design and Operation Characteristics.*, 2004.

[14] Vichaidid, T., Soodprasert, T., and Verapaspong, T. "Calibration of HPGe Gamma-Ray Planar Detector System for Radioactivity Standards." *Natural Science* 41 (2007): 198–202.

[15] White, J. E., Ingersoll, D. T., Slater, C. O., and Roussin, R. W. *BUGLE-96: A revised multigroup cross section library for LWR applications based on ENDF/B-VI release 3.*, 1996.

[16] Wolber, G., Hoever, K., Krauss, O., and Maier, W. "A new fast-neutron source for radiobiological research." *Physics in Medicine and Biology* 42 (1997): 725–733.

BIOGRAPHICAL SKETCH

Romel Franca born in Rio de Janeiro and lives in Florida. He was in the Naval Academy for few years to become a navy officer.

He had the opportunity to be twice Mathematical Olympic Champion in the state of Florida and be accepted to the Cornel University in New York - Ithaca to work in the research area of mathematical modeling of diseases in the Mathematical and Theoretical Biology Institute (MTBI).

Then pursing a degree in electrical engineering at University of Florida did work at Computational Neurological Electrical Engineering Lab (CNEL) building electronics circuits, and working with MATLAB simulations for the dynamical analysis of the olfactory brain. A mathematical model created at Berkeley University.

Once finished the electrical engineering degree, he joined the Nuclear Engineering Department to become a nuclear engineer in the area of Reactor Physics, and at the same time working with search engine optimization (SEO).